Project - MyWave

Report on wave physics development

Reference: MyWave-D1.3

Project N°: FP7-SPACE-2011-284455	**Work programme topic:** SPA.2011.1.5.03 – R&D to enhance future GMES applications in the Marine and Atmosphere areas
Start Date of project : 01.01-2012	**Duration**: 36 Months

WP leader: Luigi Cavalieri	**Issue:** 1.0
Contributors : Peter Janssen and Øyvind Breivik	
MyWave version scope: All	
Approval Date : 17 Nov. 2014	**Approver:** Øyvind Saetra
Dissemination level: PU	

Surface Wave Effects in the NEMO Ocean Model: Forced and Coupled Experiments

Øyvind Breivik[12], Kristian Mogensen[1], Jean-Raymond Bidlot[1], Magdalena Alonso Balmaseda[1], and Peter A.E.M. Janssen[1]

Abstract. The NEMO general circulation ocean model is extended to incorporate three physical processes related to ocean surface waves, namely the turbulent kinetic energy flux from breaking waves, the water-side stress (modified by growth and dissipation of the oceanic wave field), and the Stokes-Coriolis force. Experiments are run with NEMO in forced (ocean-only) and coupled mode. Ocean-only integrations are forced with fields from the ERA-Interim analysis. All three effects are noticeable in the extra-tropics, but the sea-state dependent energy flux yields by far the largest difference compared with a control run due to its influence on the uppper ocean mixing. The biases in sea surface temperature as well as subsurface temperature are reduced, and the total ocean heat content exhibits a trend closer to that observed in a recent ocean reanalysis (ORAS4) when wave effects are included. Seasonal integrations of the coupled atmosphere-wave-ocean model consisting of NEMO, the wave model ECWAM and the atmospheric model of ECMWF similarly show that the sea surface temperature biases are greatly reduced when the mixing is controlled by the sea state and properly weighted by the thickness of the uppermost level of the ocean model.

1. Introduction

Surface waves affect the ocean surface boundary layer (OSBL) through a number of processes, but perhaps most visibly through breaking waves which appear as whitecaps on the ocean surface [*Monahan*, 1971; *Wu*, 1979]. These breaking waves enhance the turbulence in the upper part of the ocean significantly [*Craig and Banner*, 1994; *Craig*, 1996]. Waves absorb kinetic energy and momentum from the wind field when they grow and in turn release it when they break [*Janssen et al.*, 2004; *Rascle et al.*, 2006; *Ardhuin and Jenkins*, 2006; *Janssen*, 2012]. This lowers or raises the stress on the water side [*Janssen et al.*, 2004; *Janssen*, 2012] compared to the air-side stress depending on whether the sea state is growing or decaying. Only when the wave field is in equilibrium with the energy injected by the wind will the stress on the two sides of the surface be equal.

Through the interaction with the Coriolis effect, the Stokes drift velocity associated with the wave field adds an additional term to the momentum equation. The effect was first discussed by *Hasselmann* [1970] and has since been investigated for idealized cases by *Weber* [1983], *Jenkins* [1987], *McWilliams and Restrepo* [1999] and *McWilliams and Sullivan* [2000] among others. The force is variously known as the Stokes-Coriolis force or the Hasselmann force depending on whether it is considered to be purely an effect of the average Coriolis force acting on a particle with a Lagrangian velocity as given by the mean currents and the waves or as a tilting of the planetary vorticity [*Polton et al.*, 2005; *Broström et al.*, 2014]. The force does not modify the total mass transport but it will alter the distribution of momentum over the depth of the Ekman layer [*McWilliams and Restrepo*, 1999; *Polton*, 2009].

The impact of the oceanic wave field on upper-ocean mixing and mean properties has been studied in a number of single-column mixed-layer model experiments [*Craig and Banner*, 1994; *McWilliams and Restrepo*, 1999; *McWilliams and Sullivan*, 2000; *Burchard*, 2001; *Kantha and Clayson*, 2004; *Mellor and Blumberg*, 2004; *Rascle et al.*, 2006; *Ardhuin and Jenkins*, 2006; *Janssen*, 2012]. Several studies employed large eddy simulations (LES) to investigate the impact of an idealized wave field on Langmuir turbulence in the upper ocean [*Skyllingstad and Denbo*, 1995; *McWilliams et al.*, 1997; *Teixeira and Belcher*, 2002; *Polton and Belcher*, 2007; *Grant and Belcher*, 2009]. But so far the impact of wave processes on fully coupled models of the ocean, the atmosphere and the oceanic wave field remains relatively unexplored, although it has been recognized that wave effects play a potentially important role in the climate system [*Babanin et al.*, 2009; *Cavaleri et al.*, 2012; *Fan and Griffies*, 2014]. *Fan et al.* [2009] demonstrated the importance of correctly modelling momentum and energy fluxes from the wave field to the ocean under hurricane conditions. *Fan and Griffies* [2014] found that the introduction of Langmuir turbulence following the parameterizations by *McWilliams and Sullivan* [2000] and *Smyth et al.* [2002] as well as the parameterization of mixing by non-breaking waves suggested by [*Qiao et al.*, 2004] significantly changed the upper-ocean temperature in long-term coupled climate integrations. The latter proposed mixing process appears similar to the mixing due to the high Reynolds numbers of the orbital motion of non-breaking waves explored by *Babanin* [2006] and *Babanin and Haus* [2009]. Using a climate model of intermediate complexity, *Babanin et al.* [2009] explored three wave-related mixing processes, namely injection of turbulent kinetic energy from breaking waves, Langmuir circulation and the aforementioned mixing by non-breaking waves. Like *Fan and Griffies* [2014] they found that all three processes contributed to the mixed layer depth and the temperature of the mixed layer. Similarly, *Huang et al.* [2011] coupled WAVEWATCH III [*Tolman et al.*, 2002] to a version of the Princeton Ocean Model [*Blumberg and Mellor*, 1987] and demonstrated an improved summertime thermal profile using the non-breaking parameterization of *Qiao et al.* [2004].

These wave-driven processes influence the vertical structure of the temperature and current fields in the mixed layer in general, and in the upper few meters in particular. This

---

[1]European Centre for Medium-Range Weather Forecasts
[2]On leave from the Norwegian Meteorological Institute

has practical implications for coupled models as these processes will affect the behavior of coupled atmosphere-ocean simulations [*Janssen et al.*, 2013]. However, on shorter time scales and at higher spatial resolution it is also clear that these processes will influence the drift of objects and pollutants on the sea surface or partially or wholly submerged. This has practical importance for oil spill modelling [*Hackett et al.*, 2006], search and rescue [*Breivik and Allen*, 2008; *Davidson et al.*, 2009; *Breivik et al.*, 2013a] or dispersion of biological material (see e.g. *Röhrs et al.* [2014]).

The NEMO ocean model [*Madec and the NEMO team*, 2012] has been coupled to the atmospheric model with wave forcing from the wave model as part of the ensemble suite of the Integrated Forecast System (IFS) of the European Centre for Medium-Range Weather Forecasts (ECMWF) since November 2013 (IFS Cycle 40R1). Here we describe the implementation of the three wave effects mentioned above in forced (ocean-only) integrations of NEMO using forcing from the ERA-Interim reanalysis [*Dee et al.*, 2011] as well as their implementation in a fully coupled atmosphere-wave-ocean seasonal forecast system.

The paper is organized as follows. Sec 2 describes the processes that have been implemented and lays out their actual implementation in NEMO. Sec 3 describes the results of long ocean-only integrations and compares with control runs, observations and the ORAS4 ocean reanalysis [*Balmaseda et al.*, 2013]. Sec 4 describes the coupled atmosphere-wave-ocean coupling used for seasonal integrations and compares the results of a control run where no direct coupling exists between the wave model and the ocean model to a run where NEMO is forced with stresses, turbulent fluxes and Stokes drift from the wave model ECWAM [*ECMWF*, 2013]. Finally, in Sec 5 we discuss the results and make suggestions for further work.

2. Wave effects in the Ocean Surface Boundary Layer

Introducing wave forcing in an Eulerian ocean model entails communicating the relevant forcing fields from a wave model. We start with a brief presentation of spectral wave models and how the two-dimensional wave spectrum relates to the fluxes and fields that have a bearing on the ocean surface boundary layer.

2.1. Fluxes and fields estimated from a spectral wave model

Third generation spectral wave models [*Hasselmann et al.*, 1988; *Tolman*, 1991; *Komen et al.*, 1994; *Ris et al.*, 1999; *Janssen*, 2004; *Tolman et al.*, 2002; *Holthuijsen*, 2007; *Cavaleri et al.*, 2007] solve the action balance equation (see Eq (1.185) by *Komen et al.* [1994] and Eq (2.71) by *Janssen* [2004]) for the wave action density N (a function of the Cartesian co-ordinate $\mathbf{x}$, frequency f and direction θ) as follows,

$$\left(\frac{\partial}{\partial t} + \frac{\partial \Omega}{\partial \mathbf{k}} \cdot \frac{\partial}{\partial \mathbf{x}} - \frac{\partial \Omega}{\partial \mathbf{x}} \cdot \frac{\partial}{\partial \mathbf{k}} \right) N = S'_{\text{in}} + S'_{\text{nl}} + S'_{\text{ds}}. \quad (1)$$

Here, the right-hand source terms refer to wind input (in), nonlinear transfer (nl), and dissipation due to wave breaking (ds), respectively. The gradient in frequency represents shoaling and refraction, and $\Omega = \sigma + \mathbf{k} \cdot \mathbf{u}$ is the absolute frequency as seen by an observer standing still, whereas σ is the intrinsic frequency as seen by an observer moving with the current. We also note that

$$\frac{\partial \Omega}{\partial \mathbf{k}} \equiv \mathbf{c}_{\text{g}} + \mathbf{u}. \quad (2)$$

The wave action density is related to the wave variance density through $N = F/\sigma$. In deep water with no current refraction Eq (1) reduces to the energy balance equation,

$$\frac{\partial F}{\partial t} + \nabla \cdot (\mathbf{c}_{\text{g}} F) = S_{\text{in}} + S_{\text{nl}} + S_{\text{ds}}, \quad (3)$$

written here in flux form. Note that the source terms in Eq (3) are related to those in the action balance equation (1) as $S = \sigma S'$.

2.2. The air-side stress modified by surface waves

The presence of an undulating surface affects the roughness felt by the airflow. The atmospheric momentum flux to the oceanic wave field is denoted τ_{in}. It is convenient to define an air-side friction velocity in relation to the total air-side stress, τ_{a}, as

$$u_*^2 = \tau_{\text{a}}/\rho_{\text{a}}. \quad (4)$$

Here, ρ_{a} is the surface air density. *Charnock* [1955] was the first to relate the roughness of the sea surface to the friction velocity,

$$z_0 = \alpha_{\text{CH}} \frac{u_*^2}{g}, \quad (5)$$

where α_{CH} is known as the Charnock constant. *Janssen* [1989] showed that α_{CH} is not constant but varies with the sea state,

$$\alpha_{\text{CH}} = \frac{\hat{\alpha}_{\text{CH}}}{\sqrt{1 - \tau_{\text{in}}/\tau_{\text{a}}}}, \quad (6)$$

where $\hat{\alpha}_{\text{CH}} = 0.006$ [*Bidlot*, 2012] and the wave-induced stress, τ_{in}, is related to the wind input to the wave field as

$$\boldsymbol{\tau}_{\text{in}} = \rho_{\text{w}} g \int_0^{2\pi} \int_0^\infty \frac{\mathbf{k}}{\omega} S_{\text{in}} \, d\omega \, d\theta. \quad (7)$$

Here ρ_{w} is the water density and $\omega = 2\pi f$ is the circular frequency which when we ignore currents coincides with the intrinsic frequency σ. The wave-modified drag coefficient is then

$$C_{\text{D}} = \frac{\kappa^2}{\log^2(10/z_0)}, \quad (8)$$

where $\kappa = 0.4$ is von Kármán's constant. Note that the drag coefficient as defined here is related to the 10-m *neutral* wind speed, $U_{10\text{N}}$. This drag coefficient is computed by ECWAM. The Charnock parameter (6) is the main coupling mechanism between the atmosphere and the wave field in IFS, in place since 1998 [*Janssen*, 2004].

2.3. The water-side stress modified by surface waves

As the wind increases, the wave field responds by first growing, thus storing more momentum. In this phase there is a net influx of momentum to the wave field. Then, as the waves mature and the breaking intensifies, the momentum flux from the wave field to the ocean starts to close on the flux from the atmosphere to the waves. This is the equilibrium state where dissipation matches wind input, also referred to as fully developed windsea (since the waves cannot become higher), see e.g. *Komen et al.* [1994]; *World Meteorological Organization* [1998]; *Holthuijsen* [2007]. Finally, as the wind dies down, there will be a net outflux of momentum from the wave field, almost all of which will go to the ocean.

If wind input and dissipation in the wave field were in equilibrium, the air-side stress would be equal to the total water-side stress. However, most of the time waves are not in equilibrium [*Janssen*, 2012; *Janssen et al.*, 2013], giving

differences in air-side and water-side stress of the order of 5–10%, with occasional departures much larger in cases where the wind suddenly slackens. Likewise, in cases with sudden onset of strong winds the input from the wind field will be much larger than the dissipation to the ocean, lowering the stress to values well below 70% of its normal ratio to the air-side stress. The water-side stress is defined as the total atmospheric stress minus the momentum absorbed by the wave field (positive) minus the momentum injected from breaking waves to the ocean (negative), $\boldsymbol{\tau}_{\mathrm{oc}} = \boldsymbol{\tau}_{\mathrm{a}} - \boldsymbol{\tau}_{\mathrm{in}} - \boldsymbol{\tau}_{\mathrm{ds}}$. This can be written [ECMWF, 2013]

$$\boldsymbol{\tau}_{\mathrm{oc}} = \boldsymbol{\tau}_{\mathrm{a}} - \rho_{\mathrm{w}} g \int_0^{2\pi} \int_0^\infty \frac{\mathbf{k}}{\omega}(S_{\mathrm{in}} + S_{\mathrm{ds}})\, \mathrm{d}\omega \mathrm{d}\theta. \quad (9)$$

The stress from waves is archived as a normalized quantity and is applied as a factor to the air-side stress in our implementation in NEMO.

2.4. The turbulent kinetic energy flux from breaking waves

Craig and Banner [1994], CB94 hereafter, demonstrated that as waves break they will considerably modify the vertical dissipation profile from the traditional law-of-the-wall where dissipation $\propto z^{-1}$ [*Stull*, 1988]. With wave breaking CB94 found dissipation $\propto z^{-3.4}$. *Terray et al.* [1996] and *Drennan et al.* [1996] later demonstrated that the observed dissipation rates under breaking waves are indeed much higher than anticipated by the law of the wall. CB94's model has since been extended to a two-equation turbulence model by *Burchard* [2001] who demonstrated that the injection of turbulent kinetic energy from breaking waves was sufficient to successfully model the evolution of the mixed layer representative of North Sea conditions. CB94 suggested that the flux of turbulence kinetic energy (TKE) should be related to the water-side friction velocity w_* as

$$\Phi_{\mathrm{oc}} = \rho_{\mathrm{w}} \alpha_{\mathrm{CB}} w_*^3. \quad (10)$$

CB94 assumed that α_{CB} was a constant ~ 100, but noted that the range would probably be between 50 and 150, depending on the sea state (see also *Mellor and Blumberg* 2004). The TKE flux from breaking waves is related (see e.g. *Janssen et al.* 2004; *Rascle et al.* 2006; *Janssen* 2012; *Janssen et al.* 2013) to the dissipation source function of a spectral wave model as

$$\Phi_{\mathrm{oc}} = -\rho_{\mathrm{w}} g \int_0^{2\pi} \int_0^\infty S_{\mathrm{ds}}\, \mathrm{d}\omega \mathrm{d}\theta = -\rho_{\mathrm{a}} m u_*^3. \quad (11)$$

For consistency we have written the energy flux *from* the waves (thus always negative), $m \approx -\sqrt{\rho_{\mathrm{a}}/\rho_{\mathrm{w}}}\, \alpha_{\mathrm{CB}}$, normalized by the air friction velocity u_*. A diagnostic spectral tail proportional to ω^{-5} has been applied above a cutoff frequency ω_{w} [*Komen et al.*, 1994; *ECMWF*, 2013].

In NEMO the energy flux from breaking waves is introduced as a boundary condition to the TKE equation, which with Reynolds averages can be written

$$\frac{\mathrm{D}e}{\mathrm{D}t} = \frac{g}{\rho_{\mathrm{w}}}\overline{u_3'\rho'} - \overline{u_i'u_j'}\frac{\partial \overline{u}_i}{\partial x_j} - \frac{\partial}{\partial x_j}(\overline{u_j'e}) - \frac{1}{\rho_{\mathrm{w}}}\frac{\partial}{\partial x_i}(\overline{u_i'p'}) - \epsilon. \quad (12)$$

Here, $e \equiv q^2/2 = \overline{u_i'u_i'}/2$ is the TKE per unit mass (with q the turbulent velocity) and ϵ the dissipation rate (see e.g. *Stull* [1988] p 152). NEMO has the option of modelling the evolution of TKE with local closure (a prognostic equation in e only, see *Stull* 1988 pp 203–208 and *Pope* 2000 pp 369–373). Assuming that the advective terms are small in comparison and making the gradient transport approximation where turbulent coefficients are proportional to the

gradients in the mean quantities [*Stull*, 1988], we arrive at

$$\frac{\partial e}{\partial t} = K_{\mathrm{m}}S^2 - K_\rho N^2 + \frac{\partial}{\partial z}(K_q \frac{\partial e}{\partial z}) - c_\epsilon \frac{e^{3/2}}{l_\epsilon}. \quad (13)$$

This is the standard one-equation formulation for NEMO (*Madec and the NEMO team* 2012, pp 176–177). Here l_ϵ is the mixing length, the buoyancy term is assumed proportional to the local Brunt-Väisälä frequency,

$$N^2 = -\frac{g}{\rho}\frac{\partial \rho_{\mathrm{w}}}{\partial z}, \quad (14)$$

and the shear production is related to the shear of the mean flow,

$$S^2 = \left(\frac{\partial \overline{\mathbf{u}}}{\partial z}\right)^2. \quad (15)$$

Finally, the dissipation term follows *Kolmogorov* [1942] with a mixing length given by a relation by *Blanke and Delecluse* [1993]. See also Eq (10.6) by *Madec and the NEMO team* [2012]. NEMO also has the option to include a Langmuir source term following a parameterization by *Axell* [2002]. We will return to this in Sec 3.

If we assume, as *Mellor and Blumberg* [2004] do, that in the wave-affected layer the mixing length can be set to a constant $l_{\mathrm{w}} = \kappa z_{\mathrm{w}}$ where the surface roughness length relates to the significant wave height H_{s} as $z_{\mathrm{w}} = 0.5H_{\mathrm{s}}$, and that in this near-surface region diffusion balances dissipation, the TKE equation takes a simple exponential solution [see Eq (10) by *Mellor and Blumberg* 2004],

$$e(z) = e_0 \exp(2\lambda z/3). \quad (16)$$

This allows the following simple boundary condition

$$e_0 = \frac{1}{2}\,(15.8\,\alpha_{\mathrm{CB}})^{2/3}\,\frac{|\boldsymbol{\tau}_{\mathrm{oc}}|}{\rho_{\mathrm{w}}}. \quad (17)$$

The length scale λ^{-1} is sea-state dependent,

$$\lambda = [3/(S_q B \kappa^2)]^{1/2} z_{\mathrm{w}}^{-1}. \quad (18)$$

We have assumed $S_q = 0.2$ and $B = 16.6$ [*Mellor and Yamada*, 1982], as used in NEMO. For a wave height of 2.5 m, which is close to the global mean, $\lambda^{-1} \approx 0.5\,\mathrm{m}$.

Since e varies rapidly with depth, we want to reduce the boundary value e_1 by weighting the surface value (e_0) by the thickness of the uppermost level to attain an average value more representative of the turbulence intensity of the topmost model level,

$$e_1 = \frac{1}{L}\int_{-L}^0 e(z)\, \mathrm{d}z. \quad (19)$$

Here $L = \Delta z_1/2$ is the depth of the T-point of the first level. This weighting is essential with model configurations with a thick uppermost level, e.g. ORCA1L42 as discussed here ($L = 5$ m). Integrating Eq (16) is straightforward, and the average TKE boundary condition (19) becomes

$$e_1 = e_0 \frac{3}{2\lambda L}\left[1 - \exp(-2\lambda L/3)\right]. \quad (20)$$

It is worth noting that the exponential profile assumed by *Mellor and Blumberg* [2004] is only valid very near the surface, and in fact CB94 had already found the solution to the more general case where the mixing length is allowed to vary with depth. The consequence is that the mixing penetrates about twice as deep as in the case where the exponential approximation assumed by *Mellor and Blumberg*

[2004]. We have not implemented this operationally, but preliminary tests suggest that the effect is to roughly double the depth over which the TKE from breaking waves is distributed. The derivation is presented in the appendix.

For clarity we note that the normalized flux of TKE, m in Eq (11) is an operational output parameter in ECWAM and ERA-Interim and will be referred to as PHIOC.

2.5. The Stokes-Coriolis effect

Waves set up a Lagrangian drift $\mathbf{v}_s$ in the down-wave direction known as the Stokes drift [*Stokes*, 1847]. Although its velocity decays rapidly with depth, it can be substantial near the surface ($|\mathbf{v}_s| \sim 0.7\,\mathrm{m\,s^{-1}}$). In combination with the earth's rotation it adds an additional veering to the upper-ocean currents known as the Stokes-Coriolis force [*Hasselmann*, 1970],

$$\frac{D\mathbf{u}}{Dt} = -\frac{1}{\rho}\nabla p + (\mathbf{u} + \mathbf{v}_s) \times f\hat{\mathbf{z}} + \frac{1}{\rho}\frac{\partial \boldsymbol{\tau}}{\partial z}. \tag{21}$$

Here f is the Coriolis frequency, $\hat{\mathbf{z}}$ is the upward unit vector, p is the pressure and $\boldsymbol{\tau}$ is the stress. The full two-dimensional spectrum is in principle required to compute the Stokes drift velocity profile [*Janssen et al.*, 2004; *Janssen*, 2012],

$$\mathbf{v}_s(z) = 4\pi \int_0^{2\pi} \int_0^\infty f\mathbf{k}e^{2kz}F(f,\theta)\,\mathrm{d}f\,\mathrm{d}\theta. \tag{22}$$

This is computationally demanding and access to the full two-dimensional wave spectra from a numerical wave model (see e.g. *ECMWF* 2013) is not always feasible. It is therefore customary to introduce a simplified, monochromatic Stokes drift profile (see e.g., *Carniel et al.* [2005]; *Polton et al.* [2005]; *Saetra et al.* [2007]; *Tamura et al.* [2012]). However, it was shown by *Breivik et al.* [2013b, 2014] that this profile is a poor match to the full profile and that the following parameterization gives a considerable improvement,

$$\mathbf{v}_e = \mathbf{v}_0 \frac{e^{2k_e z}}{1 - 8k_e z}. \tag{23}$$

The surface Stokes drift velocity vector $\mathbf{v}_0$ is computed by ECWAM and is available both in ERA-Interim [*Dee et al.*, 2011] and from the operational forecasts of ECMWF.

The transport T_s under such a profile involves the exponential integral E_1 [*Abramowitz and Stegun*, 1972] and can be solved analytically [*Breivik et al.*, 2014] to yield

$$T_s = \frac{|\mathbf{v}_0|e^{1/4}E_1(1/4)}{8k_e}. \tag{24}$$

This imposes the following constraint on the wavenumber,

$$k_e = \frac{|\mathbf{v}_0|e^{1/4}E_1(1/4)}{8T_s}. \tag{25}$$

Here $E_1(1/4) \approx 1.34$, thus

$$k_e \approx \frac{|\mathbf{v}_0|}{5.97T_s}. \tag{26}$$

The n-th order spectral moment is defined as

$$m_n = \int_0^{2\pi}\int_0^\infty f^n F(f,\theta)\,\mathrm{d}f\,\mathrm{d}\theta. \tag{27}$$

The mean frequency is defined as $\overline{f} = m_1/m_0$ [*World Meteorological Organization*, 1998; *Holthuijsen*, 2007] and the significant wave height $H_s = 4\sqrt{m_0}$. We can derive the first moment from the integrated parameters of a wave model or

from wave observations and find an estimate for the Stokes transport,

$$\mathbf{T}_s \approx \frac{2\pi}{16}\overline{f}H_{m_0}^2\hat{\mathbf{k}}_s. \tag{28}$$

Here $\hat{\mathbf{k}}_s = (\sin\theta_s, \cos\theta_s)$ is the unit vector in the direction θ_s of the Stokes transport. We approximate the Stokes transport direction by the surface Stokes drift (see *Breivik et al.* [2014]). From Eqs (26)–(28) it is clear that in order to compute the Stokes drift velocity profile at the desired vertical levels we need H_s, $\overline{f}$ and $\mathbf{v}_0$.

The Stokes-Coriolis force is implemented as a tendency in the momentum equation. The strength of the Stokes drift velocity is estimated from the surface Stokes drift velocity, $\mathbf{v}_0 = \mathbf{v}_s(z=0)$, which is computed by ECWAM. The transport is computed according to Eq (28).

3. Ocean-only Forced Model Experiments

The NEMO model is run on a tripolar ORCA $1°$ grid configuration with 42 vertical levels. The uppermost level is 10 m thick. The model is coupled to LIM2, a two-level thermodynamic-dynamic sea ice model [*Fichefet and Maqueda*, 1997; *Bouillon et al.*, 2009] and is relaxed weakly towards a climatology in temperature (3-yr e-folding time). No sea surface temperature (SST) relaxation is performed. The ORCA grid is such that the resolution is increased towards the Equator (roughly $1/3°$) to better resolve tropical waves (see *Madec and the NEMO team* [2012] for details on the ORCA grid).

The atmospheric and wave forcing fields have been computed from the ERA-Interim reanalysis [*Simmons et al.*, 2007; *Dee et al.*, 2011]. ERA-Interim is a continuously updated atmospheric and wave field reanalysis starting in 1979. The resolution of the wave model is $1.0°$ on the Equator but the resolution is kept approximately constant globally through the use of a quasi-regular latitude-longitude grid where grid points are progressively removed toward the poles [*Janssen*, 2004]. A similar scheme applies for the atmospheric model, but here the resolution is approximately $0.75°$ at the Equator and the model fields are archived on a reduced Gaussian grid. The wave parameters are interpolated from the ECWAM grid to the ORCA grid. Where ECWAM has ice or land, but NEMO has open water, the ECMWF drag law [*Janssen*, 2008; *Edson et al.*, 2013] was employed,

$$C_D(z=10\,\mathrm{m}) = (a + bU_{10}^{p_1})/U_{10}^{p_2}. \tag{29}$$

The coefficients are $a = 1.03 \times 10^{-3}$, $b = 0.04 \times 10^{-3}$, $p_1 = 1.48$ and $p_2 = 0.21$. Here U_{10} is the 10-m wind speed from ERA-Interim. Where ECWAM and NEMO agree on open water, the stress is computed from the drag coefficient of ECWAM,

$$\tau_a = \rho_a C_{DW}U_{10N}^2. \tag{30}$$

Here, U_{10N} is the neutral 10-m wind speed, available on the ECWAM grid. The conversion to water-side stress (where we account for the absorption and release of momentum by the wave field) is implemented as

$$\tau_{oc} = \tilde{\tau}\tau_a, \tag{31}$$

where $\tilde{\tau}$ is the ratio of water-side to air-side stress (see also Eq 31). It is this parameter which is archived by ERA-Interim.

A standard integration period covering the ERA-Interim period from 1979 up until the end of 2009 has been used in the following. A summary of the settings for the model runs

can be found in Tables 1 and 2. Four experiments are presented, all compared against control experiments (CTRL) where standard settings are used for NEMO. Note that these standard settings include the CB94 wave-enhanced mixing described in Sec 10.1 by *Madec and the NEMO team* [2012]. The stress in CTRL is computed using the ECMWF drag law (29). In all runs the NEMOVAR observation operator $\mathbf{y} = \mathcal{H}(\mathbf{x})$ relating model state $\mathbf{x}$ to observation space ($\mathbf{y}$) is applied also to integrations without data assimilation. This allows a comparison of model integrations against the large number of quality-controlled temperature and temperature-salinity profiles compiled in the EN3 data set [*Ingleby and Huddleston*, 2007]. Seasonal averages (DJF and JJA) over the period 1989-2008 are used to compare surface temperature fields. Three experiments are conducted where the wave effects are switched on independently.

The first experiment, **TAUOC**, uses the ECWAM drag coefficient and the TAUOC ratio to water-side stress described in Sec 2.3. The effect is confined mostly to areas with rapidly developing weather systems in the extra-tropics (Fig 1), where the sea state will be quite far from equilibrium. The experiment also computes the stress from ECWAM instead of using the parametric drag law (29). This leads to a slight weakening of the wind stress along the west coast of South America and along the coast of south-west Africa, leading to decreased upwelling. This is mainly a consequence of differences between the ECWAM drag coefficient and the drag law (29) caused by limited fetch near the coast. The overall effect is a slight reduction of the bias in the tropics compared to EN3 near-surface temperature measurements (0.1 K, not shown).

The second experiment, **WTKE**, introduces the TKE flux (11) from ECWAM (described in Sec 2.4). The differences found in the extra-tropics amount to more than 2 K (Fig 2). The large difference demonstrates that the standard settings of NEMO will overestimate the mixing due to waves, especially with coarse vertical resolution (cf Eq (19)). The improved mixing levels lead to a large reduction in the bias in the temperature in the upper 50 m.

The **STCOR** experiment introduces Stokes-Coriolis forcing from ECWAM as described in Sec 2.5. The largest impact (Fig 3) is found in areas with extra-tropical cyclones in combination with strong temperature gradients, such as across the Gulf Stream and the Kuro-Shio.

In addition, we have compared the results of another experiment called **LOW** where a law-of-the-wall formulation for the upper boundary condition on TKE is applied, i.e. a run with no enhanced mixing due to breaking waves. The motivation for this experiment is to get a lower bound on the mixing. Here, the difference between the WTKE and LOW is much smaller (not shown) than the difference between the CTRL experiment and WTKE, again suggesting that the CTRL experiment (which is the default setup of NEMO) has too vigorous mixing.

We now combine the three wave effects described above in one experiment. Fig 4 shows the standard deviation (upper curves) and the biases of the CTRL run and a wave run including all three wave effects. The most striking feature is the large-amplitude annual cycle observed for the bias of the CTRL run. This amplitude is much weaker for the run with wave effects, and the seasonality is not at all so clear. Due to the huge differences to the mixing in the runs with and without wave effects, the heat uptake of the ocean also differs significantly. Fig 5 shows the global total heat content anomaly relative to 1979 (the start of the period) for the experiment with wave effects (in green). The similarity with the ORAS4 reanalysis [*Balmaseda et al.*, 2013] is clear, and the trends almost identical. It is also clear that the impact of the wave mixing establishes itself within the first two years of the integration. This may have implications for seasonal integrations.

To further assess the impact on the surface temperature we now compare with OI_v2, an SST analysis by *Reynolds*

et al. [2002]. The comparison with a control run in Fig 6a reveals large biases, especially in the summer hemisphere. These biases are reduced when wave effects are included (Fig 6b), especially in the northern extra-tropics. This is mainly due to a more correct level of mixing. We have also compared with the ocean reanalysis ORAS4 [*Balmaseda et al.*, 2013], which is based on an earlier version of NEMO (v3.0), with observations assimilated using the NEMOVAR [*Mogensen et al.*, 2012a] 3D-VAR assimilation system. The reanalysis covers the period 1957 to present, with forcing provided by ERA-40 [*Uppala et al.*, 2005] and later ERA-Interim from 1979 and onwards. The long-term SST fields from ORAS4 are very similar to OI_v2 since a strong relaxation to the OI_v2 gridded SST was applied as a flux correction between December 1981 and December 2009 [*Balmaseda et al.*, 2013]. Consequently, the ORAS4 fields are very similar to OI_v2 and are not shown here. Furthermore, we compared the mixed layer depth (defined by the depth at which the density difference with the surface exceeds 0.01 kg m^{-3}) to the climatology of mixed layer depth presented by *de Boyer Montégut et al.* [2004]. The results (Fig 7) suggest that the impact on the winter hemisphere mixed layer from adding the wave effects is rather small and much smaller than the deviation from the observed climatology. However, the reduction in mixed layer depth in the winter hemisphere outside the subtropics is generally in the right direction, as can be seen by comparing the CTRL run and the run with wave effects (Fig 7b).

3.1. Mixing parameterizations in NEMO

The importance of mixing brings us to the ETAU mechanism, an influential tuning parameter in NEMO. This is an artificial increase of the mixing in NEMO (see *Madec and the NEMO team* [2012], Sec 10.1). The TKE boost is determined by the surface TKE through the relation

$$e_\tau = 0.05 e_1 \exp z/h_\tau \qquad (32)$$

where the depth scale h_τ can vary with longitude from 0.5 m at the Equator to 30 m poleward of $44°$ or be fixed at 10 m. The coefficient, here 0.05, can also be varied. It seems like ETAU acts as a parameterization for Langmuir turbulence since it facilitates deeper penetration of mixing from surface processes than what is normally assumed from breaking waves [*Grant and Belcher*, 2009; *Belcher et al.*, 2012].

NEMO has a parameterization for Langmuir turbulence following *Axell* [2002]. To test the relative impact of the two processes, we ran forced experiments with the Langmuir parameterization and ETAU switched off. As is evident from Fig 8, the Langmuir turbulence has only modest impact on the temperature in the mixed layer in the extra-tropics (50 m depth in the northern extra-tropics is shown in Fig 8). Switching off ETAU has a much larger impact on the mixing, both in terms of bias and random error. We conclude tentatively that the additional ETAU ad hoc mixing provided in NEMO does something very similar to what is expected from Langmuir mixing, namely to mix down from the surface to a level comparable to the mixed layer depth. The Langmuir parameterization implemented in NEMO, following *Axell* [2002], reaches a maximum near the middle of the mixed layer depth. The reasoning behind this is that the associated vertical velocity w_{LC} will peak at $H_{\text{LC}}/2$, half the maximum depth to which Langmuir cells penetrate, and it is parameterized as

$$w_{\text{LC}}(z) = c_{\text{LC}} v_{\text{s}} \sin\left(-\frac{\pi z}{H_{\text{LC}}}\right), 0 > z \geq H_{\text{LC}}. \qquad (33)$$

Here v_s is the surface Stokes drift speed and $c_{LC} = 0.15$ is a coefficient. *Axell* [2002], by making an analogy with the characteristic convective velocity scale [*D'Alessio et al.*, 1998] further assumes that the Langmuir production term to be added to the TKE equation (12) can be written

$$P_{LC}(z) = \frac{w_{LC}^3}{H_{LC}}. \tag{34}$$

However, this parameterization has the distinguishing feature that it will put most if not all of the enhanced turbulence deep into the mixed layer and nothing near the surface. This explains why the impact of the current Langmuir parameterization on temperature profiles (Fig 8) is so much smaller than that from the exponential ETAU term. This is very different from parameterizations involving the shear of the Stokes drift profile v_s [*Polton and Belcher*, 2007; *Grant and Belcher*, 2009] which will parameterize the Langmuir production term as

$$-\overline{\mathbf{u}'w'} \cdot \frac{\partial \mathbf{v}_s}{\partial z}. \tag{35}$$

Here, $\mathbf{u}'$ is the horizontal Eulerian velocity fluctuation and w' the vertical. Due to the strong shear of the Stokes drift profile this would add a larger contribution near the surface. The vertical structure of (35) is similar to the ETAU profile (32).

4. The Coupled Atmosphere-Wave-Ocean Model

Coupling between the wave model and the ocean model was first implemented operationally in the ensemble suite of the IFS in Cycle 40R1 in November 2013, but limited to the mixing (WTKE) and Stokes-Coriolis forcing (STCOR). The seasonal integrations described here include in addition the modified stress (TAUOC) and the ice model LIM2 but are run at lower spatial resolution than the operational ensemble forecasts. Fields are exchanged every three hours (the coupling timestep) between IFS/ECWAM and NEMO. The atmospheric model is run with a spectral truncation of T255 (corresponding to roughly 78 km) with 91 vertical levels to 1 Pa. ECWAM is run at $1.5°$ resolution while NEMO is run on the ORCA $1°$ grid described in Sec 3. Fig 9 shows a flow chart outlining the sequence of execution of the various components of the IFS-ECWAM-NEMO single executable over two coupling timesteps, which can be summarized as follows.

1. The atmospheric component (IFS) is integrated (internal time step 2,700 s) one coupling time step (10,800 s), yielding wind fields for ECWAM as well as radiation and evaporation minus precipitation fields for NEMO

2. ECWAM (internal time step 900 s) is tightly coupled to IFS and gives sea surface roughness for the atmospheric boundary layer at every atmospheric time step. After one NEMO coupling time step, ECWAM also gives Stokes drift velocity, turbulent kinetic energy and waterside stress to NEMO

3. NEMO is integrated (internal time step 3,600 s) one coupling time step, yielding SST and surface currents to IFS

4. All model components have now been integrated one coupling time step (10,800 s), and the sequence begins anew

The coupling between the different components is described in more detail by *Mogensen et al.* [2012b]. Here we compare a setup for seasonal integrations to seven months, with three ensemble members starting from 1 May and 1 November for the period 1993-2012. The CTRL experiment is run with a standard CB94 type wave mixing which corresponds to $\alpha_{CB} = 100$ (the NEMO parameter $e_{bb} = 67.83$), similar to the ocean-only CTRL experiment presented in

Sec 3. The wind stress is computed using the ECMWF drag law (29) and 10-m wind vectors from IFS. The wave experiment includes the three processes TAUOC, WTKE and STCOR described in Sec 2 and Sec 3. Fig 10 reveals dramatic differences in the bias in the northern extra-tropics relative to ERA-Interim for the northern summer, June to August (JJA). Panel (a) shows the bias of the CTRL run, with large cold biases in the boreal summer in the northern extra-tropics. These biases are broadly similar to what was found from the forced (ocean-only) runs presented in Sec 3 (cf Fig 2). Panel (b) shows a strong reduction in the bias in the extra-tropics for the run with wave effects. There is a certain deterioration of the upwelling area along the coast of Baja California, but the cold bias in the eastern equatorial Pacific (the "cold tongue") is reduced slightly. The lead time is one to three months from a start date at the start of May. The results are similar for the southern hemisphere summer, December-February (DJF), although the bias reduction is not as strong as for the northern hemisphere. The seasonal variation of the bias found for the forced (ocean only) runs in Fig 4 is also present in the coupled integrations, see Fig 11. Again, the bias is greatly reduced in the wave run.

5. Discussion and conclusion

We have introduced three wave effects in NEMO, namely the sea-state dependent water-side stress, the energy flux from breaking waves and the Stokes-Coriolis force. Using ocean-only integrations and experiments with a coupled system consisting of the atmospheric model IFS, the wave model ECWAM and NEMO, we demonstrated that the impact of the wave effects is particularly noticeable in the extra-tropics. Of the three processes, the modification of the mixing has the largest impact (Fig 2), although the impact of the modified stress and Stokes-Coriolis is also significant (on the order of 0.5 K locally, see Figs 1 and 3). In ocean-only integrations we see a reduction of the temperature bias in the mixed layer, particularly in the extra-tropical summer (Fig 11). This manifests itself in a more realistic oceanic heat uptake (Fig 5). The coupled seasonal integrations show a similar reduction in bias compared to ERA-Interim (Figs 4 and 10).

The ocean-only integrations and coupled seasonal integrations all suggest that a right level of mixing is very important for reducing the temperature bias in the upper part of the ocean and also for the oceanic heat uptake. An important result is that introducing wave-enhanced mixing must be done in such a way that the thickness of the uppermost layer is accounted for. This is done with the present implementation by weighting with the thickness of the layer. This would not be necessary if a Neumann-type boundary condition had been used for the flux, but this is not the case in NEMO, which uses the Dirichlet-type formulation for the surface TKE first proposed by *Mellor and Blumberg* [2004]. This demonstrates that the introduction of wave effects is non-trivial but important for getting the mixing processes near the surface right. The impact of mixing on SST is clearly shown in Fig 6 where runs with and without wave effects are compared with OI_v2. That the seasonal cycle is much distorted by too vigorous mixing is clear, and Fig 4 shows that the annual cycle in biases extends well below the surface. This has implications for the long-term behavior of an ocean model and for the heat uptake of the ocean (see Fig 5). The conclusions from the ocean-only experiments that temperature biases are reduced by introduction of wave-induced mixing are borne out by the seasonal coupled integrations which essentially show the same bias reduction (Fig 10).

The results are of interest for climate projections [*Fan and Griffies*, 2014], and a natural next step would be to investigate the impact of waves on long, decadal to century-wide integrations (see also the Co-ordinated Ocean-Wave Climate Projections (COWCLIP) initiative, *Hemer et al.* [2012]). One candidate for forcing ocean-only integrations would be the recently completed ERA 20th century reanalysis (ERA-20C, see *Poli et al.* 2013, *Hersbach et al.* 2013, *de Boisséson et al.* 2014, and *Dee et al.* 2014). This opens up the possibility of running century-long NEMO integrations with wave effects from a state-of-the-art version of ECWAM [*Bidlot*, 2012] since all relevant parameters have been archived in the new reanalysis. For coupled climate-range integrations, the nearest candidate would be EC-Earth [*Hazeleger et al.*, 2010, 2012] which operates a modified version of an earlier cycle of IFS. Such experiments would help determining the importance of waves in the climate system, rather than just the impact of climate change on the wave climate [*Hemer et al.*, 2013].

Appendix A: The dissipation profile

The exponential profile (16) for the balance of

$$\frac{\partial}{\partial z}\left(lqS_q\frac{\partial e}{\partial z}\right) = \frac{q^3}{Bl} \quad \text{(A1)}$$

assumed by *Mellor and Blumberg* [2004] is only valid very near the surface where the mixing length can be assumed constant $= \kappa z_{\mathrm{w}}$. CB94 presented the solution to the more general case where the mixing length is allowed to vary with depth. This equation has a power-law solution [cf CB94, Eq (23)],

$$e(z) = e_0\left(\frac{z_{\mathrm{w}}}{z_{\mathrm{w}} - z}\right)^{2n/3} \quad \text{(A2)}$$

where

$$n = \left(\frac{3}{S_q\kappa^2 B}\right)^{1/2} = 2.4. \quad \text{(A3)}$$

This leads to a slightly more complicated expression for the vertical average (19),

$$e_1 = e_0\frac{z_{\mathrm{w}}}{L(2n/3 - 1)}\left[1 - \left(1 + \frac{L}{z_{\mathrm{w}}}\right)^{-2n/3+1}\right]. \quad \text{(A4)}$$

than Eq (20). The consequence is that the mixing penetrates about twice as deep as in the case where the exponential approximation assumed by *Mellor and Blumberg* [2004].

References

Abramowitz, M., and I. A. Stegun (Eds.) (1972), *Handbook of Mathematical Functions, with Formulas, Graphs, and Mathematical Tables*, 1064 pp., Dover, New York.

Ardhuin, F., and A. Jenkins (2006), On the Interaction of Surface Waves and Upper Ocean Turbulence, *J Phys Oceanogr*, *36*, 551–557, doi:10.1175/2009JPO2862.1.

Axell, L. B. (2002), Wind-driven internal waves and Langmuir circulations in a numerical ocean model of the southern Baltic Sea, *J Geophys Res*, *107*(C11), 20, doi:10.1029/2001JC000922.

Babanin, A. V. (2006), On a wave-induced turbulence and a wave-mixed upper ocean layer, *Geophys Res Lett*, *33*(20), 6, doi:10.1029/2006GL027308.

Babanin, A. V., and B. K. Haus (2009), On the existence of water turbulence induced by nonbreaking surface waves, *J Phys Oceanogr*, *39*(10), 2675–2679, doi:10.1175/2009JPO4202.1.

Babanin, A. V., A. Ganopolski, and W. R. Phillips (2009), Wave-induced upper-ocean mixing in a climate model of intermediate complexity, *Ocean Model*, *29*(3), 189–197, doi:10.1016/j.ocemod.2009.04.003.

Balmaseda, M. A., K. Mogensen, and A. T. Weaver (2013), Evaluation of the ECMWF ocean reanalysis system ORAS4, *Q J R Meteorol Soc*, *139*(674), 1132–1161, doi:10.1002/qj.2063.

Belcher, S. E., et al. (2012), A global perspective on Langmuir turbulence in the ocean surface boundary layer, *Geophys Res Lett*, *39*(18), 9, doi:10.1029/2012GL052932.

Bidlot, J.-R. (2012), Present status of wave forecasting at ECMWF, in *Workshop on Ocean Waves, 25-27 June 2012. Available online at http://www.ecmwf.int/publications/*, p. 15.

Blanke, B., and P. Delecluse (1993), Variability of the Tropical Atlantic Ocean Simulated by a General Circulation Model with Two Different Mixed Layer Physics, *J Phys Oceanogr*, *23*, 1363–1388, doi:10/c3hndq.

Blumberg, A. F., and G. L. Mellor (1987), A description of a three-dimensional coastal ocean circulation model, in *Three-Dimensional Coastal Ocean Models*, edited by N. S. Heaps, AGU Coastal and Estuarine Series 4, American Geophysical Union, Washington D C.

Bouillon, S., M. Á. Morales Maqueda, V. Legat, and T. Fichefet (2009), An elastic-viscous-plastic sea ice model formulated on Arakawa B and C grids, *Ocean Model*, *27*(3), 174–184, doi:10.1016/j.ocemod.2009.01.004.

Breivik, Ø., and A. A. Allen (2008), An operational search and rescue model for the Norwegian Sea and the North Sea, *J Marine Syst*, *69*(1–2), 99–113, arXiv:1111.1102, doi:10.1016/j.jmarsys.2007.02.010.

Breivik, Ø., A. Allen, C. Maisondieu, and M. Olagnon (2013a), Advances in Search and Rescue at Sea, *Ocean Dynam*, *63*(1), 83–88, doi:10/jtx.

Breivik, Ø., P. Janssen, and J. Bidlot (2013b), Approximate Stokes Drift Profiles in Deep Water, *ECMWF Technical Memorandum 716*, European Centre for Medium-Range Weather Forecasts.

Breivik, Ø., P. Janssen, and J. Bidlot (2014), Approximate Stokes Drift Profiles in Deep Water, *J Phys Oceanogr*, *44*(9), 2433–2445, arXiv:1406.5039, doi:10.1175/JPO-D-14-0020.1.

Broström, G., K. H. Christensen, M. Drivdal, and J. E. H. Weber (2014), Note on Coriolis-Stokes force and energy, *Ocean Dynam*, *64*(7), 1039–1045, doi:10.1007/s10236-014-0723-8.

Burchard, H. (2001), Simulating the wave-enhanced layer under breaking surface waves with two-equation turbulence models, *J Phys Oceanogr*, *31*(11), 3133–3145, doi:10/fvc4n5.

Carniel, S., M. Sclavo, L. H. Kantha, and C. A. Clayson (2005), Langmuir cells and mixing in the upper ocean, *Il Nuovo Cimento C Geophysics Space Physics C*, *28C*, 33–54, doi:10.1393/ncc/i2005-10022-8.

Cavaleri, L., et al. (2007), Wave modelling–The state of the art, *Prog Oceanogr*, *75*(4), 603–674, doi:10.1016/j.pocean.2007.05.005.

Cavaleri, L., B. Fox-Kemper, and M. Hemer (2012), Wind waves in the coupled climate system, *Bull Am Meteor Soc*, *93*(11), 1651–1661, doi:10.1175/BAMS-D-11-00170.1.

Charnock, H. (1955), Wind stress on a water surface, *Q J R Meteorol Soc*, *81*(350), 639–640.

Craig, P. D. (1996), Velocity profiles and surface roughness under breaking waves, *J Geophys Res*, *101*(C1), 1265–1277, doi:10.1029/95JC03220.

Craig, P. D., and M. L. Banner (1994), Modeling wave-enhanced turbulence in the ocean surface layer, *J Phys Oceanogr*, *24*(12), 2546–2559, doi:10/df29g2.

D'Alessio, S., K. Abdella, and N. McFarlane (1998), A new second-order turbulence closure scheme for modeling the oceanic mixed layer, *J Phys Oceanogr*, *28*(8), 1624–1641, doi:10/bwq3zv.

Davidson, F. J. M., et al. (2009), Applications of GODAE ocean current forecasts to search and rescue and ship routing, *Oceanography*, *22*(3), 176–181, doi:10.5670/oceanog.2009.76.

de Boisséson, E., M. A. Balmaseda, S. Abdalla, E. Källén, and P. A. E. M. Janssen (2014), How robust is the recent strengthening of the tropical pacific trade winds?, *Geophys Res Lett*, pp. 4398–4405, doi:10.1002/2014GL060257.

de Boyer Montégut, C., G. Madec, A. Fischer, A. Lazar, and D. Iudicone (2004), Mixed layer depth over the global ocean: An examination of profile data and a profile-based climatology, *J Geophys Res*, *109*(C12), 20, doi:10.1029/2004JC002378.

Dee, D., et al. (2011), The ERA-Interim reanalysis: Configuration and performance of the data assimilation system, *Q J R Meteorol Soc*, *137*(656), 553–597, doi:10.1002/qj.828.

Dee, D., M. Balmaseda, G. Balsamo, R. Engelen, A. Simmons, and J.-N. Thépaut (2014), Toward a consistent reanalysis of the climate system, *Bull Am Meteor Soc*, *95*, 1235–1248, doi:10.1175/BAMS-D-13-00043.1.

Drennan, W., M. Donelan, E. Terray, and K. Katsaros (1996), Oceanic turbulence dissipation measurements in SWADE, *J Phys Oceanogr*, *26*(5), 808–815, doi:10/dftwnb.

ECMWF (2013), IFS Documentation CY40r1, Part VII: ECMWF Wave Model, *ECMWF Model Documentation*, European Centre for Medium-Range Weather Forecasts.

Edson, J., et al. (2013), On the Exchange of Momentum over the Open Ocean, *J Phys Oceanogr*, *43*, 1589–1610, doi:10.1175/JPO-D-0173.1.

Fan, Y., and S. M. Griffies (2014), Impacts of parameterized Langmuir turbulence and non-breaking wave mixing in global climate simulations, *J Climate*, doi:10.1175/JCLI-D-13-00583.1.

Fan, Y., I. Ginis, and T. Hara (2009), The effect of wind-wave-current interaction on air-sea momentum fluxes and ocean response in tropical cyclones, *J Phys Oceanogr*, *39*(4), 1019–1034, doi:10.1175/2008JPO4066.1.

Fichefet, T., and M. A. M. Maqueda (1997), Sensitivity of a global sea ice model to the treatment of ice thermodynamics and dynamics, *J Geophys Res*, *102*(C6), 12,609–12,646, doi:10.1029/97JC00480.

Grant, A. L., and S. E. Belcher (2009), Characteristics of Langmuir turbulence in the ocean mixed layer, *J Phys Oceanogr*, *39*(8), 1871–1887, doi:10.1175/2009JPO4119.1.

Hackett, B., Ø. Breivik, and C. Wettre (2006), Forecasting the drift of objects and substances in the oceans, in *Ocean Weather Forecasting: An Integrated View of Oceanography*, edited by E. P. Chassignet and J. Verron, pp. 507–523, Springer, doi:10.1007/1-4020-4028-8_23.

Hasselmann, K. (1970), Wave-driven inertial oscillations, *Geophys Astrophys Fluid Dyn*, *1*(3-4), 463–502, doi:10.1080/03091927009365783.

Hasselmann, S., et al. (1988), The WAM model—a third generation ocean wave prediction model, *J Phys Oceanogr*, *18*, 1775–1810, doi:10/bhs3rr.

Hazeleger, W., et al. (2010), EC-earth: a seamless earth-system prediction approach in action, *Bull Am Meteor Soc*, *91*(10), 1357–1363, doi:10.1175/2010BAMS2877.1.

Hazeleger, W., et al. (2012), EC-Earth V2.2: description and validation of a new seamless earth system prediction model, *Climate Dynamics*, *39*(11), 2611–2629, doi:10.1007/s00382-011-1228-5.

Hemer, M. A., X. L. Wang, R. Weisse, and V. R. Swail (2012), Advancing wind-waves climate science: The COWCLIP project, *Bull Am Meteor Soc*, *93*(6), 791–796, doi:10.1175/BAMS-D-11-00184.1.

Hemer, M. A., Y. Fan, N. Mori, A. Semedo, and X. L. Wang (2013), Projected changes in wave climate from a multi-model ensemble, *Nature Climate Change*, *3*(5), 471–476, doi:10.1038/nclimate1791.

Hersbach, H., C. Peubey, A. Simmons, P. Poli, D. Dee, and P. Berrisford (2013), ERA-20CM: a twentieth century atmospheric model ensemble, *ERA Report Series 16*, European Centre for Medium-Range Weather Forecasts, http://www.ecmwf.int/publications.

Holthuijsen, L. (2007), *Waves in Oceanic and Coastal Waters*, 387 pp., Cambridge University Press.

Huang, C. J., F. Qiao, Z. Song, and T. Ezer (2011), Improving simulations of the upper ocean by inclusion of surface waves in the Mellor-Yamada turbulence scheme, *J Geophys Res*, *116*(C1), doi:10.1029/2010JC006320.

Ingleby, B., and M. Huddleston (2007), Quality control of ocean temperature and salinity profiles Historical and real-time data, *J Marine Syst*, *65*, 158–175, doi:10.1016/j.jmarsys.2005.11.019.

Janssen, P. (1989), Wave-induced stress and the drag of air flow over sea waves, *J Phys Oceanogr*, *19*(6), 745–754, doi:10/fsz7vd.

Janssen, P. (2004), *The interaction of ocean waves and wind*, 300 pp., Cambridge University Press, Cambridge, UK.

Janssen, P. (2008), Air-sea interaction through waves, in *ECMWF Workshop on Ocean-Atmosphere Interactions, 10-12 November 2008. Available online at http://www.ecmwf.int/publications/*, pp. 47–60.

Janssen, P. (2012), Ocean Wave Effects on the Daily Cycle in SST, *J Geophys Res*, *117*, 24, doi:10/mth.

Janssen, P., O. Saetra, C. Wettre, H. Hersbach, and J. Bidlot (2004), Impact of the sea state on the atmosphere and ocean, in *Annales hydrographiques*, vol. 3-772, pp. 3.1–3.23, Service hydrographique et océanographique de la marine.

Janssen, P., et al. (2013), Air-Sea Interaction and Surface Waves, *ECMWF Technical Memorandum 712*, European Centre for Medium-Range Weather Forecasts.

Jenkins, A. D. (1987), Wind and wave induced currents in a rotating sea with depth-varying eddy viscosity, *J Phys Oceanogr*, *17*, 938–951, doi:10/dwvq2.

Kantha, L. H., and C. A. Clayson (2004), On the effect of surface gravity waves on mixing in the oceanic mixed layer, *Ocean Model*, *6*(2), 101–124, doi:10.1016/S1463-5003(02)00062-8.

Kolmogorov, A. N. (1942), The equation of turbulent motion in an incompressible fluid, *Izv. Akad. Nauk SSSR, Ser. Fiz.*, *6*, 56–58.

Komen, G. J., L. Cavaleri, M. Donelan, K. Hasselmann, S. Hasselmann, and P. A. E. M. Janssen (1994), *Dynamics and Modelling of Ocean Waves*, 532 pp., Cambridge University Press, Cambridge.

Madec, G., and the NEMO team (2012), Nemo ocean engine v3.4, *Note du Pole de modélisation 27*, Institut Pierre Simon Laplace.

McWilliams, J., P. Sullivan, and C.-H. Moeng (1997), Langmuir turbulence in the ocean, *J Fluid Mech*, *334*(1), 1–30, doi:10.1017/S0022112096004375.

McWilliams, J. C., and J. M. Restrepo (1999), The Wave-driven Ocean Circulation, *J Phys Oceanogr*, *29*(10), 2523–2540, doi:10/dwj9tj.

McWilliams, J. C., and P. P. Sullivan (2000), Vertical mixing by Langmuir circulations, *Spill Science and Technology Bulletin*, *6*(3), 225–237, doi:10.1016/S1353-2561(01)00041-X.

Mellor, G., and A. Blumberg (2004), Wave breaking and ocean surface layer thermal response, *J Phys Oceanogr*, *34*(3), 693–698, doi:10/bftfk9.

Mellor, G. L., and T. Yamada (1982), Development of a turbulent closure model for geophysical fluid problems, *Rev Geophys Space Phys*, *20*, 851–875.

Mogensen, K., M. A. Balmaseda, and A. Weaver (2012a), The NEMOVAR ocean data assimilation system as implemented in the ECMWF ocean analysis for System 4, *ECMWF Technical Memorandum 668*, European Centre for Medium-Range Weather Forecasts.

Mogensen, K., S. Keeley, and P. Towers (2012b), Coupling of the NEMO and IFS models in a single executable, *ECMWF Technical Memorandum 673*, European Centre for Medium-Range Weather Forecasts.

Monahan, E. (1971), Oceanic whitecaps, *J Phys Oceanogr*, *1*, 139–144, doi:10/d7z784.

Poli, P., et al. (2013), The data assimilation system and initial performance evaluation of the ECMWF pilot reanalysis of the 20th-century assimilating surface observations only (ERA-20C), *ERA Report Series 14*, European Centre for Medium-Range Weather Forecasts, http://www.ecmwf.int/publications.

Polton, J. A. (2009), A wave averaged energy equation: Comment on "global estimates of wind energy input to subinertial motions in the Ekman-Stokes layer" by Bin Liu, Kejian Wu and Changlong Guan, *Journal of Oceanography*, *65*(5), 665–668, doi:10.1007/s10872-009-0057-1.

Polton, J. A., and S. E. Belcher (2007), Langmuir turbulence and deeply penetrating jets in an unstratified mixed layer, *J Geophys Res*, *112*(C9), 11, doi:10.1029/2007JC004205.

Polton, J. A., D. M. Lewis, and S. E. Belcher (2005), The role of wave-induced Coriolis-Stokes forcing on the wind-driven mixed layer, *J Phys Oceanogr*, *35*(4), 444–457, doi:10.1175/JPO2701.1.

Pope, S. B. (2000), *Turbulent flows*, 776 pp., Cambridge university press.

Qiao, F., Y. Yuan, Y. Yang, Q. Zheng, C. Xia, and J. Ma (2004), Wave-induced mixing in the upper ocean: Distribution and application to a global ocean circulation model, *Geophys Res Lett*, *31*(11), 4, doi:10.1029/2004GL019824.

Rascle, N., F. Ardhuin, and E. Terray (2006), Drift and mixing under the ocean surface: A coherent one-dimensional description with application to unstratified conditions, *J Geophys Res*, *111*(C3), 16, doi:10.1029/2005JC003004.

Reynolds, R. W., N. A. Rayner, T. M. Smith, D. C. Stokes, and W. Wang (2002), An improved in situ and satellite SST analysis for climate, *J Climate*, *15*(13), 1609–1625, doi:10/cdpxf6.

Ris, R. C., L. H. Holthuijsen, and N. Booij (1999), A third-generation wave model for coastal regions 2. Verification, *J Geophys Res*, *104*(C4), 7667–7681, doi: 10.1029/1998JC900123.

Röhrs, J., K. H. Christensen, F. Vikebø, S. Sundby, Ø. Saetra, and G. Broström (2014), Wave-induced transport and vertical mixing of pelagic eggs and larvae, *Limnol Oceanogr*, *59*, 1213–1227, doi:10.4319/lo.2014.59.4.1213.

Saetra, Ø., J. Albretsen, and P. Janssen (2007), Sea-State-Dependent Momentum Fluxes for Ocean Modeling, *J Phys Oceanogr*, *37*(11), 2714–2725, doi:10.1175/2007JPO3582.1.

Simmons, A., S. Uppala, D. Dee, and S. Kobayashi (2007), ERA-Interim: New ECMWF reanalysis products from 1989 onwards, *ECMWF newsletter*, *110*, 25–35.

Skyllingstad, E. D., and D. W. Denbo (1995), An ocean large-eddy simulation of Langmuir circulations and convection in the surface mixed layer, *J Geophys Res*, *100*(C5), 8501–8522, doi:10.1029/94JC03202.

Smyth, W. D., E. D. Skyllingstad, G. B. Crawford, and H. Wijesekera (2002), Nonlocal fluxes and Stokes drift effects in the K-profile parameterization, *Ocean Dynam*, *52*(3), 104–115, doi: 10.1007/s10236-002-0012-9.

Stokes, G. G. (1847), On the theory of oscillatory waves, *Trans Cambridge Philos Soc*, *8*, 441–455.

Stull, R. B. (1988), *An introduction to boundary layer meteorology*, 666 pp., Kluwer, New York.

Tamura, H., Y. Miyazawa, and L.-Y. Oey (2012), The Stokes drift and wave induced-mass flux in the North Pacific, *J Geophys Res*, *117*(C8), 14, doi:10.1029/2012JC008113.

Teixeira, M., and S. Belcher (2002), On the distortion of turbulence by a progressive surface wave, *J Fluid Mech*, *458*, 229–267, doi:10.1017/S0022112002007838.

Terray, E. A., M. A. Donelan, Y. C. Agrawal, W. M. Drennan, K. K. Kahma, A. J. W. III, P. A. Hwang, and S. A. Kitaigorodskii (1996), Estimates of kinetic energy dissipation under breaking waves, *J Phys Oceanogr*, *26*(5), 792–807.

Tolman, H. L. (1991), A Third-Generation Model for Wind Waves on Slowly Varying, Unsteady, and Inhomogeneous Depths and Currents, *J Phys Oceanogr*, *21*(6), 782–797.

Tolman, H. L., B. Balasubramaniyan, L. D. Burroughs, D. V. Chalikov, Y. Y. Chao, H. S. Chen, and V. M. Gerald (2002), Development and Implementation of Wind-Generated Ocean Surface Wave Models at NCEP, *Wea Forecasting*, *17*(2), 311–333, doi:10/d74ttq.

Uppala, S., P. Kållberg, A. Simmons, et al. (2005), The ERA-40 Re-analysis, *Q J R Meteorol Soc*, *131*, 2961–3012, doi: 10.1256/qj.04.176.

Weber, J. (1983), Steady Wind- and Wave-Induced Currents in the Open Ocean, *J Phys Oceanogr*, *13*, 524–530, doi: 10/djz6md.

World Meteorological Organization (1998), *Guide to wave analysis and forecasting*, World Meteorological Organization, Geneva, Switzerland, 2 ed.

Wu, J. (1979), Oceanic whitecaps and sea state, *J Phys Oceanogr*, *9*(5), 1064–1068, doi:10/bsjxrx.

Corresponding author: Øyvind Breivik, ECMWF, Shinfield Park, Reading, RG2 9AX, UK.
E-mail: oyvind.breivik@ecmwf.int. ORCID Author ID: 0000-0002-2900-8458.

Horizontal grid	ORCA 1°
Vertical resolution	42 levs (10 m top lev)
Time step	3600 s
Time period	1979-2009
Data assimilation	OFF
SST damping	OFF
3D damping to clim	ON
Bulk parameterization	COARE
Ice model	LIM2

Table 1. Overview of the settings common to all forced (ocean only) experiments.

Setting	Control exp (CTRL)	Wave exps (ALT)	Law of the wall (LOW)
Forcing	ERA-I	ERA-I plus wave forcing	ERA-I
TKE flux	`rn_ebb = 67.83`	ECWAM PHIOC	`rn_ebb = 0`
Drag coeff	ECMWF drag law	ECWAM CDWW	ECMWF drag law
Water-side stress	COARE	ECWAM TAUOC	COARE

Table 2. Overview of the settings of the control experiment, the wave experiments and the Law-of-the-wall experiment. PHIOC refers to the energy flux from ECWAM, TAUOC to the modification of the stress, and CDWW to the drag coefficient from ECWAM.
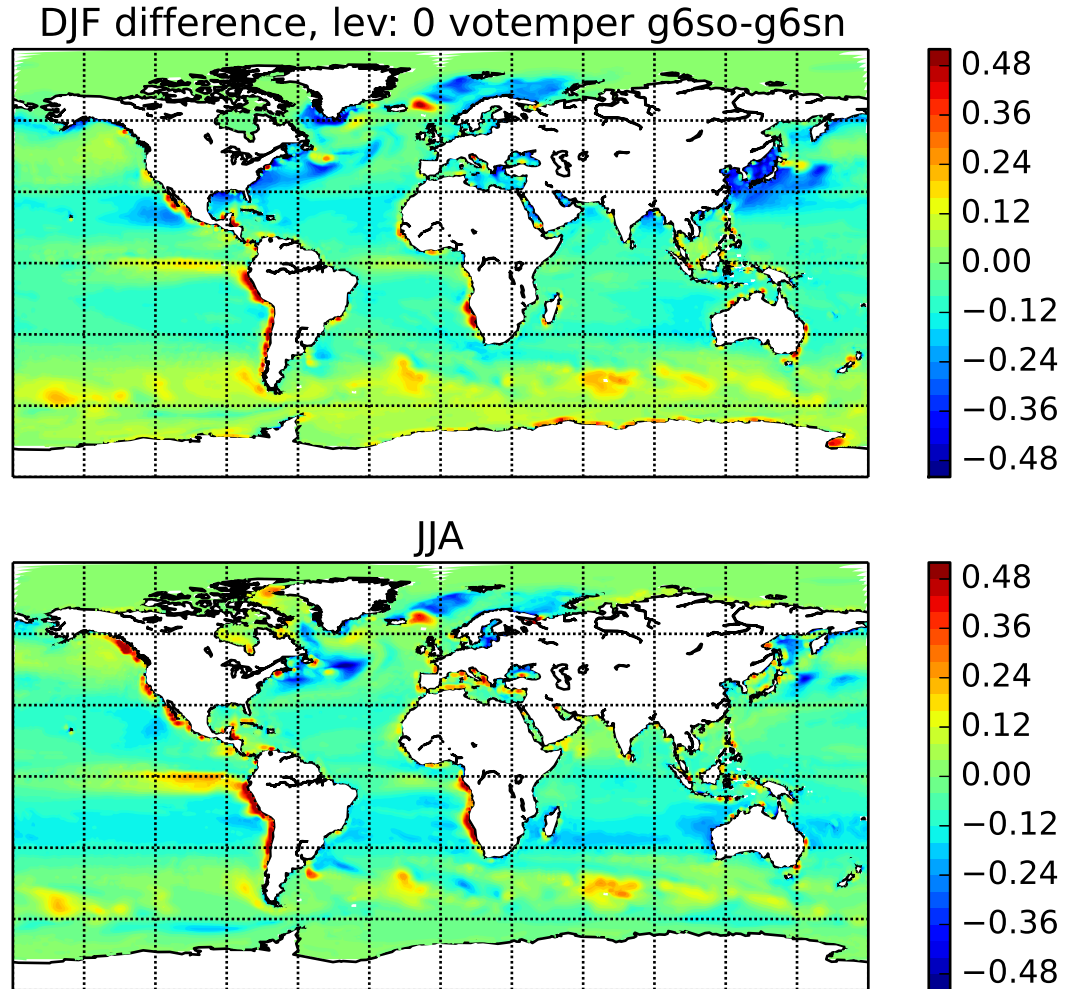
Figure 1. Long-term SST differences between a control run (g6sn) and a run with TAUOC and CDWW (g6so). The differences along the western coastlines of the American and African continents are related to differences in the drag coefficient from ECWAM and the drag law. This affects the level of upwelling somewhat. In the extra-tropics the largest differences are found in areas where rapidly evolving low pressure systems will affect the duration of wave growth. In the tropics, differences are most likely due to differences in the drag over swell compared to the parametric drag law used for the CTRL experiment.
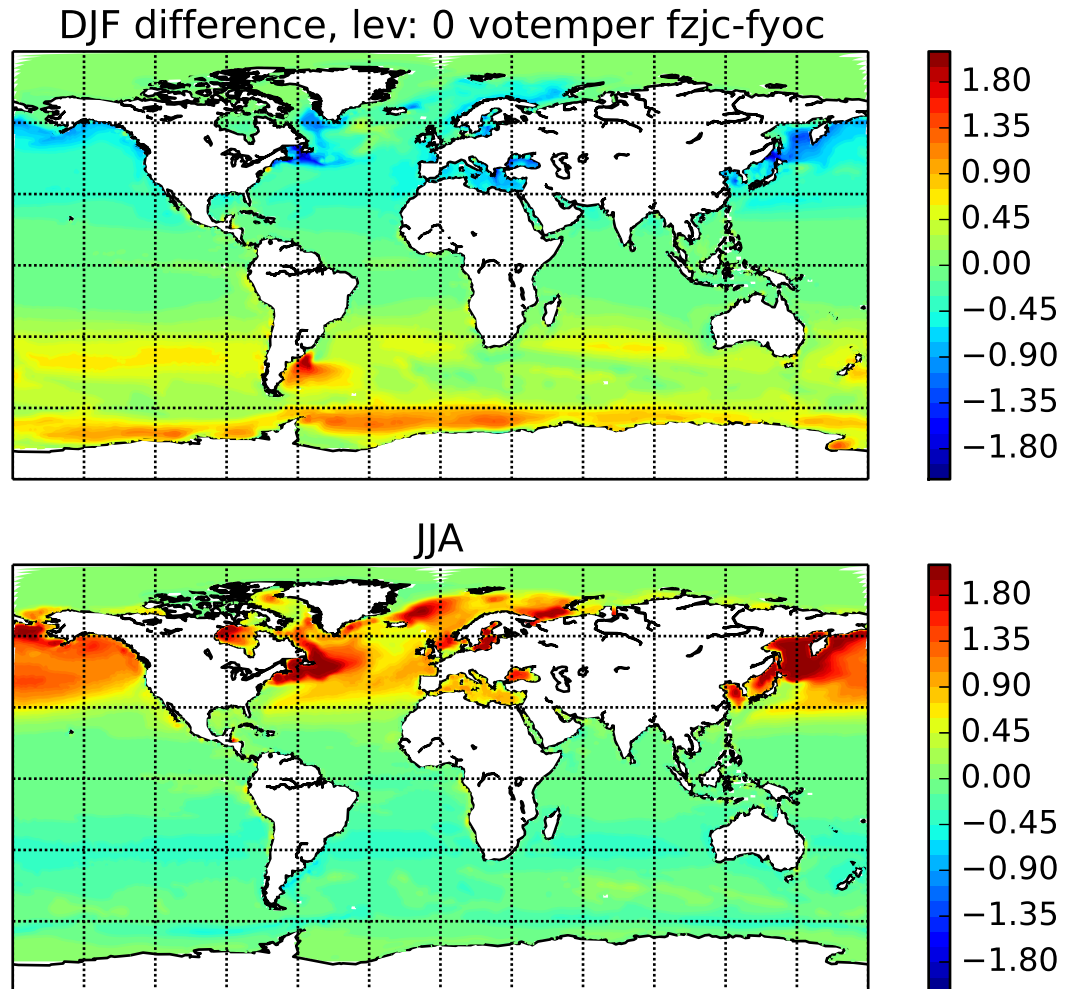
Figure 2. Long-term SST differences between a run with mixing determined by ECWAM (fzjc) and a control run (fyoc). The difference is found mostly in the extra-tropics and is much greater than that found for TAUOC and STCOR. Note that the color scale is ±2 K.
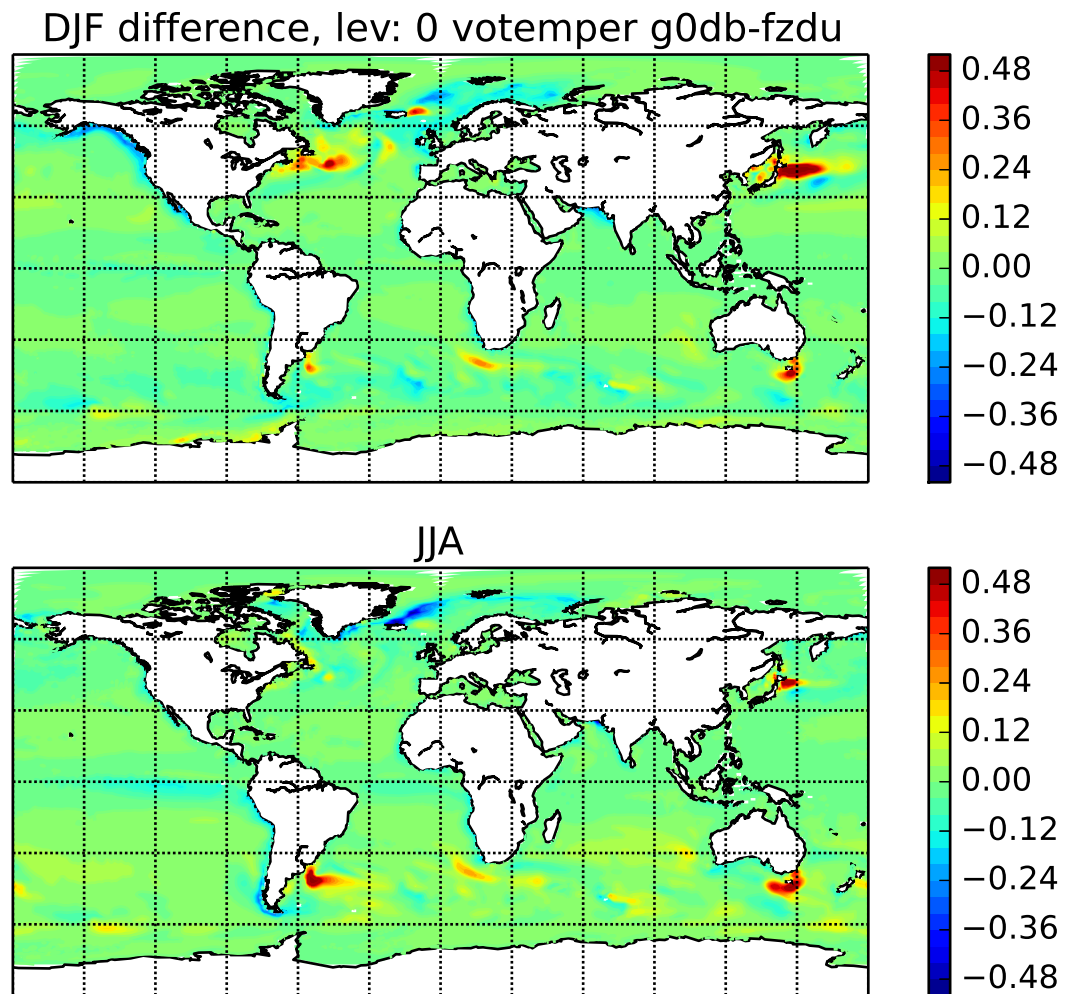
Figure 3. Long-term SST differences between a control run (experiment g0db) and a run with Stokes-Coriolis (STCOR, experiment fzdu). The differences are mostly found in the extra-tropics.
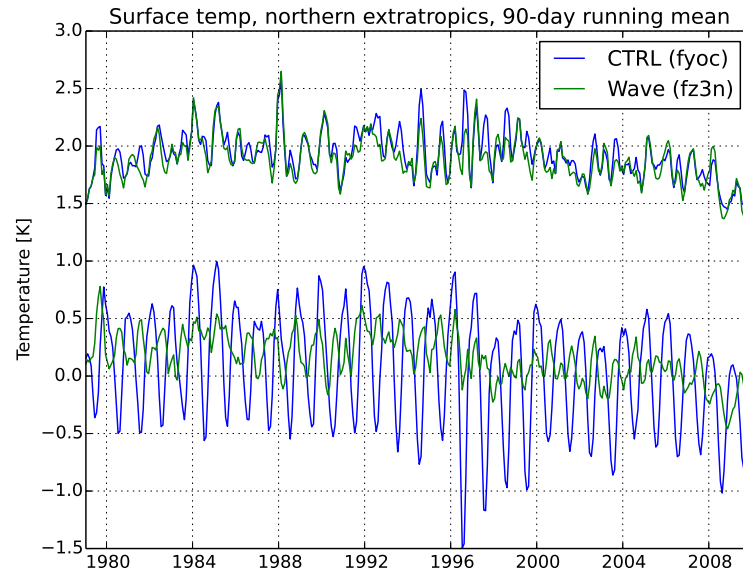
(a)
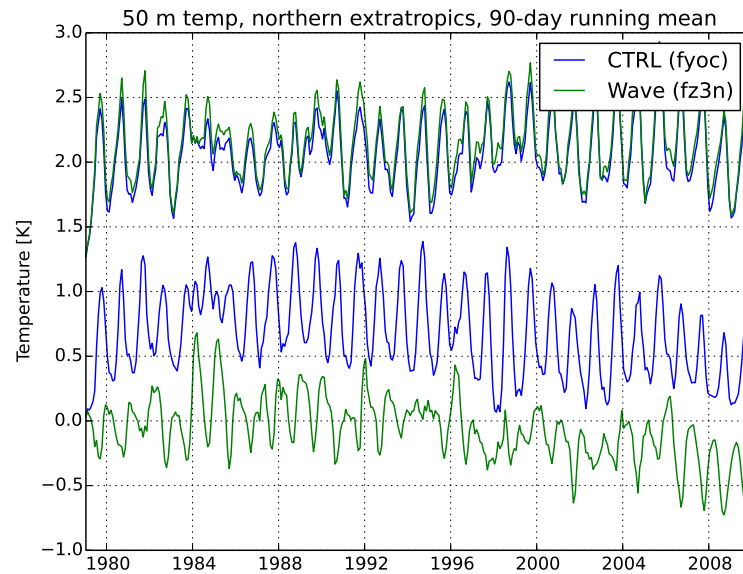
(b)

Figure 4. A comparison of surface (a) and 50 m depth (b) EN3 temperature observations [*Ingleby and Huddleston*, 2007] in the northern extra-tropics. The upper curves show the standard deviation while the lower curves represent the bias. A 90-day running mean is employed. The results reveal a striking difference in the seasonal variability of the bias with the CTRL run exhibiting a much stronger amplitude near the surface. Deeper down (Panel b, 50 m depth) the variability is still somewhat higher for the CTRL integration, and the bias is greatly reduced in the run with the wave effects.
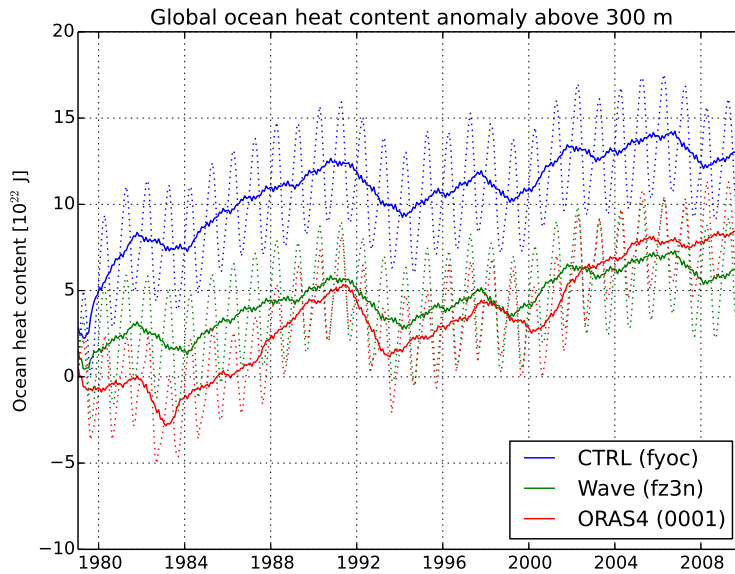
(a)
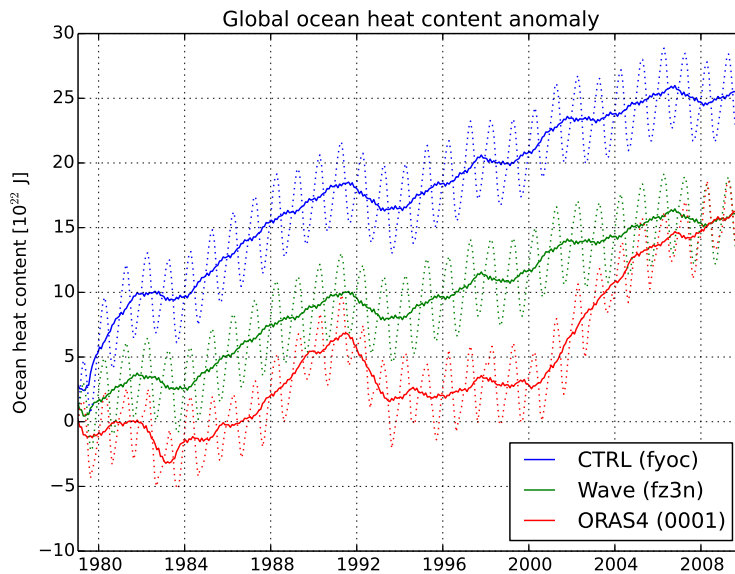
(b)

Figure 5. Panel a: The global ocean heat content anomaly (relative to the start of the time series) in the upper 300 m. The adjusted mixing due to introduction of wave dissipation rapidly manifests itself (green) and its impact is established within approximately two years from the start of the integration. The trend for the run with wave effects (full lines represent a 12-month moving average) is closer to that of the ORAS4 reanalysis (red). The pronounced annual cycle (dashed lines) is due to the difference in oceanic volume in the southern and northern hemispheres. Panel b: The levelling off in the later period is not as evident in the total ocean heat content. Again, the run with wave effects comes closer to the trend observed in ORAS4.
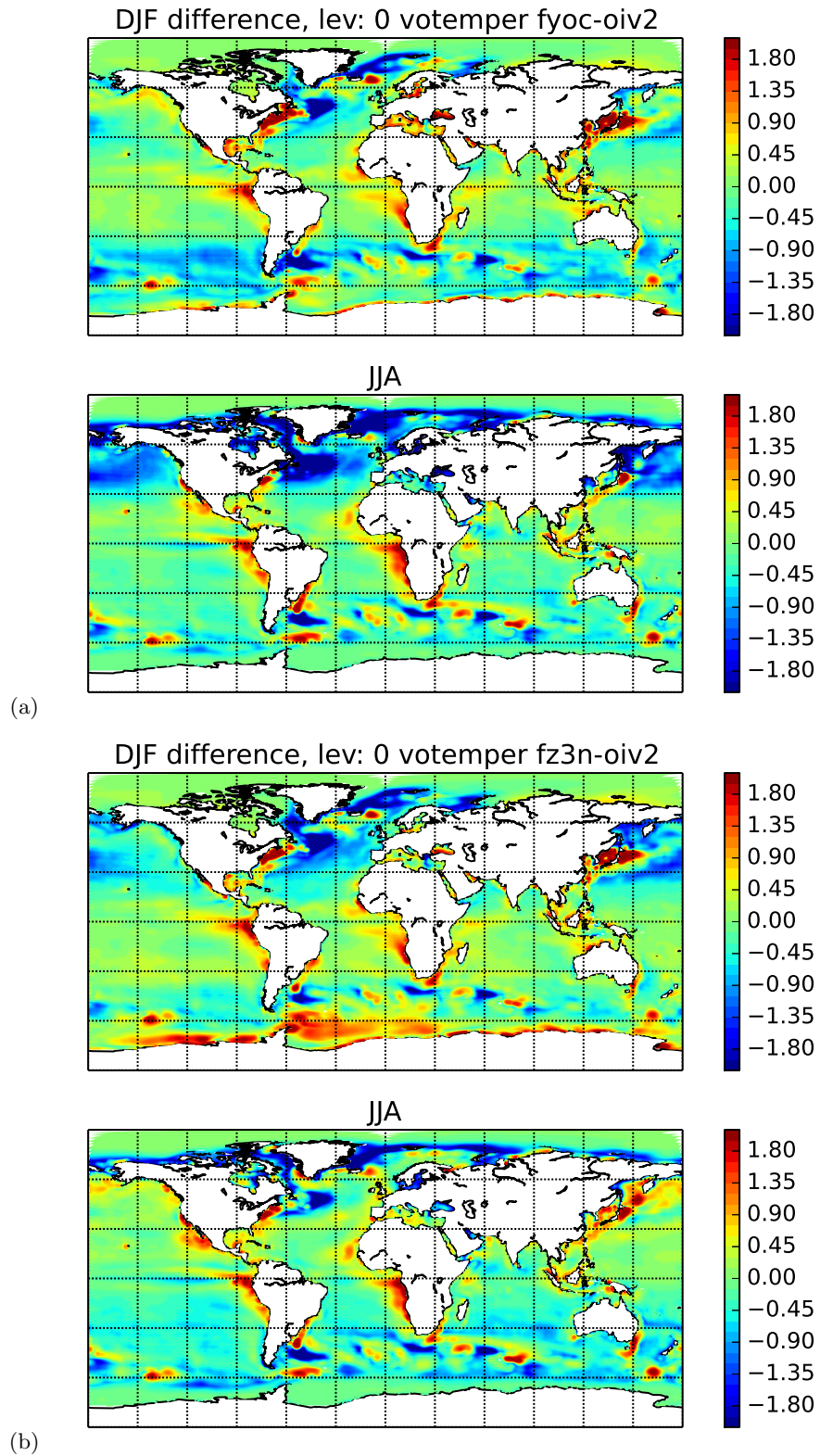
Figure 6. Panel a: Long-term SST differences between the Reynolds (2002) OI_v2 SST analysis and a control run (fyoc). The temperature biases are strongest in the summer hemisphere outside the tropics. Panel b: The temperature biases in the northern summer are reduced significantly in the run with wave effects included (fz3n).

(a)   (b)
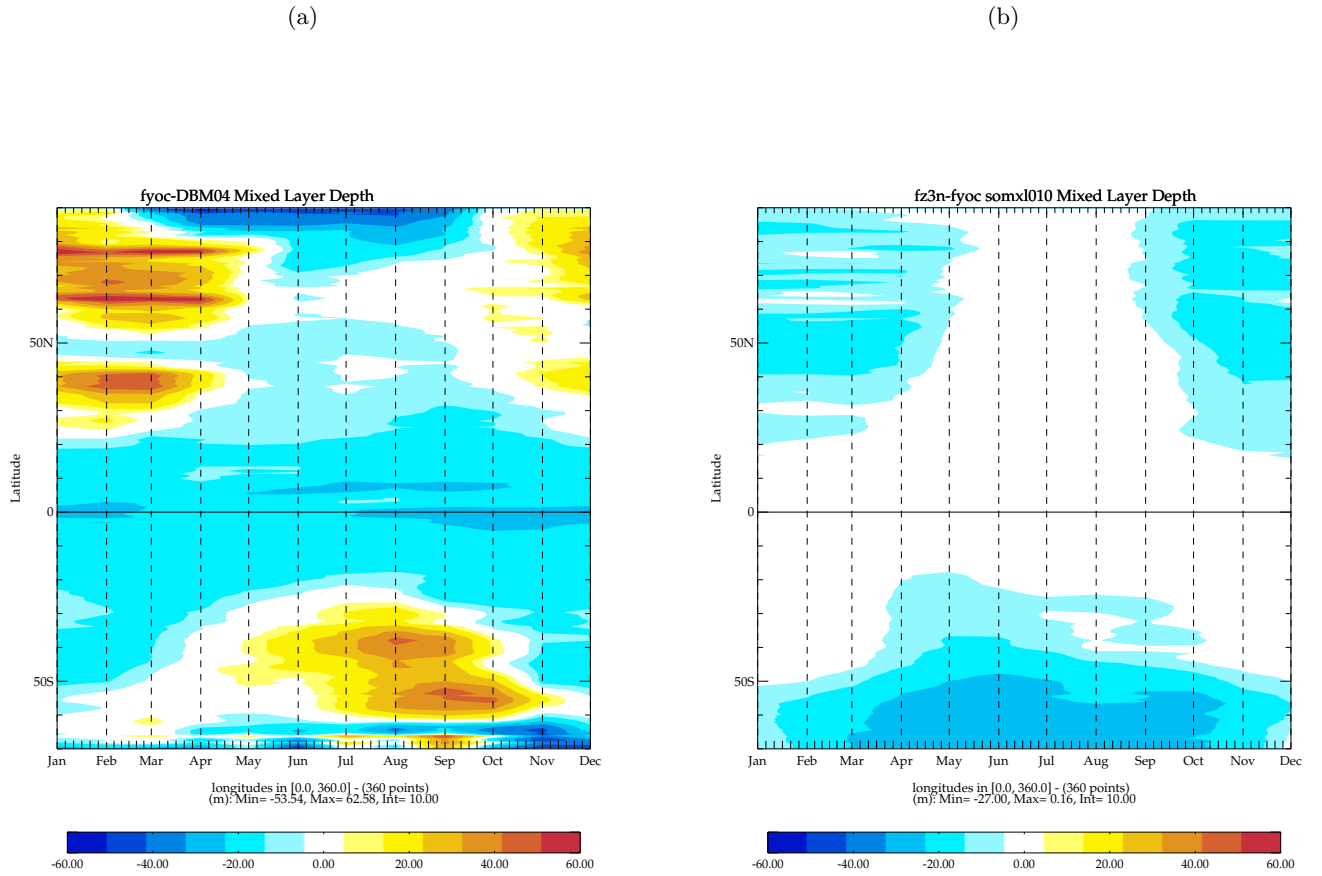
Figure 7. Panel a: Hovmöller diagram of the mixed layer depth of the CTRL (fyoc) run minus the climatology by *de Boyer Montégut et al.* [2004]. Although the definition of mixed layer depth differs it is clear that the CTRL tends to exaggerate the depth of the wintertime mixed layer in the extra-tropics. Panel b: A difference plot of the wave run (fz3n) minus the CTRL run shows a slight reduction in the depth of the mixed layer, but the differences are still much smaller than the absolute differences between the climatology and the model integrations.
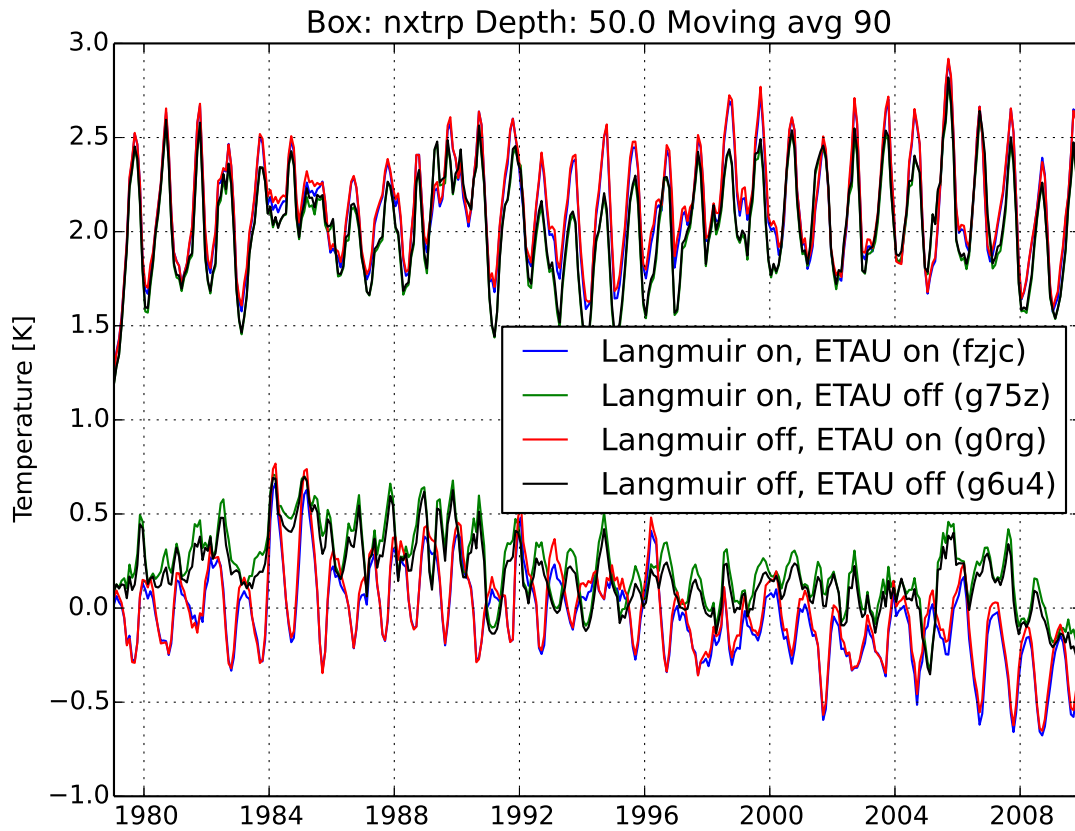
Figure 8. A comparison of the impact of ETAU, the parameterization for enhanced deep mixing in NEMO, and the Langmuir mixing parameterization by *Axell* [2002]. The northern extra-tropics (defined as north of 20° N) at 50 m depth is shown here. The blue curve shows the control experiment where both processes are switched on (default). Switching off the Langmuir mixing (red) is seen to have a much smaller impact than switching off the ETAU parameterization (green). Finally, a run where both processes are switched off (black) shows that the combined effect is again dominated by the ETAU parameterization. Modeled temperature is compared to EN3 temperature observations [*Ingleby and Huddleston*, 2007]. The upper curves show the standard deviation while the lower curves represent the bias. A 90-day running mean is employed.
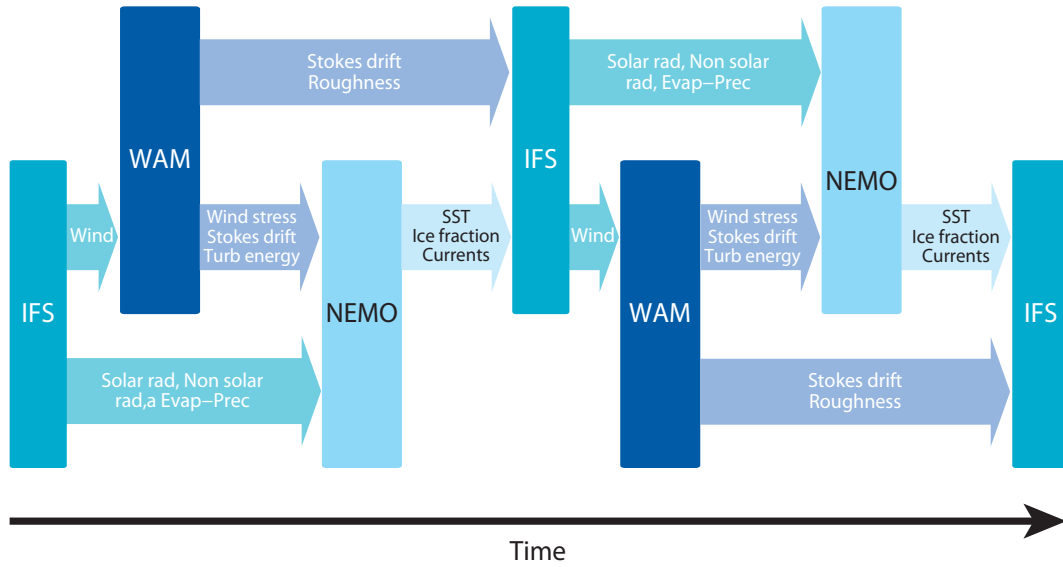
Figure 9. A flow chart of the coupling between the components of the single executable IFS-ECWAM-NEMO model setup. Two coupling time steps are shown to illustrate the sequence. This is how the operational ensemble prediction system has been run since Cycle 40R1 (November 2013). The seasonal integration experiments described here contain in addition the LIM2 ice model and are run at lower atmospheric resolution (T255). First the atmospheric component (IFS) is integrated (internal time step 2,700 s) one coupling time step (10,800 s), yielding wind fields for ECWAM as well as radiation and evaporation minus precipitation fields for NEMO. ECWAM (internal time step 900 s) is tightly coupled to IFS and gives sea surface roughness for the atmospheric boundary layer at every atmospheric time step. After one NEMO coupling time step, ECWAM also gives Stokes drift velocity, turbulent kinetic energy and waterside stress to NEMO. NEMO is integrated (internal time step 3,600 s) one coupling time step, yielding SST and surface currents to IFS. All model components have now been integrated one coupling time step (10,800 s), and the sequence begins anew with the next coupling time step.
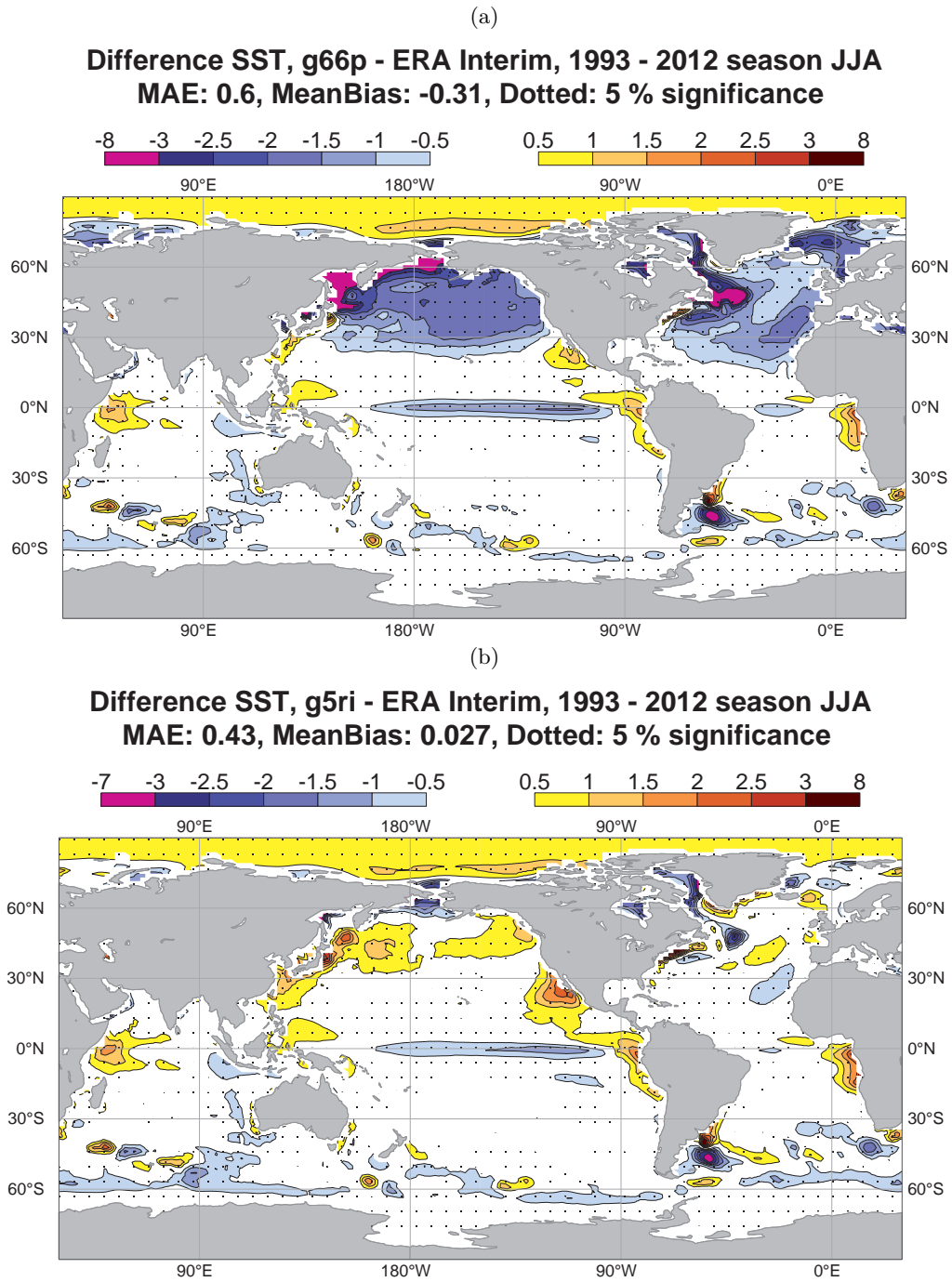
(a)

Difference SST, g66p - ERA Interim, 1993 - 2012 season JJA
MAE: 0.6, MeanBias: -0.31, Dotted: 5 % significance

(b)

Difference SST, g5ri - ERA Interim, 1993 - 2012 season JJA
MAE: 0.43, MeanBias: 0.027, Dotted: 5 % significance

Figure 10. Panel a: SST bias relative to ERA-Interim for the coupled seasonal CTRL run (JJA). The biases are substantial in the summer hemisphere. Panel b: Same for the wave run. Here, the biases are much smaller, although certain upwelling areas, most notably off the coast of California, seem to deteriorate a little. The "cold tongue" in the eastern equatorial Pacific is somewhat less pronounced.
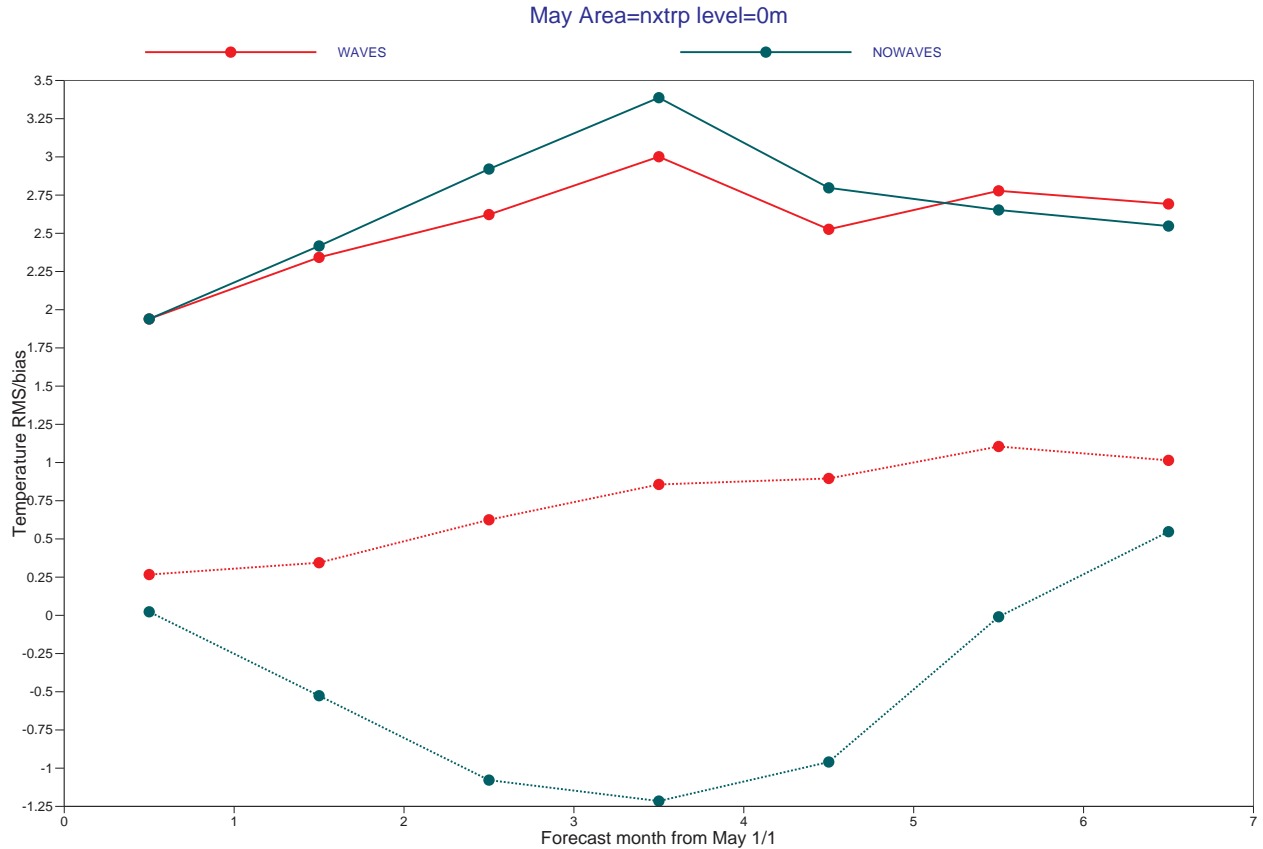
Figure 11. A comparison of surface EN3 temperature observations [*Ingleby and Huddleston*, 2007] in the northern extra-tropics for coupled integrations of IFS-ECWAM-NEMO as a function of lead time. The start date is 1 May. A three-member ensemble is run to a lead time of seven months for the years 1993–2008. The dashed red (lower) curve shows the bias of the integration with wave effects, and the green dashed curve shows the bias of the run without wave effects. A clear seasonal variation to the bias is visible for the run without wave effects. The upper full lines show that the root-mean-square (RMS) error is also reduced slightly with the introduction of the wave coupling.

Ocean wave effects on the daily cycle in SST

P. A. E. M. Janssen[1]

[1] Ocean waves play an important role in processes that govern the fluxes across the air-sea interface and in the upper-ocean mixing. Equations for current and heat are presented that include effects of ocean waves on the evolution of the properties of the upper ocean circulation and heat budget. The turbulent transport is modeled by means of the level-$2\frac{1}{2}$ Mellor-Yamada scheme, which includes an equation for the production and destruction of Turbulent Kinetic Energy (TKE). The TKE equation in this work includes production due to wave breaking, production due to wave-induced turbulence and/or Langmuir turbulence, effects of buoyancy and turbulent dissipation. As a first test, the model is applied to the simulation of the daily cycle in SST at one location in the Arabian sea for the period of October 1994 until October 1995. For this location, the layer where the turbulent mixing occurs, sometimes called the Turbocline, is only a few meters thick and fairly thin layers are needed to give a proper representation of the diurnal cycle. The dominant processes that control the diurnal cycle turn out to be buoyancy production and turbulent production by wave breaking, while in the deeper layers of the ocean the Stokes-Coriolis force plays an important role.

1. Introduction

[2] Monin-Obukhov similarity theory has played a central role in understanding turbulence in the planetary boundary layer. Essentially, this similarity theory is based on a balance between production of turbulence by work against a parallel shear flow, buoyancy and dissipation of turbulent kinetic energy. For air flow over the ocean there are, however, notable exceptions to this rule. Normally, when surface gravity waves are slower than the wind these waves will be generated by the wind hence these waves will extract energy and momentum from the airflow. This results in deviations from the classical Monin-Obukhov scaling as the balance between production and dissipation is perturbed by the presence of a finite vertical transport of the wave-induced pressure fluctuations [*Janssen*, 1999]. By the same token, when waves are propagating faster than the wind there is a small damping of the waves, which perturbs the Monin-Obukhov scaling as well [*Drennan et al.*, 1996].

[3] However, in the upper part of the ocean deviations from Monin-Obukhov scaling are much more extreme. The work of *Terray et al.* [1996] and *Craig and Banner* [1994] has highlighted the prominent role of breaking waves. In the field it is customary to find considerable deviations from the usual balance between production and dissipation of turbulent kinetic energy. These deviations are caused by the

energy flux produced by breaking waves. When observed turbulent kinetic energy dissipation, ϵ, and depth $|z|$ are scaled by parameters related to the wave field, an almost universal relation between dimensionless dissipation and dimensionless depth is found. Here, dimensionless dissipation is given by $\epsilon H_S/\Phi_{in}$, with H_S the significant wave height and Φ_{in} the energy flux from wind to waves, while the dimensionless depth is given by $|z|/H_S$. Whilst the classical Monin-Obukhov scaling would result in a turbulent dissipation that scales with the inverse of depth, in the upper ocean a much more sensitive dependence on depth and consequently much larger turbulent dissipation is found suggesting that indeed wave breaking plays an important role in the mixing of momentum and heat in the upper ocean.

[4] The energy flux by surface wave breaking is expected to affect the upper-ocean mixing up to a depth of the order of the significant wave height. Transport to the deeper layers of the ocean is possible because work against the shear in the Stokes drift generates Langmuir cells and wave-induced turbulence which have a penetration depth of the order of the inverse of a typical wave number of the wave field.

[5] In this paper I would like to develop a multi-layer model of turbulent mixing in the upper ocean that includes effects of surface wave damping, wave-induced turbulence and stratification in addition to the usual shear production and dissipation. The model is applied to the problem of the evolution of the diurnal cycle in SST, and it is shown that, even for low wind speed, wave effects play an important role in determining the amplitude of the diurnal cycle.

[6] The programme of the paper is as follows. In section 2 a brief discussion of the role of ocean waves in air-sea interaction is given while it is shown how to obtain in a

[1]ECMWF, Reading, UK.

Corresponding author: P. A. E. M. Janssen, ECMWF, Shinfield Park, Reading RG2 9AX, UK. (p.janssen@ecmwf.int)

reliable way energy and momentum flux from the wave field. Section 3 gives some of the details of the mixed layer model that is proposed to describe the mixing processes in the upper ocean. The model consists of momentum equations (which includes the Stokes-Coriolis force) and the heat equation. In the presence of turbulence these equations are not closed and the level-$2\frac{1}{2}$ Mellor-Yamada scheme is adopted to model the eddy viscosity for heat and momentum. These eddy viscosities are then found to depend on the turbulent kinetic energy (TKE) and hence the need for a TKE equation. In the present paper the TKE equation describes the rate of change of turbulent kinetic energy due to processes such as shear production (including shear in the Stokes drift), damping by buoyancy, vertical transport of pressure and TKE and dissipation of turbulence. It presents an ideal context to model effects of wave dissipation and wave-induced turbulence on the mixing properties of the upper ocean. In contrast to the Craig and Banner model effects of wave breaking on mixing are taken into account by following the fairly novel approach of explicitly modeling the vertical transport of pressure in terms of the rate of change of the wave spectrum due to wave dissipation (A similar idea in the atmospheric context was pursued by *Janssen* [1999]). The effect of Langmuir and/or wave-induced turbulence, following *Grant and Belcher* [2009], is represented by the part in the shear production term that is connected to the Stokes drift. The upper ocean may experience extremely stable conditions, especially during the day under low wind speed conditions; the modeling of these stable conditions therefore requires special attention. A model for buoyancy effects was developed which for weakly stable conditions is based on results from the Kansas field campaign (assuming that atmospheric and oceanic turbulence behaves in a similar fashion) while the modeling of extremely stable conditions was guided by the renormalization approach of *Sukoriansky et al.* [2005].

[7] In section 4 some properties of steady state solutions of the TKE equation are discussed. In particular, it is argued that to a good approximation diffusion of turbulent kinetic energy may be neglected. This approximation is called the *local* approximation because the turbulent kinetic energy then only depends on the local properties of the turbulent flow. In the local approximation it turns out that the TKE equation reduces to an algebraic problem and its solution indicates that the turbulent velocity (and hence the eddy viscosity) only weakly depends on the wave energy flux and the contribution by Langmuir turbulence (according to a 1/3-power law). Nevertheless, wave effects enhance the eddy viscosities by a factor of 2–3. Inspecting more closely the solution according to the local approximation it is found that wave dissipation affects the mixing process very close to the surface at a depth of the order of the significant wave height. Langmuir turbulence is found to affect mixing in the deeper parts of the upper ocean at a depth of the order of a typical wavelength of the ocean wave field. Also buoyancy effects are discussed in some detail. For weak stratification, the present model is shown to be in close agreement with the results of the Kansas field campaign [*Businger et al.*, 1971] while for extremely stable conditions it is found that momentum transport dominates heat transport, in agreement with *Sukoriansky et al.* [2005]. In addition, the combined

effects of waves and buoyancy are studied as well. It is found that under stable conditions buoyancy effects, which act in particular in the deeper parts of the upper ocean, suppress the effects of Langmuir turbulence. Finally, the TKE equation is shown to be in close agreement with the empirically known dependence of dimensionless turbulent dissipation on depth.

[8] In section 5 results of numerical simulations with the mixed layer model are presented. First, a synthetic example with constant momentum and heat fluxes is given, which is followed by a simulation of the sea surface temperature (SST) at a location in the Arabian Sea. The simulated diurnal cycle in SST is found to be in close agreement with in-situ observations. The importance of sea state effects, even for low wind speed cases, is shown as well. Finally, section 6 gives a summary of conclusions.

2. Surface Layer Mixing and Ocean Waves

[9] In order to be able to give a realistic representation of the mixing processes in the surface layer of the ocean, a reliable estimate of energy and momentum fluxes to the ocean column is required. A first attempt to estimate these fluxes from modeled wave spectra and knowledge about the generation and dissipation of ocean waves was given by *Komen* [1987], while *Weber* [1994] studied energy and momentum fluxes in the context of a low-resolution coupled ocean-wave atmosphere model (WAM-ECHAM).

[10] As energy and momentum flux depend on the spectral shape, the solution of the energy balance equation is required. It reads

$$\frac{\partial}{\partial t}F + \frac{\partial}{\partial \vec{x}} \cdot \left(\vec{v}_g F \right) = S_{in} + S_{nl} + S_{diss} + S_{bot}, \qquad (1)$$

where $F = F(\omega, \theta)$ is the two-dimensional wave spectrum which gives the energy distribution of the ocean waves over angular frequency ω and propagation direction θ. Furthermore, $\vec{v}_g$ is the group velocity and on the right hand side there are four source terms. The first one, S_{in} describes the generation of ocean waves by wind and therefore represents the momentum and energy transfer from air to ocean waves. The third and fourth term describe the dissipation of waves by processes such as white-capping, large scale breaking eddy-induced damping and bottom friction, while the second term denotes nonlinear transfer by resonant four-wave interactions. The nonlinear transfer conserves total energy and momentum and is important in shaping the wave spectrum and in the down-shift towards lower frequencies.

[11] Let us first define the momentum and energy flux. The total wave momentum $\vec{P}$ depends on the variance spectrum $F(\omega, \theta)$ and is defined as

$$\vec{P} = \rho_w g \int_0^{2\pi} \int_0^\infty d\omega d\theta \frac{\vec{k}}{\omega} F(\omega, \theta), \qquad (2)$$

which agrees with the well-known relation that wave momentum is wave energy divided by the phase speed of the waves. The momentum fluxes to and from the wave field are given by the rate of change in time of wave momentum, and one may distinguish different momentum fluxes depending on the different physical processes. For example, making use

of the energy balance equation (1) the wave-induced stress is given by

$$\vec{\tau}_{in} = \rho_w g \int_0^{2\pi} \int_0^\infty d\omega d\theta \frac{\vec{k}}{\omega} S_{in}(\omega, \theta), \qquad (3)$$

while the dissipation stress is given by

$$\vec{\tau}_{diss} = \rho_w g \int_0^{2\pi} \int_0^\infty d\omega d\theta \frac{\vec{k}}{\omega} S_{diss}(\omega, \theta), \qquad (4)$$

Similarly, the energy flux from wind to waves is defined by

$$\Phi_{in} = \rho_w g \int_0^{2\pi} \int_0^\infty d\omega d\theta S_{in}(\omega, \theta), \qquad (5)$$

and the energy flux from waves to ocean, Φ_{diss}, is given by

$$\Phi_{diss} = \rho_w g \int_0^{2\pi} \int_0^\infty d\omega d\theta S_{diss}(\omega, \theta). \qquad (6)$$

It is important to note that while the momentum fluxes are mainly determined by the high-frequency part of the wave spectrum, the energy flux is to some extent also determined by the low-frequency waves.

[12] In an operational wave model, the prognostic frequency range is limited by practical considerations such as restrictions on computation time, but also by the consideration that the high-frequency part of the dissipation source function is not well-known. In the ECMWF version of the WAM model the prognostic range of the wave spectrum is given by the condition

$$\omega < \omega_c = \max(2.5\omega_{mean}, 4\omega_{pm})$$

where ω_{mean} is a conveniently defined mean angular frequency and ω_{pm} is the Pierson Moskovitch frequency. In the diagnostic range, $\omega > \omega_c$, the wave spectrum is given by Phillips' ω^{-5} power law. In the diagnostic range it is assumed that there is a balance between wind input and dissipation. In practice this means that all energy and momentum going into the high-frequency range of the spectrum is dissipated, and is therefore directly transferred to the ocean column.

[13] The momentum flux to the ocean column, denoted by $\vec{\tau}_{oc}$, is the sum of the flux transferred by turbulence across the air-sea interface $\vec{\tau}_a - \vec{\tau}_{in}$ and the momentum flux transferred by the ocean waves due to wave breaking $\vec{\tau}_{diss}$. As a consequence, $\vec{\tau}_{oc} = \vec{\tau}_a - \vec{\tau}_{in} - \vec{\tau}_{diss}$. Utilizing the balance at the high-frequencies one finds

$$\vec{\tau}_{oc} = \vec{\tau}_a - \rho_w g \int_0^{2\pi} \int_0^{\omega_c} d\omega d\theta \frac{\vec{k}}{\omega}(S_{in} + S_{diss}), \qquad (7)$$

where $\vec{\tau}_a$ is the atmospheric stress, whose magnitude is given by $\tau_a = \rho_a u_*^2$ with u_* the air friction velocity. Alternatively, one may introduce the water friction velocity w_* in such a way that the magnitude of the ocean stress is given by $\tau_{oc} = \rho_w w_*^2$. In equilibrium, the second term on the right-hand side of (7) vanishes, hence $\tau_{oc} = \tau_a$, and in that case w_* and u_* are related according to $w_* = (\rho_a/\rho_w)^{1/2}u_*$.

[14] Ignoring the direct energy flux from air to currents, because it is small [cf. *Phillips*, 1977], the energy flux to the ocean, denoted by Φ_{oc}, is therefore given by $-\Phi_{diss}$. Utilizing the assumed high-frequency balance one therefore obtains

$$\Phi_{oc} = \Phi_{in} - \rho_w g \int_0^{2\pi} \int_0^{\omega_c} d\omega d\theta (S_{in} + S_{diss}), \qquad (8)$$

where Φ_{in} is the total energy flux transferred from air to ocean waves. This energy flux is fairly well-known, because empirically the wind input to ocean waves is well-known, even in the high-frequency part of the spectrum [cf. *Plant*, 1982]. Furthermore, there is now a consensus that the high-frequency part of the spectrum obeys an ω^{-5} power law [*Banner*, 1990; *Birch and Ewing*, 1986; *Hara and Karachintsev*, 2003] (to mention but a few references).

[15] Note that the ocean momentum flux $\vec{\tau}_{oc}$ and the energy flux Φ_{oc} only involve the sum of the source functions of the energy balance equation and therefore it only involves the total rate of change of wave momentum and wave energy. Noting furthermore that the wave energy is directly connected to the wave height while (at least in deep water) the wave momentum is directly connected to the first moment of the wave spectrum, i.e. the mean period, it can be concluded that any wave model that is forced by reliable atmospheric stresses and that produces wave height and mean period results that compare well with, for example, buoy wave height data and altimeter wave height data, will produce reliable estimates of the ocean momentum flux $\vec{\tau}_{oc}$ and the energy flux Φ_{oc}.

[16] Let us now illustrate the sea-state dependence of the momentum and energy flux for the simple case of the passage of a front. To that end take a single grid-point version of the ECMWF version of the WAM model and force the waves for the first day with a constant wind speed of 18 m/s, which is followed by a drop in wind speed to 10 m/s and a change in wind direction by 90 deg. In Figure 1 a plot is given of the time series of atmospheric stress (τ_a), momentum flux to the ocean (τ_{oc}), air-wave energy flux (Φ_{aw}) and the energy flux into the ocean (Φ_{oc}). The momentum fluxes have been normalized by τ_a, while the energy fluxes have been normalized by $m\rho_a u_*^3$, with $m = 4.5$ which is a convenient mean value. During the first day we deal with the case of wind-generated gravity waves, hence wind sea, and, in particular, the difference between atmospheric stress and the momentum flux to the ocean is small, most of the time at best 2%. This is a well-known property of wind sea [*Hasselmann et al.*, 1973]. For wind sea, the difference between input energy flux Φ_{in} and the energy flux into the ocean Φ_{oc} is somewhat larger. When the front passes at $T = 24$ hrs there is a sudden drop in wind, hence in atmospheric stress. However, the waves are still steep and experience an excessive amount of dissipation in such a way that wave energy decreases. As a consequence, considerable amounts of momentum and energy are transferred to the ocean column, much larger than the amounts one would expect from the local wind. Therefore, in cases of rapidly varying circumstances, the fluxes are seen to depend on the sea state. This is in particular true for the energy flux Φ_{oc} and to a much lesser extent for the momentum flux τ_{oc}.

[17] This different behavior of momentum flux and energy flux is caused by a combination of two factors. By definition momentum flux is mainly determined by the high frequency
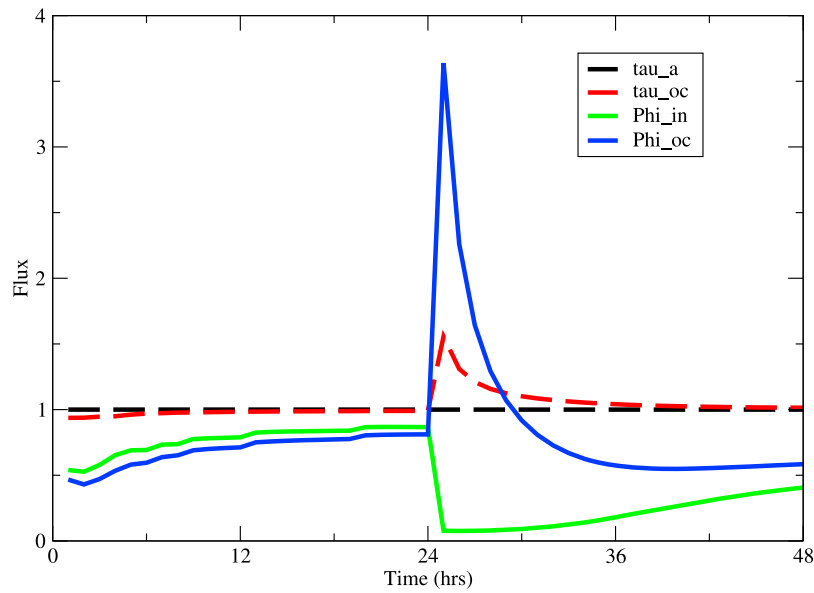
Figure 1. Evolution in time of normalized momentum flux and energy flux to the ocean for the case of a passing front after 24 hrs. The momentum flux has been normalized with $\rho_a u_*^2$, while the energy flux has been normalized with $m\rho_a u_*^3$, where $m = 4.5$.

part of the spectrum while we have assumed that in the unresolved part of the spectrum there is a balance between wind input and dissipation. Hence, for wind sea there is almost always a balance between atmospheric momentum flux and the flux into the ocean. This holds to a lesser extent

for the energy flux because this flux is partly determined by the low frequency part of the wave spectrum as well.

[18] The different behavior of momentum and energy flux is also found in the monthly means on a global scale. This is illustrated in Figures 2 and 3, which are obtained from analyzed spectra from the ERA-interim analysis for the
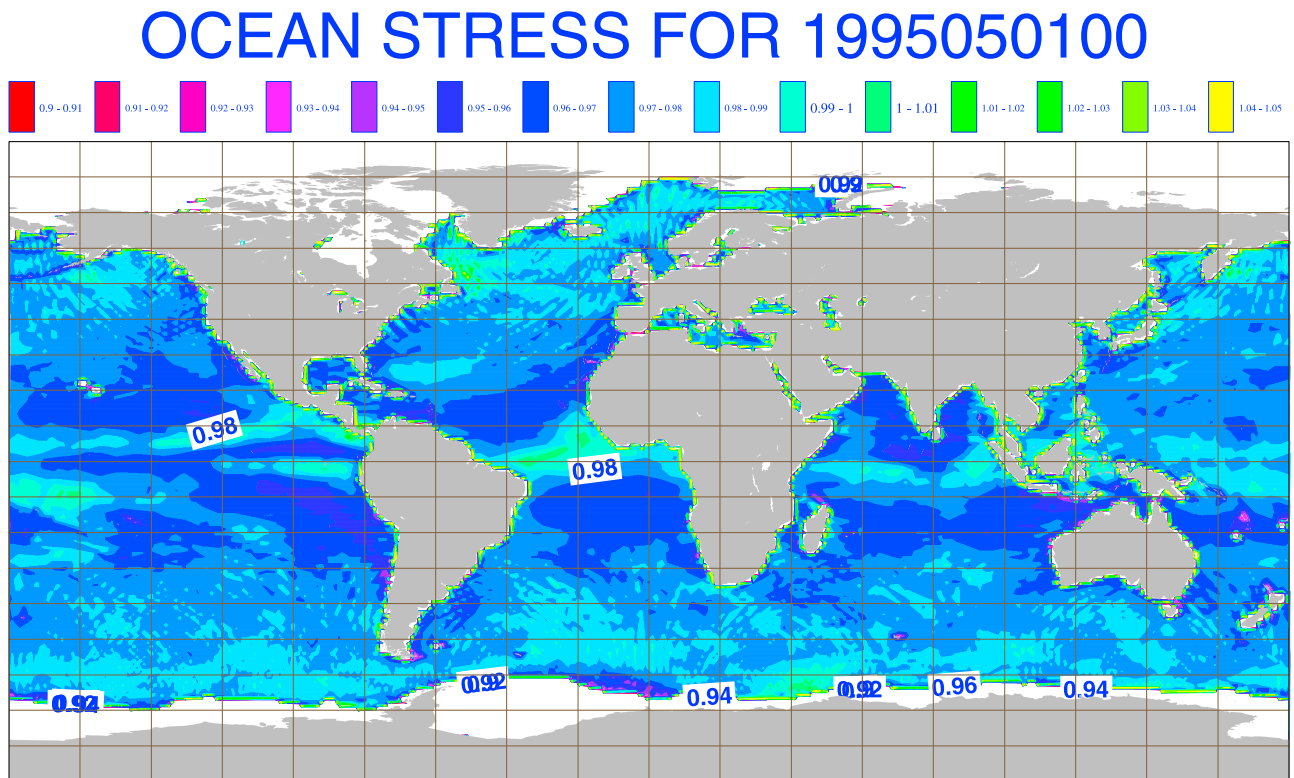

Figure 2. Monthly mean of momentum flux into the ocean, normalized with the monthly mean of the atmospheric stress. Period is May 1995.
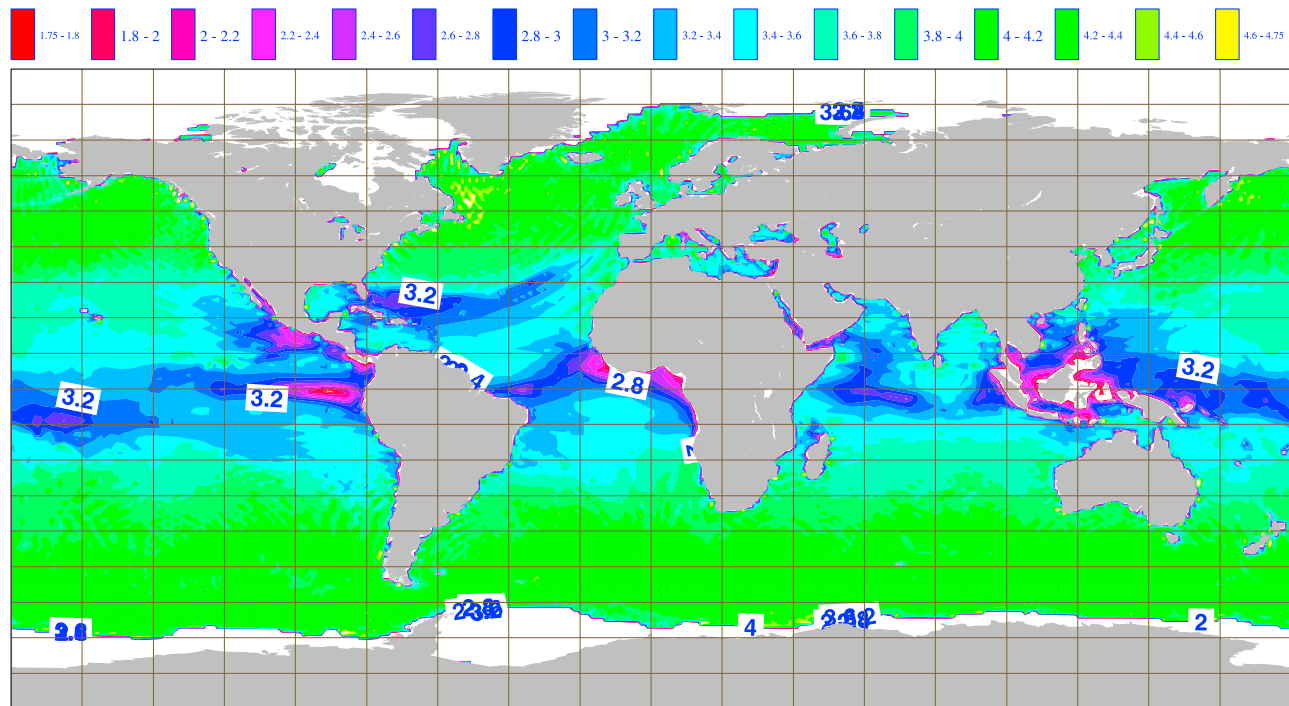
Figure 3. Monthly mean of energy flux into the ocean, normalized with the monthly mean of $\rho_a u_*^3$. Period is May 1995.

month of May 1995. The typical variation in the ratio τ_{oc}/τ_a is then found to be of the order of 4% while the variation in the normalized energy flux, $\Phi_{oc}/m\rho_a u_*^3$, is substantially larger. The global average of the value for m turns out to be $m \simeq 4.5$. Note that the map for the energy flux shows an interesting spatial pattern. In the equatorial region values of the normalized energy flux are small, suggesting that the mixed layer is thinner than the norm. In the extra-Tropics the normalized energy flux is considerably larger, presumably because here there is larger variability in the wind field.

[19] It is concluded that it is not a good idea to estimate the energy flux from the local stress, because significant memory effects are present in rapidly varying circumstances. In general, when wave information is available, it is preferred to directly use knowledge on the evolution of the sea state due to wave dissipation, cf. equation (8). Furthermore, on average 98% of the atmospheric stress is transferred locally to the ocean, while 2% of the wave momentum is advected away. However, under extreme circumstances such as during hurricanes as much as 10% of the wave momentum may be advected away. Therefore, although on average differences are small, it seems preferable to drive the ocean with the momentum flux from waves to ocean, cf. equation (7), because the alternative choice would introduce slightly more momentum in the ocean column, which in long integrations may give a contribution to climate drift.

[20] For completeness it is mentioned that ocean waves not only affect the momentum and energy flux across the air-sea interface, but the waves may also affect the heat flux in an indirect way. Using critical layer theory [*Janssen*, 1997]

determined the effect of ocean waves on the heat flux in the atmospheric boundary layer. Ignoring effects of breaking waves it was shown that while the contribution to the heat flux by the waves vanishes at the sea surface, the waves may nevertheless affect the temperature profile and hence may influence the heat transport by molecular processes. A more detailed discussion is given in section 3.2.

3. Mixed Layer Modeling

[21] After having found a method to obtain from the rate of change of the wave spectrum the momentum and energy flux into the ocean, we now turn our attention to the consequences for the mean flow in the ocean. We start from the work of *Craig and Banner* [1994] (and *Mellor and Yamada* [1982]) who introduced effects of wave dissipation on turbulent mixing by specifying the energy flux at the surface as a surface boundary condition to the turbulent kinetic energy (TKE) equation. Following *Grant and Belcher* [2009], the TKE equation is extended by introducing the generation of wave-induced turbulence and Langmuir circulation through work done against the shear in the Stokes drift. Furthermore, following *Noh and Kim* [1999] and *Baas et al.* [2008], the important effects of buoyancy are introduced as well. We discuss the consequences for the momentum and heat equation, where the eddy viscosity is expressed as a product of a mixing length, the turbulent velocity and a stability dependent function. Here, turbulent velocity follows from the solution of the turbulent kinetic energy budget.

[22] The model is applied to the problem of the diurnal cycle in sea surface temperature (SST), which is quite a

challenge because the SST follows from a balance between absorption of solar radiation in water and turbulent transport of heat. Assuming that the amplitude of the diurnal cycle can be measured accurately and since the absorption profile of solar radiation is fairly well-known, this application provides a sensitive test of our ideas of mixing in the upper ocean. In this section the model is presented, while in section 4 the properties of the steady state version of the momentum, heat and TKE equations are studied. This is then followed in section 5 by an application of the dynamical model to a synthetic case of constant wind forcing and heat flux, while, using observed forcings, the model is also applied to simulate the diurnal cycle in subsurface temperature for a one year period in the Arabian Sea.

3.1. Momentum Equation

[23] To simplify the problem, the wind/wave driven water velocity is assumed to be uniform in the horizontal without any pressure gradients. The mean water surface corresponds to $z = 0$. The bottom of the model is $z = -D$ where a constant depth D is assumed from the outset. Following *Janssen et al.* [2004] the horizontal momentum equations for a constant water density ρ_a are given by the general form

$$\frac{\partial \vec{u}}{\partial t} = \frac{1}{\rho_w} \frac{\partial}{\partial z} \tau + (\vec{u} + \vec{u}_{Stokes}) \times \vec{f}. \qquad (9)$$

where $\vec{f}$ is the coriolis parameter, $\vec{u}$ is the average ocean current, with the average defined in such a way that it filters out the linear wave motions, while $\vec{u}_{Stokes}$ is the Stokes drift. Details of the terms in the momentum equation are given below.

3.1.1. The Stress

[24] The stress in the water column is usually parameterized as $\vec{\tau}/\rho_w = \nu_m \partial \vec{u}/\partial z$ assuming that the main fluctuating component of the water velocity is turbulent. Here, ν_m is the eddy viscosity for momentum and following *Craig and Banner* [1994] the level-$2\frac{1}{2}$ Mellor-Yamada (1982) scheme is used. Hence, the eddy viscosity for momentum (and heat denoted by ν_h) is expressed as

$$\nu_{m,h} = l(z)q(z)S_{M,H} + \nu_w \qquad (10)$$

where ν_w is the water molecular viscosity, $l(z)$ is the turbulent mixing length, $e = q^2/2$ is the turbulent kinetic energy ($q(z)$ is called the turbulent velocity) and S_M and S_H are dimensionless parameters which may still depend on stratification. The turbulent velocity q will be obtained from the TKE equation, while the mixing length l is chosen as the usual one for neutrally stable flow, i.e.

$$l(z) = \kappa|z| \qquad (11)$$

with $\kappa = 0.4$ the von Kármán constant.

[25] However, in the same spirit as done for the problem of wind wave generation [*Janssen*, 1999; *Janssen et al.*, 2004] it is suggested that in the upper part of the ocean column wave motion provides an important contribution to the fluctuating velocity as well. Therefore, the fluctuating parts of the velocity are written as a sum of wave-induced motion, denoted with a subscript w, and turbulent motion, denoted with a prime ', and it is assumed that there is no correlation between wave motion and turbulence. As a result the stress $\vec{\tau}$ becomes

$$\frac{\vec{\tau}}{\rho_w} = -\langle \delta \vec{u}_w \delta w_w \rangle - \langle \vec{u}' w' \rangle,$$

and the turbulent part of the stress is modeled with the usual mixing length model while the wave-induced part is assumed to be completely determined by a number of sea state parameters. Note that on the air side it is possible [e.g., cf. *Janssen*, 1991] to obtain an analytical expression for the wave-induced stress. On the water side an explicit form of the wave breaking stress is not known, and at this stage the assumed functional form is more like an educated guess. The shape of the wave-induced stress is prescribed by a function that has a maximum at the surface (in agreement with the property that waves can transport momentum across the air-sea interface) and whose first derivative vanishes at the surface, hence

$$-\langle \delta \vec{u}_w \delta w_w \rangle = \frac{\vec{\tau}_{oc}}{\rho_w} \times \hat{T}(z), \quad 1 - \hat{T}(z) = \left(1 - e^{-|z|/z_{0M}}\right)^2, \quad (12)$$

where z_{0M} determines the gradient of the wave-induced stress and is assumed to be closely related to the significant wave height H_S. Note that when the momentum equation is integrated over depth the assumption of the vanishing of the first derivative avoids the occurrence of a singularity in the current at the surface. Therefore, it is assumed that wave dissipation affects at most a layer of thickness of the wave height.

[26] Combining everything together and introducing the water friction velocity w_* according to

$$w_*^2 = |\vec{\tau}_{diss}|/\rho_w \qquad (13)$$

the momentum equation becomes

$$\frac{\partial \vec{u}}{\partial t} = \frac{\partial}{\partial z}\left(\nu_m \frac{\partial \vec{u}}{\partial z}\right) + |\vec{w}|_* \vec{w}_* \frac{d\hat{T}(z)}{dz} + (\vec{u} + \vec{u}_{Stokes}) \times \vec{f}, \quad (14)$$

where the friction velocity vector $\vec{w}_*$ is assumed to have the same direction as the wind. The decomposition of the stress in terms of a turbulent stress and a wave-induced stress has also consequences for the boundary condition at the surface. The boundary condition for the turbulent stress at the surface becomes

$$z = 0: \rho_w \nu_m \frac{\partial \vec{u}}{\partial z} = \vec{\tau}_a - \vec{\tau}_{in}, \qquad (15)$$

because an amount $\vec{\tau}_{in}$ is spent in the generation of ocean waves. Therefore, the ocean is forced by the sum of the turbulent stress $\vec{\tau}_a - \vec{\tau}_{in}$ and the dissipation stress $-\vec{\tau}_{diss}$. The turbulent part of the momentum is distributed according to a diffusion equation (which has essentially no typical length scale) while the wave-induced part is distributed over the column with the length scale z_{0M} which is of the order of the wave height. However, when also the momentum flux of the gravity-capillary waves is taken into account it turns out that under strongly forced conditions, i.e. large wind speed, to a good approximation the wave-induced stress equals $\vec{\tau}_a$ so that at the surface the turbulent stress is small.

Hence, for strong winds in a good approximation one may take as boundary condition $\nu_m \partial \vec{u}/\partial z \approx 0$, but in low wind speed conditions this is not a valid assumption because the wave-induced stress may become vanishingly small as there may be no wind waves at all.

3.1.2. Stokes-Coriolis Forcing and Surface Drift

[27] In the usual description of the ocean the momentum of the ocean waves is not taken into account, despite the fact that a considerable list of authors [e.g., *Hasselmann*, 1970; *Weber*, 1983; *Jenkins*, 1987; *Xu and Bowen*, 1994; *McWilliams and Restrepo*, 1999] have pointed out that in a rotating ocean surface waves exert a wave-induced stress on the Eulerian mean flow which is called the Stokes-Coriolis force. It is given by the fourth term on the right-hand side of equation (14), where $\vec{u}_{Stokes}$ is the Stokes drift profile. The Stokes drift profile, U_S, is given by

$$U_S = \frac{2}{g} \int_0^\infty d\omega \, \omega^3 F(\omega) e^{-2k|z|}, \, k = \omega^2/g. \qquad (16)$$

with $F(\omega)$ the angular frequency spectrum. The Stokes-Coriolis force follows in a straightforward manner from the evaluation of the wave-induced stresses in a rotating ocean [*Xu and Bowen*, 1994].

[28] Equation (14) is the basic evolution equation for the mean ocean current in a Eulerian context. However, also the ocean waves give a contribution to the mean momentum [*Phillips*, 1977] resulting in an additional highly localized surface drift $\vec{u}_{surf}$ [*Janssen et al.*, 2004].

[29] For a single wave with surface elevation $\eta = a \cos\theta$, $\theta = kx - \omega t$ the mean wave momentum $\vec{P}_w$ at height z is given by

$$\vec{P}_w = \rho \vec{u}_{surf} = \frac{1}{2}(\rho_a + \rho_w)\omega a^2 d(z, a), \qquad (17)$$

where for small amplitude a the function $d(z, a)$ is highly localized around $z = 0$,

$$d(z, a) = \frac{2}{\pi a}\sqrt{1 - \left(\frac{z}{a}\right)^2}. \qquad (18)$$

for $|z| < a$, otherwise $d(z, a)$ vanishes. Note that $d(z, a)$ is normalized to 1, ie. $\int dz \, d(z, a) = 1$, and in the limit $a \to 0$ the function $d(z, a)$ behaves like a δ-function and hence the surface drift becomes a surface jet.

[30] The result for the mean momentum of a single wave may be generalized to the case of many waves once the joint probability distribution function of amplitude and period of the waves is known. For linear wave trains the surface elevation η obeys a Gaussian distribution and the joint pdf of envelope a and period $\tau = 2\pi/\omega$ has been obtained by *Longuet-Higgins* [1983]. Following *Janssen and Bidlot* [2009] negative frequencies are allowed as well, however. The ensemble average wave momentum then becomes

$$\langle \vec{P}_w \rangle = \rho \langle \vec{u}_{surf} \rangle = \frac{1}{2\pi}(\rho_a + \rho_w)\sigma\langle\omega\rangle e^{-\frac{1}{2}(z/\sigma)^2}, \, \sigma = \frac{H_S}{4}, \quad (19)$$

with H_S the significant wave height and with $\langle\omega\rangle$ the mean frequency based on the first moment of the spectrum. Hence, for a spectrum of waves with random phase the profile of the

wave-induced momentum $\vec{P}_w$ is seen to be a Gaussian with width determined by the significant wave height.

[31] Therefore, the total momentum $\vec{P}_{tot}$ of the combined system of ocean waves and ocean circulation becomes

$$\vec{P}_{tot} = \langle \vec{P}_w \rangle + \rho_w \vec{u} \qquad (20)$$

and the total transport is given by

$$\vec{T}^{tot} = \int_{-\infty}^0 dz \, \vec{P}_{tot} \qquad (21)$$

Denoting the surface stress by $\vec{\tau}_{oc}$ and assuming that the turbulent stress vanishes for large depth, one then finds, upon using the momentum equation (9) in the steady state, that the total transport is given by the classical result for the Ekman layer

$$\vec{T}^{tot} = \frac{\vec{\tau}_{oc} \times \vec{f}}{f^2}, \qquad (22)$$

in other words transport by the Stokes-Coriolis forcing is exactly canceled by the transport caused by the surface drift. Nevertheless, as shown in Janssen et al. (2004), because effects of the surface drift are only confined to a layer of the thickness of the significant wave height, the Stokes-Coriolis force will give rise to considerable deviations from the classical Ekman spiral in the layers below the surface layer.

3.2. Heat Equation

[32] The heat equation describes the evolution of the temperature T due to radiative forcing and turbulent diffusion. With c_p the heat capacity of water at constant pressure, the temperature evolves according to

$$\frac{\partial T}{\partial t} = -\frac{1}{\rho_w c_p}\frac{\partial R}{\partial z} + \frac{\partial}{\partial z}\nu_h\frac{\partial T}{\partial z}, \qquad (23)$$

where ν_h is the eddy viscosity for heat, given by equation (10), while, assuming clear waters, the solar radiation profile $R(z)$ is parameterized following the work of *Soloviev* [1982], i.e.

$$R(z) = a_1 \exp(-|z|/z_1) + a_2 \exp(-|z|/z_2) + a_3 \exp(-|z|/z_3) \qquad (24)$$

with $(a_1, a_2, a_3) = (0.28, 0.27, 0.45)$ while $(z_1, z_2, z_3) = (0.014, 0.357, 14.3)$. The decay length scale z_1, corresponding to the absorption of light in the infra red range, is seen to be quite small, of the order of 1 cm. Therefore, in order to capture the absorption of light in the infra red range high resolution in z near the ocean surface is required.

[33] The heat transport in the present model is entirely determined by turbulent transport. However, it is expected that also breaking waves will contribute to this process, just as waves contribute to momentum transport. Thus far this has not been done yet, mainly because there is relatively little known about the heat transport by breaking waves. In *Janssen* [1997] the effect of surface gravity waves on the heat flux in the atmospheric surface layer was determined. It was found that $q_w = -\langle\delta w \delta T\rangle = D_w \, \partial T/\partial z$ where D_w is proportional to the wave spectrum evaluated at the critical

height and is identical to the diffusion coefficient occurring in the transport of momentum by unsteady gravity waves [*Janssen*, 1982]. In this critical layer approach there is a direct correspondence between wave number space and ordinary space through the equation of the critical height z_c which reads $U_0(z_c) = c$ where $U(z)$ is the wind profile and c is the phase speed of the waves. As a consequence, the mean surface at $z = 0$ corresponds to high frequency gravity waves with zero phase speed, and since the wave spectrum vanishes for high frequencies, the wave diffusion coefficient D_w vanishes at the surface. In other words, according to the critical layer approach waves cannot transfer heat across the air-sea interface and this would suggest the following boundary condition for the turbulent heat flux $\nu_h \partial T/\partial z$ at the surface on the ocean side,

$$\nu_h \frac{\partial}{\partial z} T = \frac{Q_h}{\rho_w c_p} \qquad (25)$$

where Q_h is sum of latent and sensible heat flux. Note the difference with the boundary condition for the momentum flux given in equation (15) which shows that waves may transfer a considerable amount of momentum across the air-sea interface and, as a consequence, there is only a relatively small amount of momentum flux supplied to the turbulent momentum flux in the ocean. The momentum transfer by waves across the air-sea interface is caused by the work done by the wave-induced pressure at the mean sea level. Nevertheless, one would expect that in case of breaking waves considerable amounts of heat may be transferred across the air-sea interface which means that the boundary condition (25) requires modification, but at present there is no guidance to what the actual contribution to breaking waves is. Furthermore, it is unlikely that the heat flux profile may be represented by a simple exponential function which has its maximum at the surface. It is perhaps more likely that the flux profile should vanish at the interface.

[34] Because of all these uncertainties direct wave effects on the heat flux will be ignored, and the heat equation (23) will be solved subject to the boundary condition (25).

3.3. Kinetic Energy Equation

[35] The equation for the kinetic energy of the turbulent velocity fluctuations is obtained from the Navier-Stokes equations. If effects of advection are ignored, the TKE equation describes the rate of change of turbulent kinetic energy e due to processes such as shear production (including the shear in the Stokes drift), damping by buoyancy, vertical transport of pressure and TKE, and turbulent dissipation ε. It reads

$$\frac{\partial e}{\partial t} = \nu_m S^2 + \nu_m \vec{S} \cdot \frac{\partial \vec{u}_S}{\partial z} - \nu_h N^2 - \frac{1}{\rho_w} \frac{\partial}{\partial z} \left(\overline{\delta p \delta w} \right) - \frac{\partial}{\partial z} \left(\overline{e \delta w} \right) - \varepsilon, \qquad (26)$$

where $e = q^2/2$, with q the turbulent velocity, $\vec{S} = \partial \vec{u}/\partial z$, where $S = |\vec{S}|$, and $N^2 = -g\rho_0^{-1} \partial\rho/\partial z$, with N the Brunt-Väisälä frequency, ρ_w is the water density, δp and δw are the pressure and vertical velocity fluctuations and the over-bar denotes an average taken over a time scale that removes linear turbulent fluctuations.

[36] The turbulent production by Langmuir circulation and/or the orbital motion of the surface gravity waves is modeled following *Grant and Belcher* [2009] by the second term on the right-hand side of equation (26) which represents work against the shear in the Stokes drift. Here, $\vec{u}_S$ is the Stokes drift vector which has magnitude U_S; the expression for a general wave spectrum $F(\omega)$ is given in equation (16). Although in principle the depth dependence of the Stokes drift is therefore known it still is computationally expensive so we will use the approximate expression

$$U_S = U_S(0)e^{-2k_S|z|},$$

where $U_S(0)$ is the value of the Stokes drift at the surface and k_S is an appropriately chosen wave number scale.

[37] The dissipation term is from the Mellor-Yamada scheme, it is proportional to the cube of the turbulent velocity divided by the mixing length

$$\varepsilon = \frac{q^3}{Bl}, \qquad (27)$$

Here, B is another dimensionless constant.

[38] It is customary [see, e.g., *Mellor and Yamada*, 1982] to model the combined effects of the pressure term and the vertical transport of TKE by means of a diffusion term. However, the pressure term can also be determined by explicitly modeling the energy transport caused by wave dissipation. *Janssen* [1999] demonstrated how the pressure term may affect flow in the atmospheric boundary layer by using knowledge on the growth of waves by wind. The same idea will be used here [cf. *Janssen et al.*, 2004] but now applied to wave dissipation in the ocean column. Let us denote the correlation between pressure and vertical velocity perturbations by

$$I_w(z) = \frac{1}{\rho_w} \overline{\delta p \delta w} \qquad (28)$$

It is now claimed that at the surface the correlation $I_w(z)$ is just the work done by white capping/wave breaking on the ocean surface. Therefore, the pressure velocity correlation can be related to the energy flux from ocean waves to ocean circulation due to wave dissipation defined in equation (6), or,

$$I_w(0) = g \int_0^\infty S_{diss}(\vec{k})d\vec{k} = \frac{\Phi_{diss}}{\rho_w}, \qquad (29)$$

and the main problem is now how to model the depth dependence of $I_w(z)$. One could perhaps argue that the depth dependence may be modeled in a similar way as done for the Stokes drift (i.e. assume potential flow with the usual exp $(-2k|z|)$ factor inside the integral), but I would expect that the main action of wave dissipation is in a layer of thickness of order of the wave height H_S. Nevertheless, it is emphasized that there are still a number of open questions regarding the nature of surface wave dissipation. The suggested causes of the wave dissipation range from large scale wave breaking to microscale breaking or even by ocean eddies generated by unsteady large scale waves. Each different process will have a different penetration depth and for simplicity it is assumed here that these length scales can all be

lumped together to one wave height scale. Therefore the following depth dependence for $I(z)$ is suggested:

$$I_w(z) = I_w(0) \times \hat{I}_w(z), \hat{I}_w(z) = e^{-|z|/z_0}, \qquad (30)$$

where the depth scale $z_0 \sim H_S$ will play the role of a roughness length, and the surface value of I_w follows from equation (29). In the absence of the relevant information on the sea state, the energy flux is often parameterized as $\Phi_{oc} = m\rho_a u_*^3$, where m is in the range of 2–10 (cf. Figure 3). The energy flux may also be expressed in terms of the water friction velocity which gives $\Phi_{oc} = \alpha\rho_w w_*^3$ with $\alpha = m(\rho_w/\rho_a)^{1/2}$ having values of the order of 50–150. Using a wave prediction system, as intended here, m and α can be determined explicitly. Realizing that by definition I_w is negative one may therefore write

$$I_w(0) = -\alpha w_*^3. \qquad (31)$$

Using equations (30) and (31) in (26) and parameterizing the transport of turbulent kinetic energy by means of turbulent diffusion the TKE equation becomes

$$\frac{\partial e}{\partial t} = \frac{\partial}{\partial z}\left(lqS_q \frac{\partial e}{\partial z}\right) + \alpha w_*^3 \frac{\partial \hat{I}_w(z)}{\partial z} + \nu_m S^2 + \nu_m \vec{S} \cdot \frac{\partial \vec{u}_S}{\partial z}$$
$$- \nu_h N^2 - \frac{q^3}{Bl(z)}. \qquad (32)$$

At the surface there is no direct conversion of mechanical energy to turbulent energy and therefore the flux of turbulent energy is assumed to vanish. Hence the boundary conditions become

$$lqS_q \frac{\partial e}{\partial z} = 0 \qquad \text{for} \qquad z = 0, \qquad (33)$$

$$\frac{\partial e}{\partial z} = 0 \qquad \text{for} \qquad z = -D. \qquad (34)$$

The values used for the empirical constants are from the Mellor-Yamada model. For neutrally stable flow they are

$$\left(S_M, S_q, B\right) = (0.39, 0.2, 16.6) \qquad (35)$$

Note that in order to agree with the turbulence results for neutral flow, when there is a balance between production and dissipation of kinetic energy, the parameters S_M and B should satisfy the relation $B^{1/4}S_M^{3/4} = 1$.

3.3.1. Buoyancy Effects

[39] The description of the TKE equation is concluded by means of a discussion of buoyancy effects and the choice of the mixing length. In the upper ocean effects of stratification are important. In this paper the present mixed layer model will be applied to the prediction of the diurnal cycle in SST. Extreme events typically arise for low winds. At sunrise the upper ocean is usually neutrally stably stratified and the temperature profile is almost uniform. When the sun starts shining the top layer of the ocean gets heated up resulting in stable conditions which reduce the heat transport to the layers below. As a consequence a considerable amount of heat is retained in the top layer which may have a thickness

of a few decimeters only. In the course of the day more and more heat is added to this top layer with the consequence that the layer becomes more and more stable, reducing heat transport to the layers below even more. In the extreme circumstances of low winds of 1 m/s the Obukhov length may go down to a few centimeters, which is much smaller then what is encountered in the atmospheric case. An adequate modeling of these extremely stable cases is clearly of the utmost importance, but there is little empirical evidence available. Notable exceptions in the atmospheric context are the works of *Cheng and Brutsaert* [2005] and of *Grachev et al.* [2007a].

[40] In the presence of stable stratification it may be argued that buoyancy gives rise to a reduction of momentum and heat transport, because when the gradient Richardson number would pass 1/4 then fluid motion will be damped. Following *Csanady* [1964], *Deardorff* [1980], *Britter et al.* [1983] and *Wyngaard* [1985], this means that there is an additional parameter which may determine the transport properties of the upper ocean, namely the Brunt-Väisälä frequency N. Under very stable conditions one would expect that most of the 'turbulent' energy is concentrated near N which suggests that the mixing length is limited by an additional length scale $l_b = q/N$. The eddy viscosity can then be estimated by

$$\nu \sim ql_b \sim qlRi_t^{-1/2} \qquad (36)$$

where

$$Ri_t = (Nl/q)^2 \qquad (37)$$

is the Richardson number for turbulent eddies and the mixing length l is given in (11). On the basis of equation (36), which is valid at large Ri_t, it is suggested, that the dimensionless parameters $S_{M,H}$ can be represented by

$$S_{M,H}/S_0 = f_{M,H}(Ri_t); f_{M,H} = a_{M,H}\left(1 + b_{M,H}Ri_t\right)^{-1/2} + c_{M,H} \qquad (38)$$

with $a_{M,H}$, $b_{M,H}$ and $c_{M,H}$ empirical constants [see *Noh and Kim*, 1999; *Baas et al.*, 2008]. In fact, *Noh and Kim* [1999] have chosen zero values of $c_{M,H}$, but a number of studies have suggested that at least S_M should have a finite value in order to represent effects of internal waves on momentum transport [*Pacanowski and Philander*, 1981; *Strang and Fernando*, 2001; *Sukoriansky et al.*, 2005]. Finite c_M has important consequences for the turbulent transport properties: while for zero c_M there is a critical value of the gradient Richardson number above which there is no transport, in case of finite values of c_M a critical Richardson number does not exist in agreement with the notion that also internal waves may give rise to momentum transport.

[41] The relevant constants in equation (30) are chosen as follows: $a_M = 0.8$, $b_M = 100$, $c_M = 0.2$, $a_H = 1.4$ and $b_H = 80$, while c_H vanishes. The motivation for this choice is given in section 4.1 where basically the TKE equation is applied to the case of turbulent airflow in the atmospheric surface layer over a flat surface. This case is governed by Monin-Obukhov similarity as only shear production, buoyancy production and dissipation are assumed to be present. The

parameterizations from the Kansas field campaign [*Businger et al.*, 1971], valid for weakly stable stratification, and the renormalization results of *Sukoriansky et al.* [2005], also valid for strong stratification, were used to determine the relevant constants.

[42] Also the diffusion of turbulent kinetic energy is expected to be affected by effects of stratification as the size of the eddies is limited under strongly stable circumstances. And the same applies to the coefficient B in the dissipation. As a consequence

$$S_q/S_{q0} = B/B_0 = f_M(Ri_t)$$

thus under stable conditions the TKE transport enjoys the same reduction as the momentum transport. The coefficients S_0, S_{q0} and B_0 assume the values as given in equation (35).

[43] Finally, the case of unstable stratification ($Ri_t < 0$) needs to be modeled properly as well. It is assumed that also in this case the relevant parameters depend on the turbulent Richardson number Ri_t but the functional dependence is different. In this paper the following form is chosen for $f_{M,H}$ if $Ri_t < 0$:

$$f_{M,H} = (a_{M,H} + c_{M,H})\left(1 + \frac{d_{M,H}Ri_t}{1 + d_{M,H}Ri_t}\right),$$

where $d_{M,H} = -20$ and $f_{M,H}$ is continuous at $Ri_t = 0$ while for $Ri_t \to -\infty$ the dimensionless parameter $f_{M,H}$ is twice as large as its value at the origin. Although not shown explicitly here, this choice results in good agreement with the parameterizations of dimensionless shear function and virtual potential temperature gradient obtained from the Kansas field campaign [*Businger et al.*, 1971]. Experience from simulations of the diurnal cycle suggests that the evolution of sea surface temperature and surface current is fairly insensitive to details of how transport in unstable circumstances is represented.

4. Some Properties of the TKE Equation

[44] In section 3 the mixed layer model has been described and it is straightforward to solve these equations numerically [see, e.g., *Kondo et al.*, 1979; *Mellor and Yamada*, 1982; *Noh and Kim*, 1999]. The numerical approach will be further discussed in section 5. Here, instead, some interesting properties of the TKE equation will be discussed, in particular regarding effects of ocean waves on turbulent transport and effects of buoyancy. The discussion will be restricted to the steady state case. Furthermore, diffusion of TKE will be ignored, although turbulent diffusion is important in transporting TKE from the near surface to deeper parts of the ocean. This aspect and a number of mathematical details related to section 4 may be found in *Janssen* [2010]. Therefore, TKE will only depend on the local properties of the turbulent flow and hence this approach will be called the *local* approximation. Note that this approach is not feasible in the original Craig-Banner problem because diffusion is essential in order to transport the turbulent kinetic energy through the surface layer. However, here a different route has been followed as the pressure vertical velocity correlation term in the TKE equation has been explicitly modeled in terms of the energy flux and the profile function $\hat{I}_w$.

[45] Consider the one-dimensional version of the TKE equation and assume steady state. For simplicity, in this section the turbulent stress will be ignored. Eliminate the shear S and the buoyancy frequency N using the equations for momentum (14) and heat (23). From (14) one obtains for the shear

$$\nu_m S = w_*^2\left(1 - \hat{T}\right)$$

Similarly, integrating (23) once with respect to depth z and prescribing the heat flux Q_h at the surface one finds

$$\nu_h \frac{\partial T}{\partial z} = \frac{Q_h + R(0) - R(z)}{\rho_w c_p}$$

In order to eliminate the buoyancy frequency $N^2 = -g\rho'/\rho$ it is assumed that the water density is a function of temperature only, hence $\rho = \rho(T)$ and therefore the vertical gradient in density can be connected to the temperature gradient through the thermal expansion coefficient α_w, i.e.

$$\frac{1}{\rho}\frac{\partial \rho}{\partial z} = -\alpha_w \frac{\partial T}{\partial z}.$$

Next, one introduces the dimensionless turbulent velocity Q,

$$q = w_*\left(\frac{B}{S_M}\right)^{1/4} Q. \tag{39}$$

Furthermore, introduce a new length scale x according to,

$$dx = \frac{dz}{l} \tag{40}$$

where it is noted that the range of the new variable x is from $-\infty$ to ∞ because the turbulent mixing length $l(z) = \kappa|z|$ vanishes at the surface. Neglecting diffusion the steady state version of the TKE equation (32) then assumes the simple form

$$Q^3 - \frac{\left(1 - \hat{T}\right)^2}{Q} + f_M \zeta = S(x), \tag{41}$$

where the source function reads

$$S(x) = \alpha f_M \frac{d\hat{I}_w}{dx} + f_M La^{-2}\left(1 - \hat{T}\right)\frac{d\hat{U}_s}{dx}. \tag{42}$$

with $La = (w_*/U_S(0))^{1/2}$ the turbulent Langmuir number and f_M the stability dependent function introduced in (38). Here, the left-hand side of the dimensionless form of the TKE equation contains the processes which are usually encountered in the atmospheric surface layer, namely dissipation, turbulence production by shear and buoyancy. The stability parameter ζ is defined as $\zeta = |z|/L$ where L is the Obukhov length scale

$$L = -\frac{\rho w_*^3}{\kappa g \nu_h d\rho/dz}. \tag{43}$$

which is the height where shear production and buoyancy balance. Making use of the temperature profile and the

relation between density gradient and temperature gradient, the Obukhov length becomes

$$L = \frac{\rho_w c_p w_*^3}{\kappa g \alpha_w (Q_h + R(0) - R(z))}. \qquad (44)$$

and, because of the local definition of the Obukhov length, radiative forcing is included in a natural way in the expression for L [cf. *Large et al.*, 1994]. The right-hand side of (41) gives the effects of ocean waves on the mixing in the upper ocean: the first term represents effects of wave dissipation which affect mixing close to the ocean surface, while the second term (which depends on the turbulent Langmuir number) represents the effect of Langmuir circulation which transports heat and momentum to the deeper parts of the ocean.

[46] It is, as far as I know, not possible to obtain for the general case the exact solution of the algebraic problem (41), (42). The reason for this is that the stability function f_M, which is a function of the turbulent Richardson number Ri_t, depends in a complicated way on the turbulent velocity Q and the stability parameter ζ. Therefore, the general case can only be solved using an iteration scheme, but it is possible to solve the neutral stable case with $Ri_t = 0$. In that event $f_M = 1$ while $\zeta = 0$ and equation (41) reduces to a quartic equation in Q. This still gives an awkward expression for the turbulent velocity Q. A much simpler solution is possible following a suggestion by Ø. Saetra (private communication, 2002). In fact, this approach was also followed by *Craig* [1996] although it is not mentioned explicitly in his paper. Inspecting the algebraic equation for Q it is realized that the nonlinearity only comes from the Q^{-1} term and therefore the nonlinearity is fairly weak. It is therefore suggested to replace the Q^{-1} term by its equilibrium value for large x. Far away from the sea surface the wave dissipation and Langmuir circulation term $S(x)$ vanish. The equilibrium value for Q then follows from the balance of shear production and dissipation (which is the 'typical' situation in the atmospheric surface layer), hence $Q = (1 - \hat{T})^{1/2}$. Therefore, the algebraic equation for Q becomes approximately

$$Q^3 \approx (1 - \hat{T})^{3/2} + \alpha \frac{d\hat{I}_w}{dx} + La^{-2}(1 - \hat{T})\frac{d\hat{U}_s}{dx}. \qquad (45)$$

The approximate solution (45) was compared with the exact solution obtained from the quartic problem and, in practice, a good agreement was found.

[47] Knowing the turbulent velocity Q, the current profile follows now immediately from the one-dimensional, steady-state version of the momentum equation (14), which is integrated with respect to depth while using the boundary condition (15). In terms of the present dimensionless variables one then finds

$$u(z)/w_* = \int_{x_D}^x \frac{dx}{Q}(1 - \hat{T}), \qquad (46)$$

where $x = x_D$ corresponds to the depth D where the current profile vanishes. In this section $D = 5H_S$ is chosen.

[48] It is now straightforward to estimate the respective contributions of wave dissipation and Langmuir turbulence to the dimensionless turbulent velocity Q. This is compared with Monin-Obukhov similarity which is based on the balance between shear production and dissipation of turbulence. The estimate is obtained by taking the maximum of the individual terms. The maximum of the shear production term is 1, while the maximum of the wave dissipation contribution is, with $\alpha = 100$, $\alpha \kappa e^{-1} \approx 15$ at $z = -z_0$ and the maximum contribution by Langmuir turbulence is $La^{-2}\kappa e^{-1} \approx 2$ at $z = -1/2k_s$ for $La = 0.25$. Based on these estimates it seems that near the surface the most relevant process for mixing is wave dissipation because it is an order of magnitude larger than the other two terms, however the turbulent velocity is only enhanced by a factor 2.5 because the sum of the contributions is raised to the power 1/3. Nevertheless, Langmuir turbulence should be relevant as well as this process penetrates into the deeper layers of the ocean.

[49] The relative importance of shear production, wave dissipation and Langmuir turbulence as function of dimensionless depth $|z|/H_S$ is illustrated in Figure 4 for a special case of low wind. This low wind speed example has been chosen because under these circumstances a diurnal cycle in the sea surface temperature and in the surface drift might be present.

[50] In order to be able to plot the solution (45) the decay length scales z_M and z_0 of the wave-induced stress and the pressure-vertical velocity correlation need to be specified. These length scales will be specified in terms of the significant wave height H_S, defined as $H_S = 4m_0^{1/2}$, with m_0 the zeroth moment of the wave spectrum. Since the wave-induced stress is more sensitive to the short wave part of the spectrum it is expected that the momentum flux penetrates less deep into the ocean than the energy flux. Hence, the decay length scale for the wave-induced stress will be chosen shorter than the corresponding one for the energy flux. Here the choice

$$z_{0M} = H_S/8 \quad z_0 = H_S/2, \qquad (47)$$

is made, and in section 4.2 arguments are presented why the choice of the length scale for the energy flux seems appropriate. The wind speed is 2.5 m/s, the turbulent Langmuir number is 1/4 and the dimensionless energy flux α is equal to 100, which is a typical value in the Tropics (see Figure 3). In this example it is assumed that there is only wind sea present. The significant wave height follows from the empirical formula $H_S = \beta U_{10}^2/g$, with $\beta = 0.22$. The Stokes drift decay length scale then follows from $k_s = g/U_{10}^2$. For $U_{10} = 2.5$ m/s the significant wave height is only 14 cm so that the 'roughness' length is about 7 cm. The air friction velocity u_* is 8 cm/s while the water friction velocity w_* is about 0.3 cm/s. Finally, the Stokes wave number k_s is about 1.6 rad/m.

[51] Figure 4 shows the impact on the profile of Q^3 of switching off Langmuir turbulence and wave dissipation. Indeed the maximum in Q^3 by wave dissipation is close to the sea surface at a depth z_0 while the maximum by Langmuir turbulence is at the larger depth of $1/2k_s$. These scales are widely different because ocean waves are weakly non-linear which means that their 'typical' steepness $k_s H_S \ll 1$. As a consequence the ratio of the penetration depths by wave dissipation and Langmuir turbulence, given by $2k_s z_0 = k_s H_S$, is small as well.
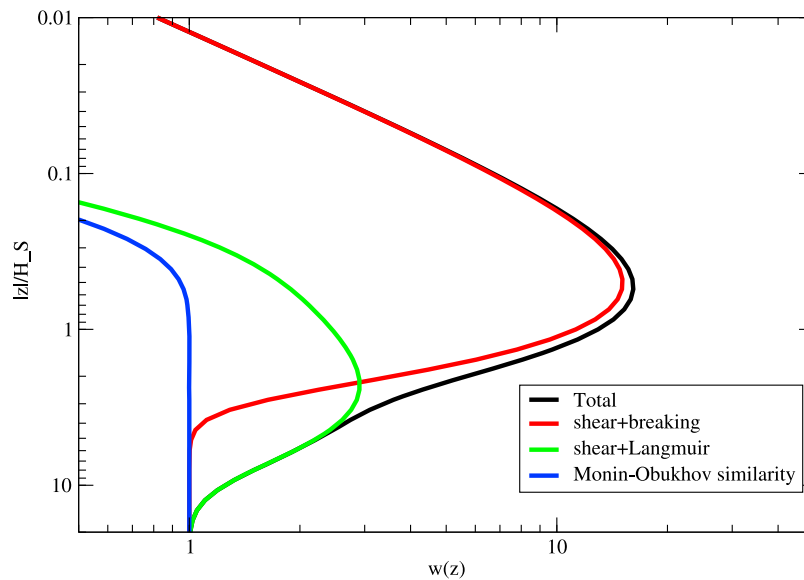
Figure 4. Profile of $w = Q^3$ according to the local approximation in the ocean column near the surface. The contributions by wave dissipation (red line) and Langmuir turbulence (green line) are shown as well. Finally, the w-profile according to Monin-Obukhov similarity, which is basically the balance between shear production and dissipation, is shown as the blue line.

[52] Therefore it is evident that there are two regimes. The first one is close to the surface and is dominated by wave dissipation. Around 4 times the roughness length a transition to a different regime is to be noted, namely one dominated by the production of Langmuir turbulence. Hence, it is seen that there are two transport mechanisms operating in the surface layer of the ocean. Up to a few wave heights wave dissipation is dominant in the diffusion of momentum and heat and the transport of these quantities is taken over by Langmuir turbulence in the deeper part of the surface layer. The enhanced transport by wave processes gives rise to much flatter profiles near the surface. This may be inferred

from Figure 5 where current profiles from the Monin-Obukhov similarity model are compared with current profiles when wave dissipation and Langmuir turbulence play a role. The surface current reduces from about $7w_*$ to $2.5w_*$, which is a considerable reduction. As a consequence, it is expected that upper ocean mixing by wave dissipation and Langmuir turbulence will play an important role in the determination of the amplitude of the diurnal cycle. Finally, it is also concluded that a mixed layer model which has only a representation of Langmuir turbulence will not provide sufficient mixing of heat and momentum, hence it will overestimate the amplitude of the diurnal cycle. If one is
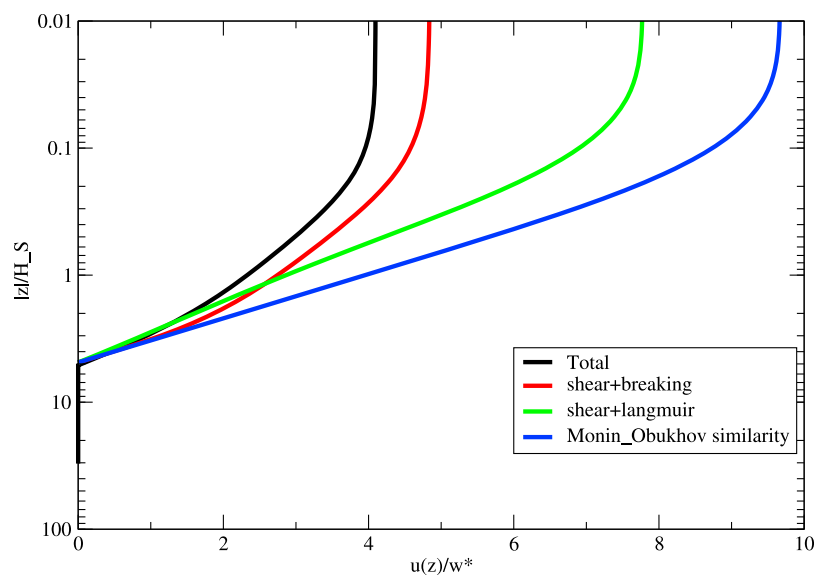

Figure 5. Current profile near the surface. The impact of wave dissipation and Langmuir turbulence is shown as well. The Monin-Obukhov similarity gives the usual logarithmic profile.

interested in modeling the diurnal cycle then probably only the first few meters of the upper ocean need to be considered. In that event wave dissipation is seen to be the dominant process for heat transport. Nevertheless there is no reason to disregard effects of Langmuir turbulence from the outset as it is very straightforward to take this effect into account. In addition, during the diurnal cycle there will also be episodes when the flow is neutrally stable or unstable. Langmuir turbulence will then play a pronounced role.

[53] This section is concluded with the following comment. So far we have learned that in the local approximation it seems possible to combine in a simple way several physical processes that affect the mixing in the upper-ocean. From the previous discussion it appears that if one has, apart from shear production S_P, several processes P_1, P_2, P_2, ... that contribute to turbulent mixing then the turbulent velocity $q(z)$ of the combination of all those processes is, following equation (45), given by

$$q = \left\{ S_P^{3/4} + P_1 + P_2 + P_3 + ... \right\}^{1/3}.$$

The reason that processes can be added via an '1/3'- rule is because dissipation is proportional to the third power of q, while the shear production term has been linearized by replacing q by its equilibrium value and the other processes are assumed to be independent of the turbulent velocity q. Because of the '1/3'- rule it makes sense, as done in the present work, to make plots involving Q^3 as this allows to add the different processes by eye.

[54] Nevertheless, it should be pointed out that the '1/3'-rule is not always appropriate. In particular, the buoyancy term has so far not been considered but this effect is expected to play an important role far away from the surface, thus making it difficult to give an estimate of the equilibrium value of q. In addition, the buoyancy term is a fairly sensitive function of q and therefore it is not easy to linearize it.

4.1. Effects of Stratification

[55] First, effects of stratification in the atmospheric context will be studied and the findings will be applied to the mixed layer of the upper ocean. In the atmosphere close to the surface there is a balance between shear production, buoyancy and dissipation, as forcing is usually absent. This will be called the case of Monin-Obukhov similarity.

4.1.1. Monin-Obukhov Similarity

[56] In the atmosphere, stability effects are usually studied in terms of the dimensionless shear function ϕ_m and the dimensionless virtual potential temperature gradient ϕ_h. These dimensionless functions are defined as

$$\phi_m = \frac{\kappa |z|}{u_*} \left| \frac{\partial u}{\partial z} \right|, \quad \phi_h = \frac{\kappa |z|}{\theta_*} \frac{\partial \theta_v}{\partial z}, \tag{48}$$

where u_* is the air friction velocity and $\theta_* = -\overline{w'\theta'_v}/u_*$ is a turbulent temperature scale. The dimensionless shear function measures deviations from neutral circumstances as for the logarithmic wind profile $\phi_m = 1$, and similarly ϕ_h measures deviations from the logarithmic virtual temperature profile. Using the local scaling theory of *Nieuwstadt* [1984] it can be argued that the profile functions are only a

function of the stability parameter $\zeta = z / L$, where L is the local Obukhov length defined as

$$L = -\frac{u_*^3 \theta_v}{\kappa g \Phi_h}. \tag{49}$$

Here, θ_v is the virtual potential temperature and $\Phi_h = -\overline{\delta w \delta \theta_v}$ is the virtual potential temperature flux.

[57] Let us now apply the TKE equation (41) to the atmospheric problem where forcing is absent. In the steady state one then finds

$$Q^4 + \zeta f_M Q - 1 = 0. \tag{50}$$

The similarity functions can be written in terms of the present dimensionless variables and the result is

$$\phi_m = \frac{1}{Q f_M}; \quad \phi_h = \frac{1}{Q f_H} \tag{51}$$

Expressing Q in terms of ϕ_m and substituting the result into (50) gives

$$\phi_m^4 - \zeta \phi_m^3 - f_M^{-4} = 0. \tag{52}$$

This equation is similar to the well-known KEYPS formula [*Panofsky*, 1963].

[58] The shape of the ϕ functions is usually determined from observations acquired during field campaigns, but high measurement accuracy is required because the fluxes become weak during strongly stable conditions. Alternatively, a realistic theoretical model of turbulent flows with stable stratification has been developed by *Sukoriansky et al.* [2005] providing additional information on how to model stratification effects. The Kansas field campaign [*Businger et al.*, 1971] was one of the first experiments to propose realistic parameterizations for the ϕ functions. But note that in order that $\phi_m(\zeta = 0) = 1$, a von Kármán constant of 0.35 was chosen, which does not agree with the accepted value of 0.4. For stable conditions it was found that ϕ_m and ϕ_h vary essentially linearly with ζ over the observed stability range between 0 and 1. A fit gives

$$\phi_m = 1 + 4.7\zeta, \quad \phi_h = 0.74 + 4.7\zeta, \text{ for } 0 < \zeta < 1. \tag{53}$$

On the other hand, for unstable conditions a good fit was found to be

$$\phi_m = (1 - 15\zeta)^{-1/4}, \quad -2 < \zeta < 0. \tag{54}$$

A similarly looking fit was found for ϕ_h. However, in the upper ocean strongly stable conditions occur with ζ of the order 10 or even larger. These conditions are much more extreme than typically encountered for the atmospheric surface layer except perhaps for air flow over ice. Therefore, relatively little is known in these extreme circumstances, and in fact conflicting conclusions about properties of strongly stable turbulence have been reached in the past. The problem is best illustrated by the behavior of the Prandtl number Pr, defined as

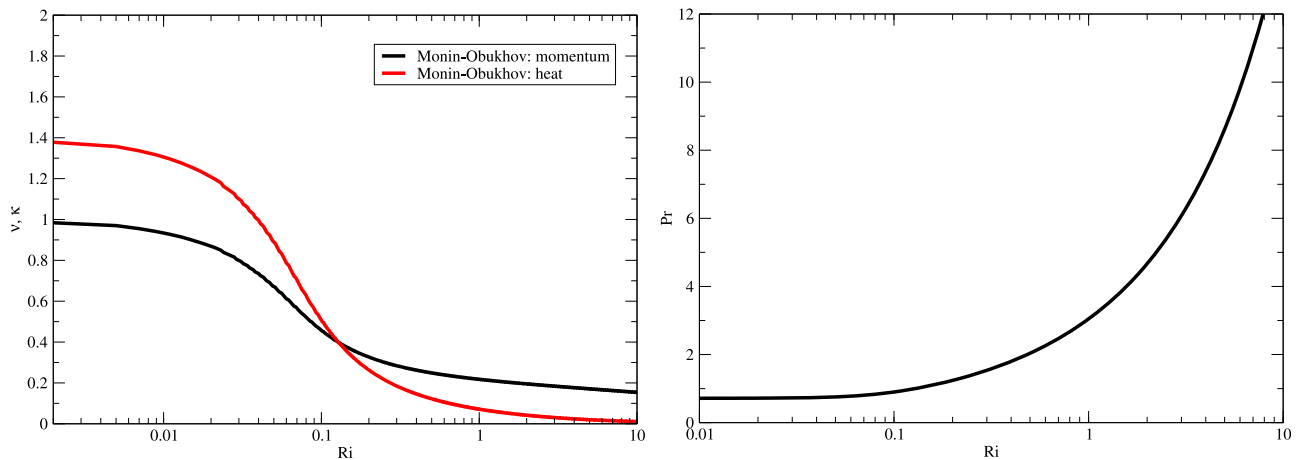$$Pr = \frac{\nu_m}{\nu_h} = \frac{\phi_h}{\phi_m},$$

Figure 6. (left) Eddy viscosity v_m and heat diffusivity v_h, normalized with the neutral value of the eddy viscosity, as function of the local Richardson number Ri. (right) The Prandtl number Pr shown as function of Ri.

as function of the gradient Richardson number Ri given by

$$Ri = \frac{N^2}{S^2}.$$

A vast number of studies [see, e.g., *Kondo et al.*, 1978; *Kim and Mahrt*, 1992; *Strang and Fernando*, 2001; *Monti et al.*, 2002; *Sukoriansky et al.*, 2005; *Zilitinkevich*, 2007] (and many others) suggest that for strongly stable flow, hence for a Richardson number larger than the critical value of 1/4, the Prandtl number is larger than 1, while for small Ri (the neutral limit) the Prandtl number is smaller than 1 (as is evident from equation (53)). In other words, for strongly stable flow, momentum is mixed more efficiently than heat. This is thought to be an indication of internal gravity wave activity which can produce transfer of momentum but only little heat transfer (as long as the waves do not break).

[59] In sharp contrast to these findings, *Cheng and Brutsaert* [2005] and *Grachev et al.* [2007b] conclude from the SHEBA observations, which were obtained for strongly stable flow over ice, that heat transport is more efficient than momentum transport hence $Pr < 1$. *Grachev et al.* [2007b] have analyzed their findings in some detail, but no physical explanation has been offered. Both *Cheng and Brutsaert* [2005] and *Grachev et al.* [2007a] find a leveling-off of the similarity functions ϕ_m and ϕ_h as a function of the stability parameter ζ which is so large that it conflicts with the steady state TKE equation. For example, the *Grachev et al.* [2007a] parametrization for ϕ_m will cross the line $\phi_m = \zeta$ for $\zeta \approx 17$ which is well inside the stability range that the dimensionless shear has been observed. However, when $\phi_m < \zeta$ the implication is that the buoyancy term from equation (52) becomes more important than the shear production term, but this is not possible because dissipation is always positive. Thus, the SHEBA results cannot be used as a guideline for the present modeling work.

[60] Therefore, the choice of the coefficients in the parametrization (38) of f_M and f_H will be based on the one hand on the Kansas field results in the weakly stable limit, while for the strongly stable limit guidance from the

renormalization work of *Sukoriansky et al.* [2005] is taken. In particular, the following choice for f_M and f_H has been made:

$$f_M = a_M(1 + b_M Ri_t)^{-1/2} + c_M, f_H = a_H(1 + b_H Ri_t)^{-1/2} \quad (55)$$

where $a_M = 0.8$, $b_M = 100$, $c_M = 0.2$, $a_H = 1.4$ and $b_H = 80$. From (55) it is seen that f_H vanishes for large Ri_t while f_M asymptotes to a finite value of $c_M = 0.2$. For small turbulent Richardson numbers f_H is larger than f_M, hence, with $Pr = \phi_h/\phi_m = f_M/f_H$, it is found that $Pr \approx 0.71 < 1$ for $Ri_t \to 0$ in agreement with results from the Kansas field campaign. In order to determine some of the coefficients an approximate solution of equation (52) was used. In fact, an approximate solution for the dimensionless turbulent velocity Q may be found for small values of the stability parameter ζ. One finds $Ri \approx \zeta/a_H$ and the eventual result for the dimensionless shear function is

$$\phi_m \approx 1 + \frac{1}{4}\zeta\big[1 + 2(1 - c_M)b_M S_0^2/a_H\big].$$

but this approximation is only valid for a relatively small range of the stability parameter, $\zeta < 0.1$. The choice of coefficients given below equation (55) together with $S_0 = .39$ gives a value of the slope of 4.6 which is close to the value reported by the Kansas field campaign given in equation (53). In addition, Figure 6 (right) shows that up to a gradient Richardson number of 0.1 the Prandtl number is a constant so that in agreement with the Kansas data ϕ_h has the same slope as ϕ_m for small ζ.

[61] On the other hand, for large turbulent Richardson number, $Ri > 0.2$, the Prandtl number is larger than 1, indicating that in this domain momentum transfer is more efficient than heat transport, in agreement with *Sukoriansky et al.* [2005] and the observations of *Strang and Fernando* [2001]. In order to show explicitly the effect of buoyancy on the transport properties, the eddy viscosity v_m and heat diffusivity v_h are normalized with the eddy viscosity $\nu = \kappa u_* |z|$ for neutrally stable flow. In terms of the present dimensionless variables one finds $v_m/\nu = f_M Q$ while $v_h/\nu = f_h Q$, hence the
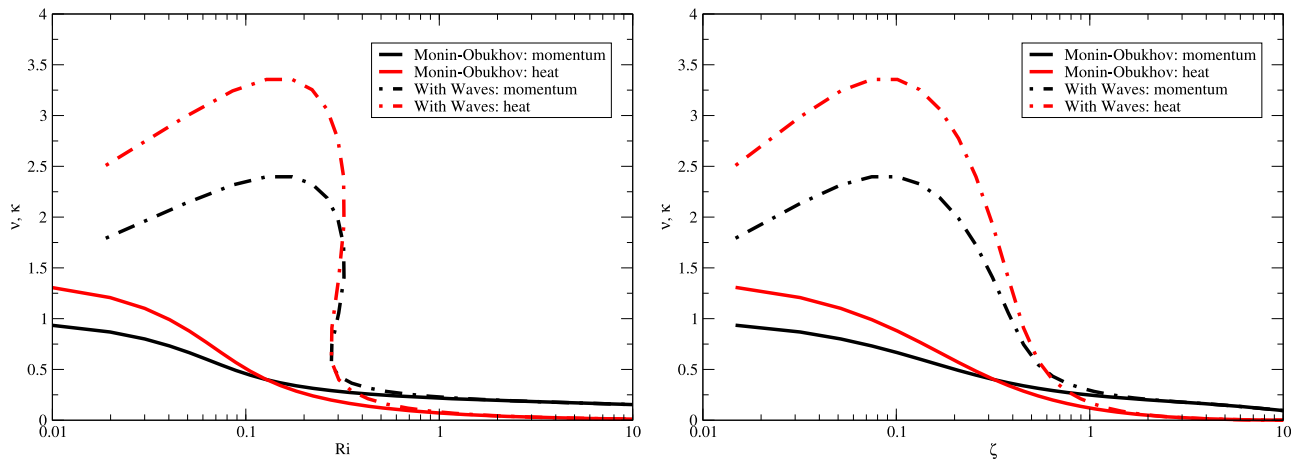
Figure 7. (left) Eddy viscosity v_m and heat diffusivity v_h, normalized with the neutral value of the eddy viscosity, as function of the local Richardson number Ri, showing the effects of wave dissipation and Langmuir turbulence. (right) The same parameters shown as function of the stability parameter ζ.

normalized viscosities are simply the inverse of ϕ_m and ϕ_h. Using (55) in (50) and solving for Q by iteration the resulting transport coefficients as function of the Richardson number $Ri = \zeta \phi_h / \phi_m^2$ are shown in Figure 6 (left), while the Prandtl number Pr as function of Ri is shown in Figure 6 (right). Comparing this figure with Figures 8 and 9 of *Sukoriansky et al.* [2005] it is seen that there is good qualitative agreement with the results using renormalization techniques to obtain the transport coefficients. In particular, as already pointed out, a finite value of c_M in (54) does not give rise to a critical value of the gradient Richardson number as a finite c_M represents additional diffusion by e.g. internal gravity waves and/or intermittency. At the same time, the consequence is that for large Richardson number momentum transport dominates heat transport.

4.1.2. Wave Effects and Buoyancy

[62] In this section the combined effects of wave dissipation, Langmuir turbulence and buoyancy on the properties

of turbulence in the mixed layer are studied. It is assumed that the parametrization of effects of stratification (cf. equation (55)) also holds for the oceanic case. The set of equations to be solved consists of (41) together with (37), (38), and (44). This set of equations does not have an exact solution because owing to effects of stability f_M in (41) depends strongly on the dimensionless turbulent velocity Q. The set of equations was therefore solved by means of an iteration scheme using starting values $Q = 1$, $f_M = f_H = 1$. Because the stability effects are modeled in terms of the turbulent Richardson number $Ri_t = (Nl(z)/q)^2$, the Brunt-Väisälä frequency needs to be expressed in terms of Q. Introducing $N_* = l(z)N/w_*$ one finds $N_*^2 = \zeta / f_H Q$.

[63] In Figure 7 effects of wave dissipation and Langmuir turbulence on transport coefficients for momentum and heat are shown. In Figure 7 (left) these coefficients are plotted as function of the gradient Richardson number Ri, while in Figure 7 (right) they are shown as function of the stability
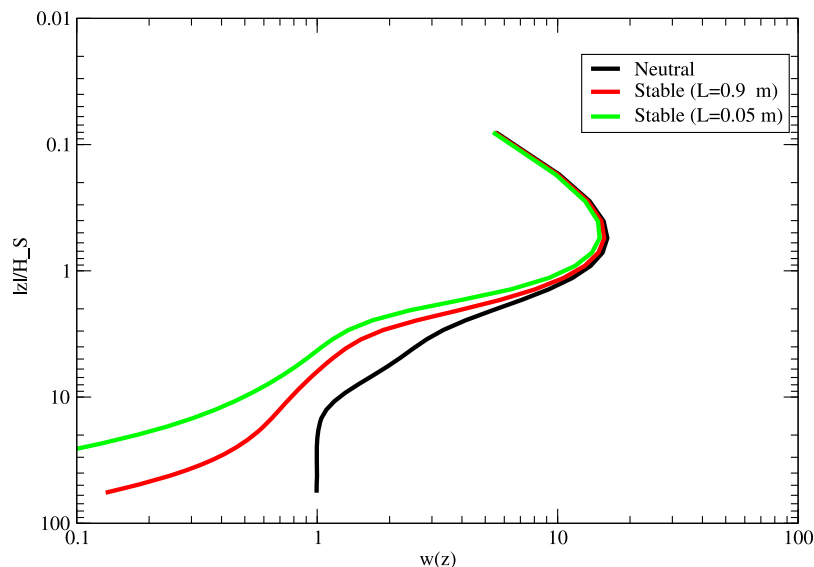

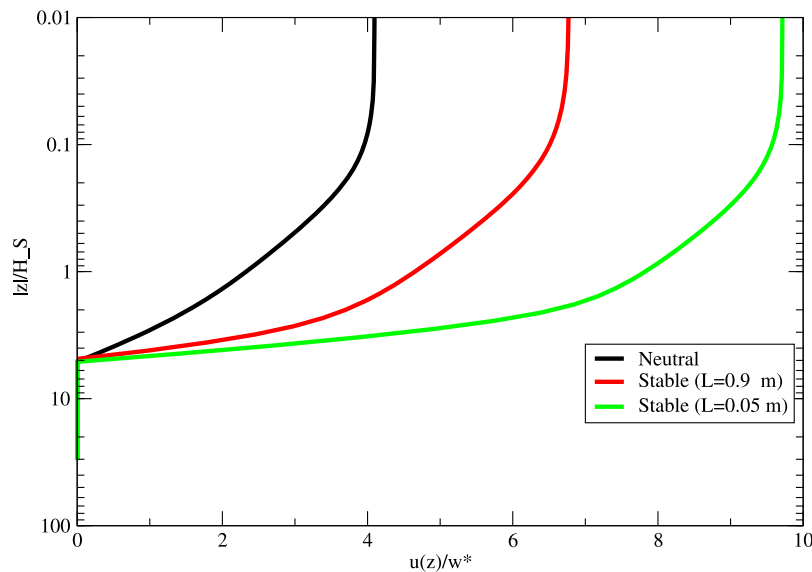**Figure 8.** Dependence of $w(z)$-profile on effects of buoyancy.

Figure 9. Dependence of near-surface current profile on effects of buoyancy.

parameter ζ. Of course, waves give rise to enhanced transport, but, remarkably, in the presence of this additional forcing the transport coefficients are not a single-valued function of Ri. However, in terms of the turbulent Richardson number Ri_t or the stability parameter ζ (as shown in Figure 7, right) the transport coefficients are unique functions.

[64] In Figure 8 effects of stratification on the profile for $w = Q^3$ as function of dimensionless depth $|z|/H_S$ are shown. For this plot the parameters from the example in section 4.1 are used and, in addition, the heat flux Q_h was 100 W/m^2 while the water temperature T was 303 K. In order to vary the Obukhov length scale L, as determined by equation (44), wind speed values of 2.5 and 1 m/s were used respectively. It is instructive to compare results for Q^3 (z) with the case of no stratification. It is then immediately seen that, as expected, buoyancy has the biggest impact on the turbulent velocity Q in the deeper layers of the ocean (note that $L = 0.9$ corresponds to $L \approx 5 H_S$). This means that according to this model the impact of Langmuir turbulence on upper ocean mixing is considerably reduced in stable circumstances. For these particular examples the maximum in Q, caused by wave dissipation, is hardly affected by stability effects. Surprisingly perhaps, this is a fairly general result. Only when the heat flux was increased by a factor of 10 an appreciable reduction of the impact of wave dissipation on the mixing was found (not shown). This apparent robustness of the wave dissipation impact on mixing can be understood by once more noting that the maximum of $Q(z)$ occurs at $z = -z_0$, where according to the present model the roughness length scales with the square of the wind velocity. A significant impact of buoyancy on the maximum is expected when $L \leq z_0$. Using the definitions for L and z_0 one finds that in practice this condition can only be met for very low wind speed conditions.

[65] Finally, in Figure 9 the impact of stability on the equilibrium current is shown. The increase of the surface current for increasing stability is mainly caused by the reduction of the effects of Langmuir turbulence. The figure

illustrates that also in the surface current a diurnal cycle is to be expected. As a general remark it is noted that under unsteady circumstances the impact of effects of stability, wave dissipation and Langmuir circulation is reduced, while the temperature and current profile may occasionally be convex rather then concave as in the steady state case. This will be shown in more detail in the next section during a discussion of the simulation of the diurnal cycle in SST.

4.1.3. A Qualitative Validation

[66] The present experimental knowledge of turbulence in the ocean surface layer is summarized by the works of *Terray et al.* [1996], *Drennan et al.* [1996] and *Anis and Moun* [1995]. Here, dimensionless dissipation, defined as $\varepsilon_* = \varepsilon H_S/\Phi_{in}$ with Φ_{in} the energy flux into the ocean, is found to be a function of dimensionless depth $(|z| + z_0)/H_S$. In the case of Monin-Obukhov similarity one would expect that the 'Law of the Wall' holds which states that dissipation scales with $|z|^{-1}$ as the turbulent velocity is constant. However, according to observations of turbulence near the surface, dissipation depends in a more sensitive manner on depth. Based on work of *Terray et al.* [1999] and of *Burchard* [2001], who summarized the observational knowledge, one finds near the surface the fit

$$\varepsilon_* = 0.78 Z^{-2.78}, \quad Z = (|z| + z_0)/H_S.$$

which is valid for $\varepsilon_* > 0.01$. These observations are quite useful to determine an important parameter in the mixed layer scheme, namely the roughness length z_0 or the corresponding gradient length scale of the wave dissipation source function. Burchard finds an optimal fit (however using a somewhat different turbulence model) when $z_0 = 0.5 H_S$. This finding has been confirmed here. In order to illustrate that the present model indeed gives the correct scaling behavior, Figure 10 shows dimensionless dissipation versus $(|z| + z_0)/H_S$ for the strongly stable case and for neutral stability and compares the model results with the above power law. In the validity region of the empirical fit, i.e.
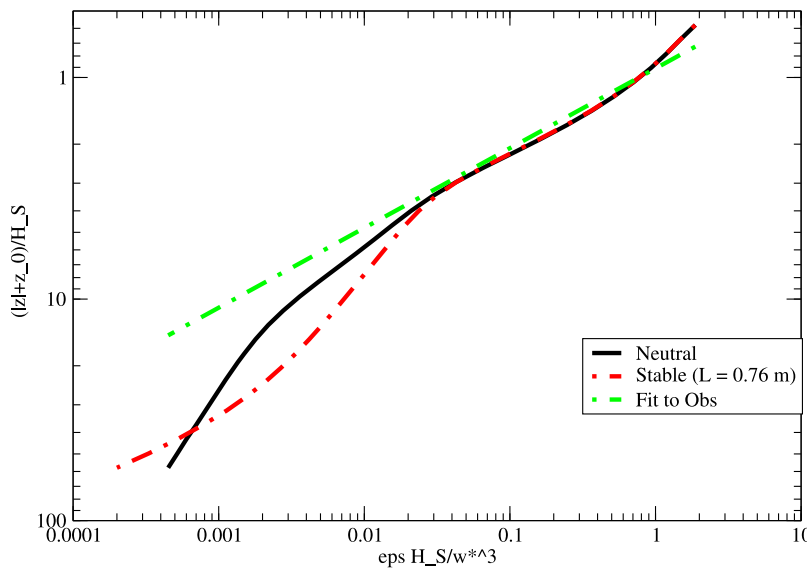
Figure 10. Dimensionless dissipation $\varepsilon_* = \varepsilon H_S/\Phi_{in}$ versus $(|z| + z_0)/H_S$.

$\varepsilon_* > 0.01$, the agreement between the neutrally stable case and the fit to the data seems fair. Also note that according to the present mixed-layer model there is a transition from wave dissipation driven turbulence to shear driven turbulence, giving the 'Law of the Wall' in the deeper layers of the ocean, while in the transition layer turbulence is controlled by production of Langmuir circulation. Furthermore, although this cannot be shown explicitly because of the logarithmic scale, according to the present model the dimensionless dissipation vanishes at the surface, in agreement with the findings of *Gemmrich* [2010]. The reason for the vanishing of the turbulent dissipation is that the turbulent velocity vanishes sufficient rapidly near the surface as illustrated in Figures 4 and 8. In contrast, the *Craig and Banner* [1994] approach gives a maximum in the dissipation at the surface.

5.   Numerical Simulation of the Diurnal Cycle in SST and Surface Current

[67]   In this section the mixed layer model described in section 3 is applied to a simulation of the diurnal cycle in sea surface temperature (SST) and the surface current. The relevant equations are (14), (10), (23), (24), (32) and (38). The boundary condition for the momentum equation is that the momentum flux at the surface is given by the turbulent stress $\vec{\tau}_a - \vec{\tau}_{in}$ (cf. equation (15)), while for the temperature equation the turbulent flux at the surface is given by $Q_h/(\rho_w c_p)$. The turbulent kinetic energy flux at the surface vanishes. At depth $z = -D$, where in the present application D is either 3.5 or 20 m, current velocity $\vec{u}(z)$ and temperature $T(z)$ are assumed to be given.

[68]   The equations for momentum, heat and turbulent kinetic energy are discretized in the vertical in such a way that the fluxes are conserved, while the relevant quantities are advanced in time using a fully-implicit scheme. The time step was chosen to be 300 seconds. This choice of time step still gave reasonably accurate results compared to a short time step run. With n labeling a particular layer and N the

total number of layers, the vertical discretization is obtained using a logarithmic transformation of the type

$$z(n) = -z_s\left(e^{\xi(n)} - 1\right), n \le N,$$

where $\xi(n) = n\Delta$ is discretized in a uniform manner and $\Delta = \log(D/z_s + 1)/N$. Typically, z_s is of the order of a few centimeters thus giving high resolution near the surface, which is needed to resolve the solar absorption profile (24) appropriately, while away from the surface resolution degrades. In general the parameter z_s is a constant with value 0.025 m. The depth D is a constant as well. Results will be reported for two applications, namely for $D = 3.5$ m and $D = 20$ m and the corresponding number of layers N is equal to 8 and 25.

[69]   Finally, when integrating the TKE equation forward in time numerical errors may introduce small negative turbulent kinetic energy so that determination of the turbulent velocity would fail because of taking the square root of the energy. For security reasons, therefore, a minimum value of turbulent kinetic energy is introduced being a small fraction of the equilibrium turbulent kinetic energy, $e_{min} = 0.0001 w_*^2/2$.

5.1.   Synthetic Example

[70]   As a first test a five day simulation was performed with constant fluxes of momentum τ and heat Q_h while the solar radiation followed a daily cycle according to $R = R_0 \max[\sin(\omega t), 0]$ where $\omega = 2\pi/(24 \times 3600)$. The intention is to generate a steady daily oscillation in SST without drift in the temperature and to study effects of ocean waves on shape and amplitude of the daily cycle. In order to achieve a steady oscillation in temperature, values of daily average insolation, heat and momentum flux have to be chosen appropriately. The momentum flux τ was chosen equal to 0.0069 m²/s², which, with a drag coefficient of 1.11×10^{-3}, corresponds to a wind speed of 2.5 m/s, while the heat flux was given the value - 200 W/m² typical for the Arabian sea in May. Hence, in the absence of radiative
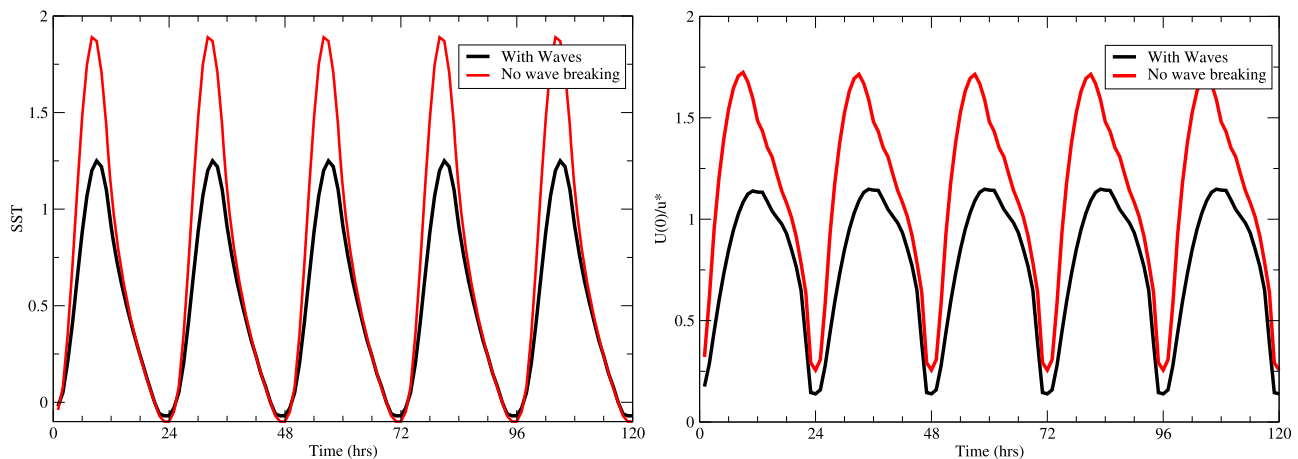
Figure 11. (left) For pure wind sea time series of SST for a constant wind speed of 2.5 m/s and a heat flux of -150 W/m^2; the daily average solar insolation is 350 W/m^2. The impact of disregarding ocean wave effects is shown as well. (right) The surface current normalized with the air friction velocity.

forcing the ocean would cool down. The constant R_0 in the formula for the solar insolation was given the value $350 \times \pi$ so that the daily average irradiation is 350 W/m^2 and the maximum irradiation is 1099 W/m^2. All other parameters such as the turbulent Langmuir number, the Stokes drift decay length scale and the water friction velocity were chosen as in section 4.1. Note that for these particular cases the decay length scale of the energy flux is assumed to be given by one-half the significant wave height where the sea state consists of wind sea and a swell of 0.5 m height, mimicking the typical sea state in the Arabian sea.

[71] In Figure 11 time series of SST are shown over the five day period and are compared with a simulation without wave effects. Note that in the simulations without wave effects the wave dissipation term and the Langmuir term are switched off in the TKE equation (32), while also the wave-induced stress in the momentum equation (11) is switched off. The boundary condition for momentum flux at the surface is then, of course, replaced by the usual one, namely $\tau = \rho_w w_*^2$. Surprisingly, even for a low wind speed case of 2.5 m/s, sea state effects on the simulation of the diurnal cycle in SST are clearly visible. As expected, wave dissipation and Langmuir turbulence give rise to an enhanced mixing and therefore a reduction in the diurnal cycle amplitude compared to the case without wave effects. From Figure 11 (right) a similar conclusion also follows for the

diurnal cycle in the surface current. The corresponding diurnal amplitude in the current is fairly substantial.

[72] In Figure 12 profiles for turbulent velocity $Q(z)$, temperature $T(z)$ and the magnitude of the current $|\vec{u}(z)|$ are shown. Four hours into the simulation the ocean is warming up producing a stable layer as is evident from the fact that the turbulent velocity is less than 1 in the deeper parts of the ocean. Temperature and velocity profile are not in equilibrium because they have an S-shape. Eight hours later, at sunset, the upper part of the ocean is already turning unstable because the ocean is cooling off as the heat flux, given by $Q_h = -200$ W/m^2 is directed from ocean to atmosphere. Therefore, in the upper part of the ocean the temperature profile is well-mixed and is slightly lower at the surface than at $|z|/H_S \approx 6$ where the maximum temperature is found. The shape of the surface current is now concave and it looks similar to the equilibrium profiles shown in Figure 9. Finally, at sunrise, 24 hours into the simulation the temperature in the whole column is almost uniform and equal to its value at the bottom of the domain. The reason is that during the night the whole ocean column becomes unstable giving an efficient transfer of heat towards the atmosphere and towards the deeper parts of the ocean. The efficient transfer is reflected by the observation that now the dimensionless turbulent velocity Q is everywhere larger than 1. Furthermore, the current is now the smallest because during the
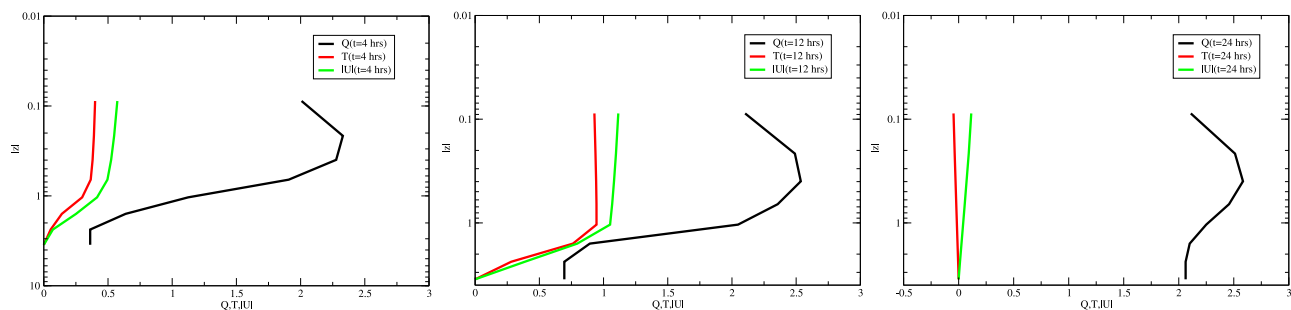

Figure 12. Profile of turbulent velocity, temperature and current after (left) 4, (middle) 12 and (right) 24 hours from the start of the simulation.
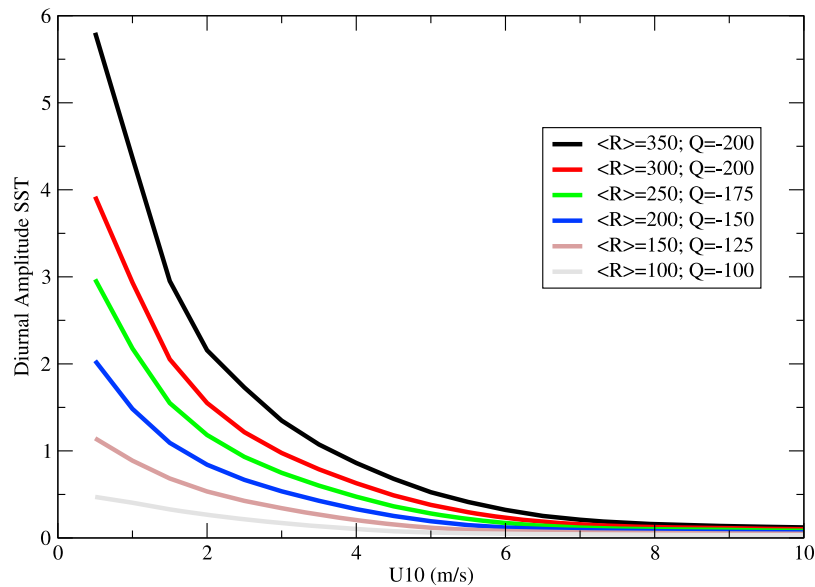
Figure 13. Diurnal amplitude in SST as function of wind speed for different solar insolation and heat flux as indicated in the legend. The sea state is a mixture of wind sea and swell of 0.5 m.

night also momentum has been transferred efficiently towards the deep ocean.

[73] In order to give an impression of the overall behavior of the present mixed layer model a one-day simulation was performed for different wind speed, solar insolation and heat flux. The results are summarized in Figure 13. The plot shows that the amplitude in the diurnal cycle is a sensitive function of wind speed and the magnitude of the solar insolation and heat flux. Note that larger diurnal cycle amplitudes may be achieved by reducing the magnitude of the heat flux, but in that event there are considerable drifts in the temperature record for one day.

5.2. Simulation of Buoy Observations

[74] Next, a simulation with the mixed layer scheme is performed and validated against buoy observations of the Arabian Sea Mixed Layer Dynamics Experiment (called Aranian Sea experiment for short) at 15°30′N, 61°30′E during a one year period from the 16th of October 1994 to the 20th of October 1995 [*Baumgartner et al.*, 1997; *Weller et al.*, 2002]. The Arabian Sea is an area with considerable variability in the weather where periods of strong winds (related to e.g. the Somali jet) are alternated by episodes of low winds. During these calm periods the diurnal cycle in SST can be quite profound. The mixed-layer model is driven by hourly surface fluxes computed with the COARE flux algorithm [*Fairall et al.*, 1996] using Improved Meteorology (IMET) buoy observations. Temperature observations and flux data were downloaded from the Woods Hole Oceanographic Institution web page. In particular the ocean temperature record is impressive as at a sampling rate of 15 min. temperature profiles have been observed at high vertical resolution starting at a depth of 0.17 m. This is therefore a unique opportunity to validate a mixed layer model.

[75] Results of two versions of the mixed layer model will be discussed. The first version has a depth of 3.5 m and as boundary condition the observed temperature at a depth of 3.5 m is prescribed, while the current at that depth is

assumed to vanish. This shallow version of the mixed layer model will be used to study modeled diurnal cycle and for verification purposes observed temperature at a depth of 0.17 m is compared with the model counterpart. As a boundary condition the observed temperature at a depth of 3.5 m is prescribed, while the current at that depth is assumed to vanish.

[76] However, in such a shallow model effects of Langmuir turbulence turn out to be relatively small as its maximum contribution is below the modeled domain and therefore also results of a second version of the mixed layer model will be presented that has a depth of 20 m. Again, as boundary condition the observed temperature at 20 m depth is prescribed while the current at that depth is assumed to vanish.

[77] In both versions sea state parameters such as significant wave height H_S, its wind sea part $H_{S,ws}$, the mean wave number k_S the components of the Stokes drift and the energy flux parameter α have been obtained using archived wave spectra from the ERA-Interim (wave) analysis [*Dee et al.*, 2011]. The 6-hourly wave parameters are interpolated in time and supplied to the mixed-layer scheme.

[78] A number of experiments were performed with the shallow version of mixed-layer scheme. The first set of experiments were done to decide what is, in the context of the present model, the most appropriate penetration depth and/or roughness length z_0 that represents the transfer of ocean wave motion to ocean turbulence. A number of choices were tried, namely

[79] 1. Relate z_0 to the wave height of the wind waves. This expresses the nonlinear character of the wave dissipation process.

[80] 2. Relate z_0 to the significant wave height including swell. This reflects that the dissipating ocean waves are transported in the vertical by the longer waves.

[81] The statistics from the comparison with the temperature observations are shown in Table 1 and it is clear that the second option performs best as the bias is very small while in particular the standard deviation of error in SST is only

Table 1. Summary of Statistics of a Number of Experiments[a]

Exp	Bias DSA	SD DSA	SST Bias	SD SST	VAR
$z_0 = 0.5\ H_{S,ws}$	+0.08	0.19	+0.02	0.11	1.23
$z_0 = 0.5\ H_S$	**−0.02**	**0.13**	**−0.00**	**0.07**	**0.97**
No Breaking	+0.09	0.16	+0.02	0.11	1.19
+No Langmuir	+0.11	0.16	+0.03	0.11	1.20
$C_M = 0$	+0.06	0.17	+0.03	0.12	1.17
$\langle \alpha \rangle = 130$	−0.07	0.17	−0.02	0.10	0.79

[a]Here, DSA is the Diurnal SST Amplitude, SD is the standard deviation and VAR is the variability normalized with the observed variability. The number of hourly SST observations is 8712, while the number of daily cycles is 363. The best statistics (i.e., the smallest errors) are given in bold.

0.07 K. Therefore, from now on the decay length scale will be given by $z_0 = 0.5\ H_S$ where H_S is the significant wave height which represents both wind sea and swell. For this case a 20 day section of the time series for $\Delta T = T(0.17) - T(3.5)$ is shown in Figure 14. For completeness, also time series of some relevant forcings are shown, namely the sum of solar radiation and heat flux, the wind speed and the dimensionless wave breaking flux α. From these additional graphs it can be seen that the cycle in the net surface flux is fairly constant, but that there are considerable variations in wind speed (ranging from 0.5 m/s to 9 m/s) and normalized energy flux, explaining the considerable variations in the diurnal cycle amplitude. Furthermore, in Figure 15

the modeled Diurnal SST Amplitude (DSA) is compared with the observed one. Note that here DSA is defined as the difference between daily maximum and daily minimum in SST. The mixed-layer model seems to perform remarkably well.

[82] Some additional experiments were performed. In section 4.1 it was argued that the diffusion term in the TKE equation may probably be neglected. In order to verify this the mixed-layer model was run without diffusion in the TKE equation and the verification statistics were found to be almost identical to the case with diffusion (not shown) therefore confirming that neglect of diffusion in the TKE equation is a valid assumption. Furthermore, it is of interest to study the importance of wave breaking and Langmuir turbulence in the simulation of SST. When wave breaking is switched off it is seen from Table 1 that the verification statistics worsen considerable, in particular for the standard deviation of error in DSA and SST (the latter shows an increase of more than 50%). Hence, effects of wave breaking are important for the diurnal cycle in SST. On the other hand, when in addition to wave breaking the effects of Langmuir turbulence are switched off it is seen that Langmuir turbulence has a relatively small impact on the simulation of the diurnal cycle for the present case. This follows from a comparison of the no Breaking row with the +No Langmuir in row of Table 1. This can be understood as follows. While the
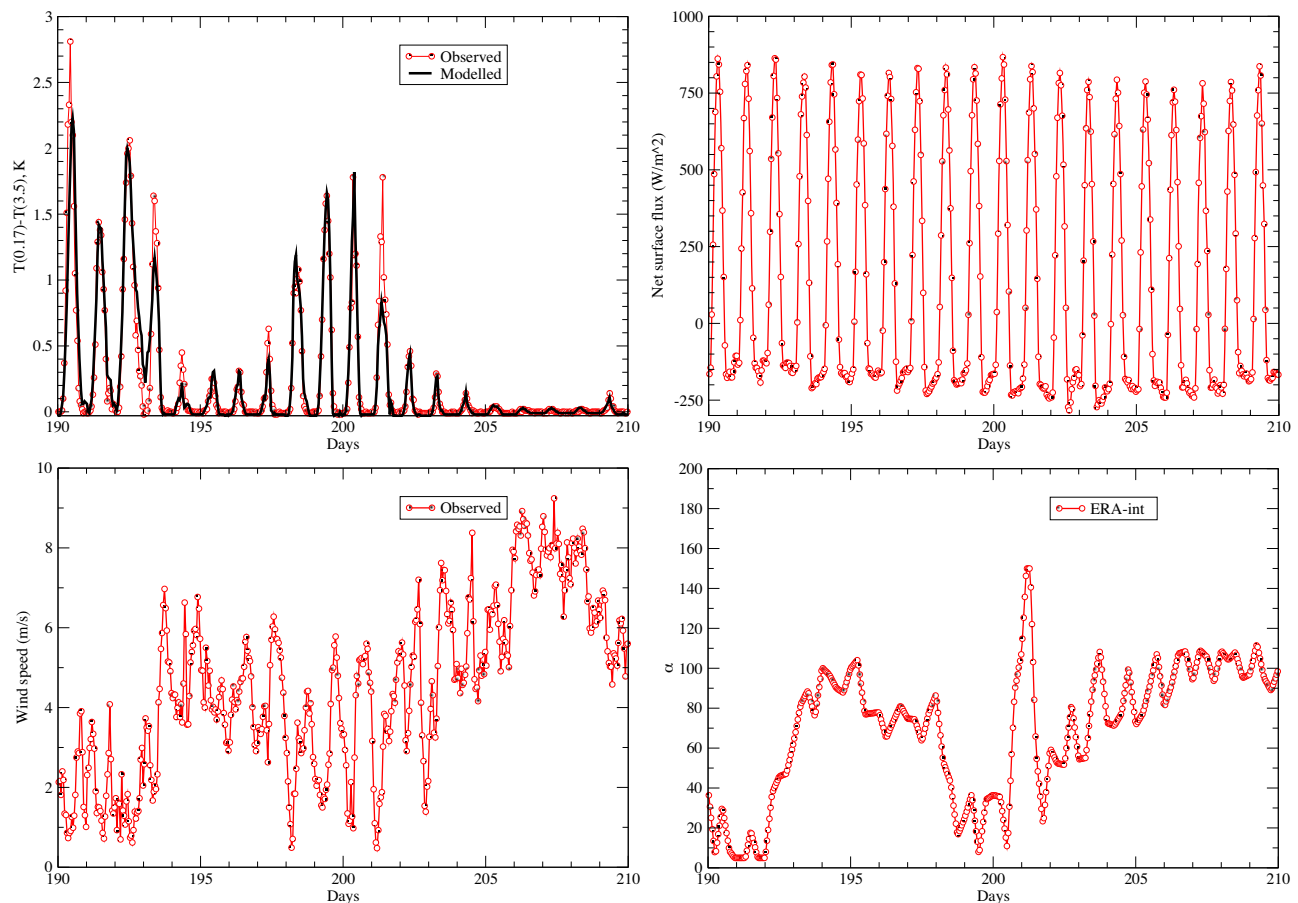

Figure 14. (top left) Observed and simulated ocean temperature $\Delta T = T(0.17) - T(3.5)$ at 15°30′N, 61°30′E in the Arabian Sea for 20 days from the 23rd of April. Relevant forcings are shown for (top right) net surface flux, (bottom left) wind speed and (bottom right) dimensionless wave breaking flux α.
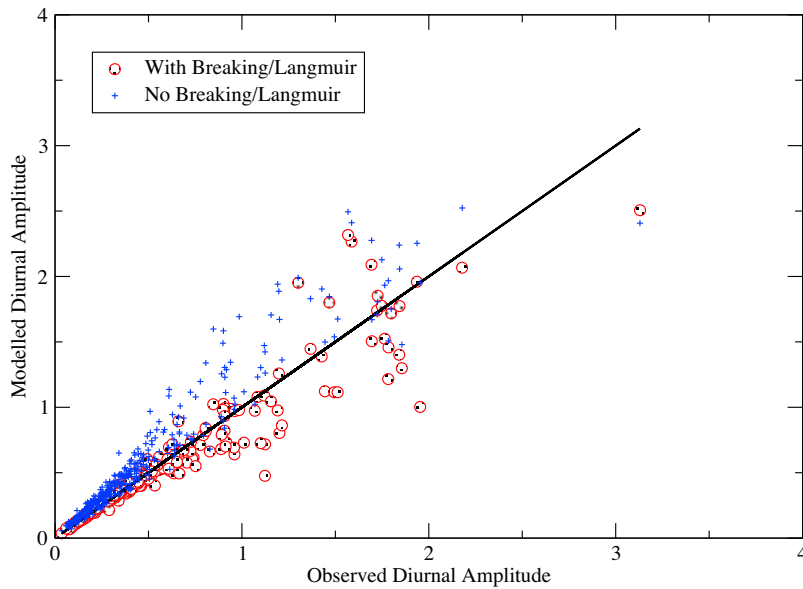
Figure 15. Comparison of simulated and observed diurnal amplitude at 15°30′N, 61°30′E in the Arabian Sea for the one-year period starting from 16th of October 1994. The case of no wave breaking effects in the TKE equation is shown as well.

average Langmuir number is about 0.4, suggesting that Langmuir turbulence should be relevant, it is noted that for this particular example the average wave number over the one year period is found to be $\langle k_S \rangle \approx 0.072$ so that the maximum contribution by Langmuir turbulence (cf. section 4) is at $z = -1/(2k_S) \approx -7.0$ m which is outside the domain that was modeled (recall that the boundary condition for temperature was provided at a depth of 3.5 m). A factor that has more impact on the simulation results is how stratification effects are modeled. In order to illustrate the sensitivity to the shape of the stratification function f_M an experiment was performed where c_M in equation (38) was set to zero. In that event there is a critical Richardson number and, just like heat, momentum transport vanishes for large gradient Richardson number. As can be seen from Table 1 this change has a significant impact on the verification statistics, with a large increase in bias, standard deviation of error and normalized variability.

[83] To conclude the discussion of the results from the shallow version of the mixed layer model we emphasize that wave effects are important in the simulation of the diurnal cycle. This follows already from the verification results in the Table 1 for the case that wave effects (wave breaking and Langmuir turbulence) are switched off. In addition, for the case of no wave effects results for the diurnal SST amplitude are shown in Figure 15. Comparing with the results of the full model it confirms that without wave effects SST is overestimated, while the standard deviation of error increases by 25%. Additional evidence of the sensitivity of the diurnal cycle to the sea state may be found in the last experiment. The average value of energy flux parameter α over the one year period is about 93. Let us consider now a simulation with the global average of α, equal to 130, then it is seen that a considerable bias in simulated DSA is found

while the normalized variability reduces by 20%. Hence, for an accurate simulation of the diurnal cycle an accurate representation of wave dissipation in space (and probably also in time) seems to be important.

[84] Finally, in order to see to what extent Langmuir turbulence and also the Stokes-Coriolis force are relevant in the deeper parts of the ocean, a simulation was performed with the 20 m depth version of the mixed layer model. With the bottom at 20 m depth it is expected to capture effects of Langmuir turbulence better since its maximum effect is on average at 7 m depth. Here, as boundary conditions the observed temperature was used, while the current vanishes at the bottom. Model results for the temperature profile were compared with the observations from the Arabian Sea Experiment and statistics for bias and standard deviation of error are shown in Figure 16. The figure shows the stats as function of depth for three experiments. The experiment labeled 'CTRL' has all relevant effects switched on and has the smallest errors, in the experiment labeled 'No Breaking' effects of wave breaking are switched off while in the experiment 'No Stokes' both the Stokes drift and wave breaking are switched off. It is clear from the stats displayed in Figure 16 that the biggest positive impact of the effect of wave breaking is near the surface. Noting that the average significant wave height over the one year period is 1.8 m it is seen that, as expected, wave breaking affects the temperature results in a layer with a thickness of the significant wave height. With a deeper ocean it is now evident that also the combined effects of Langmuir turbulence and Stokes-Coriolis force determine to some extent the temperature profile, having the biggest positive impact in the deeper layers of the ocean. However, as discussed in section 4.1, during the day time the impact of Langmuir turbulence is considerably reduced because of the stable stratification.
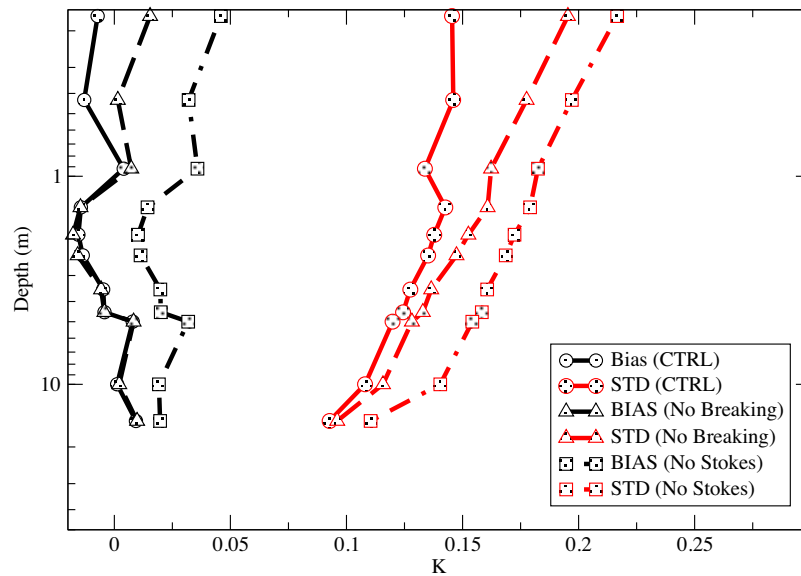
Figure 16. Validation of simulated temperature profiles against observed ones at 15°30′ N, 61°30′ E in the Arabian Sea for the one-year period starting from the 16th of October 1994. Shown are results for bias and the standard deviation of error as function of depth. The depth of the model is 20 m. When wave breaking and Stokes drift effects are switched off a considerable increase of errors is found.

Therefore, the main reason for the improvement in the deeper layers of the ocean is the Stokes-Coriolis force.

6. Conclusions

[85] The main purpose of this paper was to investigate the role of wave dissipation (e.g. wave breaking), Langmuir turbulence and Stokes-Coriolis forcing on the mixing of the upper ocean. As an interesting first application the impact of ocean waves dynamics on the simulation of the diurnal cycle in SST was studied. The wave effects were studied in the context of the Mellor-Yamada (1982) scheme where the TKE equation was extended to allow for effects of wave dissipation and following *Grant and Belcher* [2009] effects of Langmuir turbulence. Following *Janssen et al.* [2004] effects of wave dissipation on turbulence production in the ocean column were incorporated by modeling the wave-induced energy flux $-\overline{\delta p \delta w}$ while wave dissipation also affects the ocean momentum through the wave-induced stress. Particular attention was paid to modeling of stratification effects on the turbulent exchange coefficients for momentum, heat and turbulent kinetic energy, since, apart from solar insolation, the main reason for the existence of the diurnal cycle is the reduction of the turbulent transport by buoyancy effects. For low winds and strong solar forcing stratification in the ocean can become quite extreme, but unfortunately observations under these extreme circumstances are rare. Therefore, at least in the atmospheric context, there is no consensus on how the turbulent exchange coefficients behave in strongly stable conditions. First, it may be argued that turbulent motion is damped when the gradient Richardson number exceeds a critical value, say of the order of 1/4. A prominent example of this approach is the Mellor-Yamada scheme. Many others argue, on the other hand, that beyond the critical Richardson number there is still transport possible related to internal gravity waves and

intermittency. Presently, two directions may then be distinguished. One approach, which is based on observations, direct numerical simulations and group normalization methods argues that due to internal wave activity and intermittency momentum transfer will be more efficient than heat transport, while, on the other hand, from the SHEBA data there is compelling evidence that the opposite is true. A choice has therefore to be made, and in the main text arguments have been presented why I have chosen the option of a more efficient momentum transport for the strongly stable case. At the same time, for the weakly stable case the proposed model for stratification agrees with the Kansas field experiment.

[86] Properties of the resulting model for mixing in the upper ocean have been studied extensively. Under neutral circumstances it can be shown that the turbulent velocity may be obtained from a '1/3'-rule (see equation (45)). This rule is important in understanding the sensitivity of upper ocean transport to variability in the sea state. When determining the energy flux from dissipating waves it is found that there is high variability in the dimensionless flux α in particular near the passage of a front (see Figure 1). As the turbulent velocity depends, according to the '1/3'-rule only on $\alpha^{1/3}$, its variability, and the variability in the turbulent transport, is much reduced. The '1/3'-rule also explains that when only Langmuir turbulence is taken into account the turbulent velocity scales with $La^{-2/3}$ in agreement with the scaling arguments of *Grant and Belcher* [2009].

[87] Results from a simulation with the present mixed layer model (with a bottom at 3.5 m depth) of the diurnal cycle in SST over a one year period for a location in the Arabian Sea are compared with in-situ observations and judged by statistical parameters such as bias, standard deviation and simulated variability there is good agreement. It has also been shown that, as expected, results depend in a sensitive manner on the way stratification is modeled. For

JANSSEN: DAILY CYCLE IN SST

example, neglect of the contribution to turbulent transport by intermittency and internal gravity waves gives a large increase in error. In a similar spirit, it can be shown that wave effects play an important role in the mixing in the upper ocean. No sensitivity to Langmuir turbulence was found in the simulation results for the diurnal cycle, presumably because on average the maximum of the Langmuir production term was at a larger depth than the depth where the boundary condition for ocean temperature was given. For this reason, also simulations with the mixed layer model with the bottom at 20 m are presented as it was expected that with a deeper version of the model effects of Langmuir turbulence are better captured. However, in agreement with the analysis in section 4.1 the effect of Langmuir turbulence is considerable reduced in stable circumstances. Therefore, the main improvement in the deeper layers of the ocean is caused by the Stokes-Coriolis force.

[88] Nevertheless, the model still needs to be validated more extensively against satellite observations from geostationary satellites and polar orbiters. Furthermore, work is needed to better understand the effects of waves on the transport of heat, in particular regarding the heat flux profile in case of wave breaking. This work is left for the future.

References

Anis, A., and J. N. Moun (1995), Surface wave-turbulence interactions: Scaling $\epsilon(z)$ near the sea surface, *J. Phys. Oceanogr.*, 25, 2025–2045.

Baas, P., S. R. de Roode, and G. Lenderink (2008), The scaling behaviour of a turbulent kinetic energy closure model for stably stratified conditions, *Boundary Layer Meteorol.*, 127, 17–36.

Banner, M. L. (1990), Equilibrium spectra of wind waves, *J. Phys. Oceanogr.*, 20, 966–984.

Baumgartner, M. F., N. J. Brink, W. M. Ostrom, R. P. Trask, and R. A. Weller (1997), Arabian Sea mixed layer dynamics experiment data report, *Tech. Rep. WHOI-97-08*, 157 pp., Woods Hole Oceanogr. Inst., Woods Hole, Mass.

Birch, K. G., and J. A. Ewing (1986), Observations of wind waves on a reservoir, *Rep. 234*, 37 pp., Inst. of Oceanogr. Sci., Wormley, U. K.

Britter, R. E., J. C. R. Hunt, G. L. Marsh, and W. H. Snyder (1983), The effects of stable stratification on turbulent diffusion and the decay of grid turbulence, *J. Fluid Mech.*, 127, 27–44.

Burchard, H. (2001), Simulating the wave-enhanced layer under breaking surface waves with two-equation turbulence models, *J. Phys. Oceanogr.*, 31, 3133–3145.

Businger, J. A., J. C. Wyngaard, Y. Izumi, and E. F. Bradley (1971), Flux-profile relationships in the atmospheric surface layer, *J. Atmos. Sci.*, 28, 181–189.

Cheng, Y., and W. Brutsaert (2005), Flux-profile relationships for wind speed and temperature in the stable atmospheric boundary layer, *Boundary Layer Meteorol.*, 114, 519–538.

Craig, P. D. (1996), Velocity profiles and surface roughness under breaking waves, *J. Geophys. Res.*, 101, 1265–1277.

Craig, P. D., and M. L. Banner (1994), Modeling wave-enhanced turbulence in the ocean surface layer, *J. Phys. Oceanogr.*, 24, 2546–2559.

Csanady, G. T. (1964), Turbulent diffusion in a stratified fluid, *J. Atmos. Sci.*, 21, 439–447.

Deardorff, J. W. (1980), Stratocumulus-capped mixed layers derived from a three-dimensional model, *Boundary Layer Meteorol.*, 18, 495–527.

Dee, D. P., et al. (2011), The ERA-Interim reanalysis: Configuration and performance of the data assimilation system, *Q. J. R. Meteorol. Soc.*, 137, 553–597.

Drennan, W. M., M. A. Donelan, E. A. Terray, and K. B. Katsaros (1996), Ocean turbulence dissipation rate measurements in SWADE, *J. Phys. Oceanogr.*, 26, 808–815.

Fairall, C. W., E. F. Bradley, D. P. Rogers, J. B. Edson, and G. S. Young (1996), Bulk parametrization of air-sea fluxes for Tropical Ocean–Global Atmosphere Coupled–Ocean Atmosphere Response Experiment, *J. Geophys. Res.*, 101, 3747–3764.

Gemmrich, J. (2010), Strong turbulence in the wave crest region, *J. Phys. Oceanogr.*, 40, 583–595.

Grachev, A. A., E. L. Andreas, C. W. Fairall, P. S. Guest, and P. O. G. Persson (2007a), SHEBA flux-profile relationships in the stable atmospheric boundary layer, *Boundary Layer Meteorol.*, 124, 315–333.

Grachev, A. A., E. L. Andreas, C. W. Fairall, P. S. Guest, and P. O. G. Persson (2007b), On the turbulent Prandtl number in the stable atmospheric boundary layer, *Boundary Layer Meteorol.*, 125, 329–341.

Grant, A. L. M., and S. E. Belcher (2009), Characteristics of Langmuir turbulence in the ocean mixed layer, *J. Phys. Oceanogr.*, 39, 1871–1887.

Hara, T., and A. V. Karachintsev (2003), Observation of nonlinear effects in ocean surface wave frequency spectra, *J. Phys. Oceanogr.*, 33, 422–430.

Hasselmann, K. (1970), Wave-driven inertial oscillations, *Geophys. Fluid Dyn.*, 1, 463–502.

Hasselmann, K., et al. (1973), Measurements of wind-wave growth and swell decay during the Joint North Sea Wave Project (JONSWAP), *Dtsch. Hydrogr. Z. Suppl. A*, 8(12), 1–95.

Janssen, P. A. E. M. (1982), Quasilinear-approximation for the spectrum of wind-generated water waves, *J. Fluid Mech.*, 117, 493–506.

Janssen, P. A. E. M. (1991), Quasi-linear theory of wind wave generation applied to wave forecasting, *J. Phys. Oceanogr.*, 21, 1631–1642.

Janssen, P. A. E. M. (1997), Effect of surface gravity waves on the heat flux, *Res. Dep. Tech. Memo. 239*, 14pp., Eur. Cent. for Medium-Range Weather Forecasts, Reading, U. K. [Available at http://www.ecmwf.int/publications/.]

Janssen, P. A. E. M. (1999), On the effect of ocean waves on the kinetic energy balance and consequences for the inertial dissipation technique, *J. Phys. Oceanogr.*, 29, 530–534.

Janssen, P. A. E. M. (2010), Ocean wave effects on the daily cycle in SST, *Res. Dep. Tech. Memo. 634*, 38pp., Eur. Cent. for Medium-Range Weather Forecasts, Reading, U. K. [Available at http://www.ecmwf.int/publications/.]

Janssen, P. A. E. M., and J.-R. Bidlot (2009), On the extension of the freak wave warning system and its verification, *Res. Dep. Tech. Memo. 588*, 38 pp., Eur. Cent. for Medium-Range Weather Forecasts, Reading, U. K. [Available at http://www.ecmwf.int/publications/.]

Janssen, P. A. E. M., O. Saetra, C. Wettre, H. Hersbach, and J. Bidlot (2004), Impact of the sea state on the atmosphere and ocean, *Ann. Hydrogr.*, 3(772), 3.1–3.23.

Jenkins, A. D. (1987), A Lagrangian model for wind- and wave-induced near-surface currents, *Coastal Eng.*, 11, 513–526.

Kim, J., and L. Mahrt (1992), Simple formulation of turbulent mixing in the stable free atmosphere and nocturnal boundary layer, *Tellus, Ser. A*, 44, 381–394.

Komen, G. J. (1987), Energy and momentum fluxes through the sea surface, in *Dynamics of the Ocean Surface Mixed Layer*, edited by P. Müller and D. Henderson, pp. 207–217, Hawaii Inst. of Geophys., Honolulu.

Kondo J., O. Kanechika, and N. Yasuda (1978), Heat and momentum transfers under strong stability in the atmospheric surface layer, *J. Atmos. Sci.*, 35, 1012–1021.

Kondo, J., Y. Sasano, and T. Ishii (1979), On wind-driven current and temperature profiles with diurnal period in the oceanic planetary boundary layer, *J. Phys. Oceanogr.*, 9, 360–372.

Large, W. G., J. C. McWilliams, and S. C. Doney (1994), Oceanic vertical mixing: A review and a model with a nonlocal boundary parameterization, *Rev. Geophys.*, 32, 363–403.

Longuet-Higgins, M. S. (1983), On the joint distribution of wave periods and amplitudes in a random wave field, *Proc. R. Soc. London A*, 389, 241–258.

McWilliams, J. C., and J. M. Restrepo (1999), The wave-driven ocean circulation, *J. Phys. Oceanogr.*, 29, 2523–2540.

Mellor, G. L., and T. Yamada (1982), Development of a turbulence closure model for geophysical fluid problems, *Rev. Geophys.*, 20, 851–875.

Monti, P., H. J. S. Fernando, M. Princevac, W. C. Chan, T. A. Kowalewski, and E. R. Pardyjak (2002), Observations of flow and turbulence in the nocturnal boundary layer over a slope, *J. Atmos. Sci.*, 59, 2513–2534.

Nieuwstadt, F. T. M. (1984), The turbulent structure of the stable, nocturnal boundary layer, *J. Atmos. Sci.*, 41, 2202–2216.

Noh, Y., and H. J. Kim (1999), Simulations of temperature and turbulence structure of the oceanic boundary layer with the improved near-surface process, *J. Geophys. Res.*, 104, 15,621–15,633.

Pacanowski, R. C., and S. G. H. Philander (1981), Parameterization of vertical mixing in numerical models of tropical oceans, *J. Phys. Oceanogr.*, 11, 1443–1451.

Panofsky, H. A. (1963), Determination of stress from wind and temperature measurements, *Q. J. R. Meteorol. Soc.*, *89*, 85–94.

Phillips, O. M. (1977), *The Dynamics of the Upper Ocean*, 336 pp., Cambridge Univ. Press, Cambridge, U. K.

Plant, W. J. (1982), A relation between wind stress and wave slope, *J. Geophys. Res.*, *87*, 1961–1967.

Soloviev, A. V. (1982), On the vertical structure of the ocean thin surface layer at light wind, *Dokl. Acad. Sci. USSR Earth Sci. Ser.*Engl. Transl., *18*, 751–760.

Strang, E. J., and H. J. S. Fernando (2001), Vertical mixing and transports through a stratified shear layer, *J. Phys. Oceanogr.*, *31*, 2026–2048.

Sukoriansky, S., B. Galperin, and I. Staroselsky (2005), A quasinormal scale elimination model of turbulent flows with stable stratification, *Phys. Fluids*, *17*, 085107.

Terray, E. A., M. A. Donelan, Y. C. Agrawal, W. M. Drennan, K. K. Kahma, A. J. Williams, P. A. Hwang, and S. A. Kitaigorodskii (1996), Estimates of kinetic energy dissipation under breaking waves, *J. Phys. Oceanogr.*, *26*, 792–807.

Terray, E. A., W. M. Drennan, and M. A. Donelan (1999), The vertical structure of shear and dissipation in the ocean surface layer, in *The*

Wind-Driven Air-Sea Interface*, edited by M. L. Banner, pp. 239–245, Sch. of Math., Univ. of N. S. W., Sydney, Australia.

Weber, J. E. (1983), Steady wind- and wave-induced currents in the open ocean, *J. Phys. Oceanogr.*, *13*, 524–530.

Weber, S. L. (1994), Statistics of the air-sea fluxes of momentum and mechanical energy in a coupled wave-atmosphere model, *J. Phys. Oceanogr.*, *24*, 1388–1398.

Weller, R. A., A. S. Fisher, D. L. Rudnick, C. C. Eriksen, T. D. Dickey, J. Marra, C. Fox, and R. Leben (2002), Moored observations of upper-ocean response to the monsoons in the Arabian Sea during 1994–1995, *Deep Sea Res., Part II*, *49*, 2195–2230.

Wyngaard, J. C. (1985), Structure of the planetary boundary layer and implications for its modeling, *J. Clim. Appl. Meteorol.*, *24*, 1131–1142.

Xu, Z., and A. J. Bowen (1994), Wave- and wind-driven flow in water of finite depth, *J. Phys. Oceanogr.*, *24*, 1850–1866.

Zilitinkevich, S. S., T. Elperin, N. Kleeorin, and I. Rogachevskii (2007), Energy- and flux-budget (EFB) turbulence closure model for stably stratified flows. Part I: Steady-state, homogeneous regimes, *Boundary Layer Meteorol.*, *125*, 167–191.